Formation of Giant Single Crystals of Isotactic Polypropylene via Mesophase(Dissertation_全文)

AUTHOR(S):

Asakawa, Harutoshi

Formation of Giant Single Crystals of Isotactic Polypropylene via Mesophase

Harutoshi ASAKAWA

2012

Contents

Chapter 1

General Introduction

Polymer material is widely used in human life because of its lightness and hardness. Crystal structure influences especially hardness of products, and understandings of the crystal structure and the crystallization mechanism are very important for controlling the property. Therefore, a huge amount of research for polymer crystallization has been carried out from industrial and scientific standpoints. A typical morphology in polymer crystals obtained from melts is well known as spherulites which are composed of ribbon-like chain-folded lamellar crystals radiating from their center [1]. The crystallization kinetics has been examined mainly by a theory of Lauritzen and Hoffman [2]. However, the initial crystallization processes prior to crystal nucleation are not well understood even in the case of homogeneous crystal nucleation. It has so far been considered that the primary crystal nucleation occurs directly from the melt; the crystal nuclei are suddenly caused by the occurrence of embryos with sufficient size in a supercooled liquid through spontaneous fluctuations.

Recently, some groups [3-15] reported that there are considerable experimental evidences for density fluctuations at very early times of crystallization before the full crystallographic features can be detected. These researches have led to an intriguing suggestion that spinodal decomposition (SD) occurs in the early stage of polymer crystallization and Olmsted [16] has tried to explain the phenomenon in terms of a liquid-liquid co-existence in a one-component thermodynamic system. Furthermore, other groups [17, 18] proposed that the formation and growth of lamellar crystallites is a multi-step process passing over intermediate states from the results of temperature dependence of the lamellar thickness.

In this chapter, we will review the classical crystallization theories, and current crystallization concept. We focus on the studies on the structure formation of crystal

nucleation via an intermediate state. The purpose of this chapter is to give a basis to understand the results presented in this thesis.

1.1. Classical Polymer Crystallization Concepts

1.1.1. Primary Crystal Nucleation

Precursors of crystal nuclei appear or disappear in the amorphous phase during induction period of crystal nucleation [19]. If the precursors are larger than some critical size, the crystal nuclei will grow and eventually crystallize. The free energy of crystallization Δf is derived from increase of surface free energy calculated from the surface area A of crystalline nuclei and decrease of the free energy Δf_c derived from the volume V of crystal as follows [19],

$$\Delta f = A\sigma - V\Delta f_c \tag{1.1.1}$$

where σ is the specific surface free energy. The Δf_c is written as,

$$\Delta f_c = \Delta H_m - T\Delta S_m. \tag{1.1.2}$$

when crystallization temperature T is equilibrium temperature T_m^∞, the value of Δf become zero. So, Δf can be written as follows,

$$\Delta f_c = \Delta H_m (T_m^\infty - T)/T_m^\infty = \Delta H_m \Delta T/T_m^\infty \tag{1.1.3}$$

where ΔH_m is the heat of fusion and ΔT is the degree of undercooling from the melting temperature. Assuming that width and length of crystalline nuclei of a crystalline nuclei are a and l, respectively, the free energy of the crystalline nucleation is written as

$$\Delta f = 2a^2\sigma_e + 4al\sigma_s - a^2l\Delta f_c \tag{1.1.4}$$

where σ_e is surface free energy on chain folding plane and σ_s is surface free energy on the plane taken alone a chain stretching axis (see Figure 1.1). The critical nuclei sizes a^*, l^* and the critical free energy Δf^* is calculated from Eq. (1.1.4) as follows

$$a^* = 4\sigma_s/\Delta f_c$$

$$l^* = 4\sigma_e/\Delta f_c$$

$$\Delta f^* = 32\sigma_e\sigma_s^2/\Delta f_c^2. \tag{1.1.5}$$

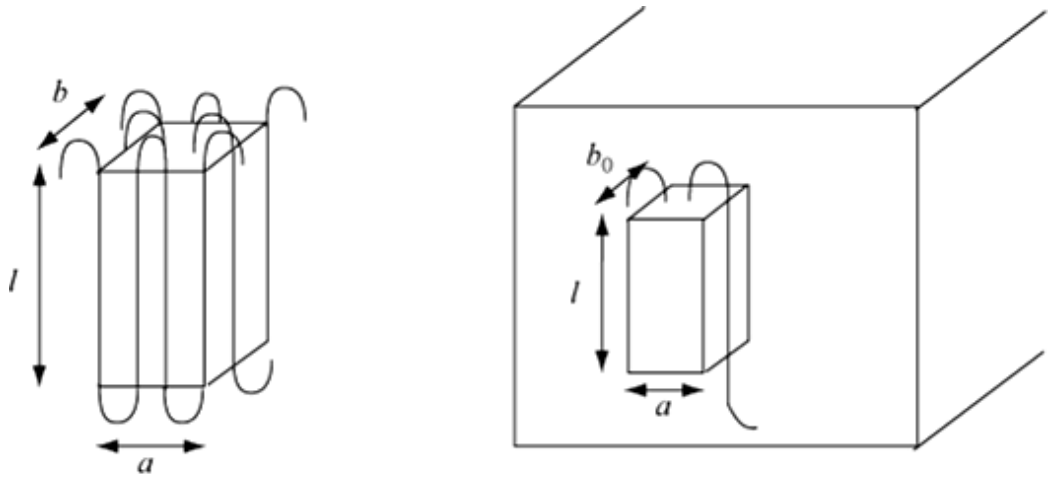

Figure 1.1. Crystalline nucleation models of polymer; *a* and *b*, widths of crystalline nuclei; *l*, a length of crystalline nuclei unit; b_0, a thickness of a polymer chain.

1.1.2. Secondly Crystal Nucleation

Crystal growth in polymer system, which can be observed by optical microscope, was explained on the basis of the primary crystal nucleation mechanism and the secondly crystal nucleation mechanism by Lauritzen and Hoffman [2]. Figure 1.1 shows the secondly crystal nucleation mechanism. A part of polymer chains first attaches onto the growth surface of the crystal, and this attached polymer chain crystallizes on the surface. The free energy change of the secondly crystal nucleation is given by [19],

$$\Delta f = 2ab_0\sigma_e + 2b_0l\sigma_s - ab_0l\Delta f_c \tag{1.1.6}$$

where b_0 is a diameter of a polymer chain. The critical nuclei sizes a^*, l^* and the critical free energy Δf^* is calculated from Eq. (1.1.6) as follows

$$a^* = 2\sigma_s/\Delta f_c$$

$$l^* = 2\sigma_e/\Delta f_c$$

$$\Delta f^* = 4\, b_0\sigma_e\sigma_s/\Delta f_c. \tag{1.1.7}$$

The secondly crystal nucleation process tends to take place rather than the primary crystal nucleation from the viewpoint of the required free energy for crystal nucleation.

1.1.3. Crystallization Temperature Dependence of Crystal Thickness

When crystalline polymer is isothermally crystallized at a certain temperature, crystal thickness becomes a certain value. The thickness depends on crystallization temperature, and increases with temperature. The temperature dependence of the crystal thickness l can be experientially written as [19]

$$l = C_1/\Delta T + C_2 \tag{1.1.8}$$

where C_1 and C_2 are constants. When crystal structure grows as lamellar structure beyond the critical nuclei (a^*, l^*), the average of the lamellar thickness $< l >$ is given by

$$< l > = l^* + \Delta l$$

$$l^* = 2\sigma_e/\Delta f_c$$

$$\Delta l = (kT/2b_0\sigma_s)\,(4\sigma_s/a - \Delta f_c)\,(2\sigma_s/a - \Delta f_c) \tag{1.1.9}$$

where k_B is Boltzmann constant. So, when ΔT is relatively smaller, $\Delta l = (k_B T/b_0\sigma_s)$ is obtained, and the dependence of the crystal thickness is given by

$$< l > = 2\sigma_e T_m^{\infty}/\Delta H_m \Delta T + kT/b_0\sigma_s \quad (1.1.10)$$

This equation corresponds to Eq. (1.1.8). When ΔT is $2\sigma_s/a\Delta H_m$, Δl is infinite value. This phenomenon is called as "Δl catastrophe". In order to avoid this problem, the variety models of attaching polymer chain based on the one-dimension nucleation concept or two-dimension nucleation concept were reported [20-22]

1.2. Current Polymer Crystallization Concepts

As mentioned above, the polymer crystallization kinetics have been discussed in terms of the nucleation and growth (NG) theory for a long time. However, the extensive studies in the last decades explored that there are another crystallization mechanism. That is crystallization via non-equilibrium intermediate state. The concept has brought about by a pioneering finding of crystallization mechanism assisted by spinodal decomposition and the subsequent experiments, theories and simulation works. In the following we will introduce some of the important works on the polymer crystallization via intermediate states.

1.2.1 Polymer Crystallization Assisted by Spinodal Decomposition

Kaji's Concept

Kaji and coworkers looked at the fundamentally important question; what happens during the induction period of polymer crystallization [3, 4]. They presumed that the nodules observed by Miyaji and Geil [23] were precursors of subsequent crystal nucleation because PET was essentially a crystalline polymer and an ultra-fast quenched PET film did not show the nodules [23]. Based on this idea, Imai *et al*. [3, 4] carried out SAXS studies on the structural changes in the induction period of crystallization of PET, leading to a surprising finding that SD really occurs during the induction period before primary crystal nucleation.

Here it is noted that the initial characteristic wavelength was about 15 nm, which agrees well with the above-mentioned inter-nodular spacing. It was also confirmed by de-polarized light scattering (DPLS) that the cause for this was due to the orientation fluctuations of polymer rigid segments [11]; the orientation domains may be considered to have liquid crystal-like structure, so-called nematic. It was then evidenced from Fourier-transform infrared spectroscopic observations for isotactic polystyrene (iPS) [5] that in the amorphous state prior to crystallization polymer chain molecules partly changed the random conformation to the crystalline one, which is 3/1 helix for iPS. The parts of such helical conformation correspond to the stiff segments, and their extension with time leads to the increase of excluded volume to cause the driving force for the orientational fluctuations, which can be explained by the Doi's theory [24-27].

Figure 1.2 shows a schematic diagram to explain the Doi's theory [24-27]. When the helical sequence increases in length, the excluded volume V_{excl} of the helical sequence rapidly increases with the length L (or persistence length l_{p}) according to the following equation:

$$V_{\mathrm{excl}} = 2bL^2 \mid \sin \Theta \mid \tag{1.2.1}$$

where b is a diameter of the stiff segment and Θ is the angle between the neighboring stiff segments. When the length of crystalline sequences exceeds a critical value, they start to orient parallel with one another to reduce the excluded volume or the free energy of the system. The critical concentration of the stiff segments when the orientation begins is given as [24]

$$\nu^* = 4.19/bL^2 \tag{1.2.2}$$

The complete parallel orientation makes the excluded volume zero while the complete perpendicular orientation gives the maximum value. The Doi's theory predicts that such parallel orientation does not occur homogeneously in the system, but it involves an SD type microphase separation into the oriented and unoriented domains. Kaji and coworkers applied the Doi's theory to describe the preparatory mechanism of polymer crystallization [3, 5, 12, 13]. They assumed regular helical structure in real polymer chains as a rod-like segment of

1. The conformational change
(ex. gauche- trans transition)

2. The persistence length is longer (because the internal enthalpy is decreased when polymers quenched).

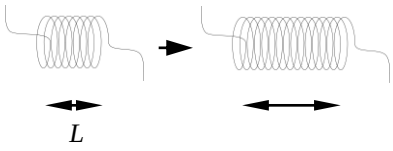

(helical or zigzag conformation)

3. The excluded volume effect of rod molecules (Doi's theory).

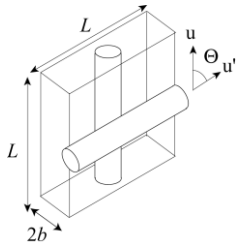

The excluded volume

$$V_{excl} = 2bL^2|\sin\Theta|$$

b: the diagram of rod segments

4. Isotropic-nematic transition.

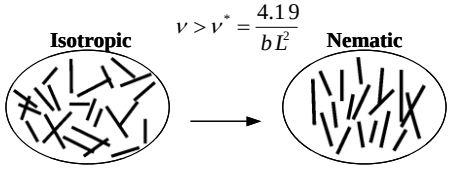

ν^*: the critical concentration
(spinodal decomposition)

Figure 1.2. Schematic diagram for the explanation of spinodal decomposition due to the orientation fluctuation of stiff segments occurring in the induction period prior to crystallization on the basis of Doi's kinetic theory [24-27]; V_{excl}, excluded volume; *b*, nearly equal to the diameter of the rod or stiff segment; *L*, rod length; Θ, angle between neighboring rods; ν^*, critical stiff segment concentration.

liquid crystalline polymer, and calculated concentration v of regular helical segments as follows:

$$v = \frac{\rho N_A}{(L / l_0) M_0} \tag{1.2.3}$$

where ρ, N_A, L, l_0 and M_0 are the density of the polymer, Avogadro's number, the average length of helical segments, the projected length of a monomer to the axis of helix, and molecular weight of the monomer, respectively. From Eqs. (1.2.2) and (1.2.3), the critical length L_c of helical segments for the Isotropic-nematic phase transition is given by [25]:

$$L_c = \frac{4.19 M_0}{b l_0 \rho N_A} \quad . \tag{1.2.4}$$

These theoretical predictions well explain the relation between SD and helical conformations of polymer chains obtained by Kaji and coworkers.

Furthermore, the annealing temperature dependence of the integrated intensity of DPLS was investigated for several polymers [15]; the detailed analysis of the results showed that the induction period can be separated into three regimes: the conformational change to the stiff segments, the initiation of orientation of the stiff-segments (the early stage of SD), and the growth of the oriented domains (or clusters) with self-similarity (the late stage of SD).

1.2.2. Polymer Crystallization via Mesomorphic Phase

Strobl's Concept

In recent years several research groups have tried to make clear morphologically and/or kinetically the mechanisms for structural formation processes in the early stages of polymer crystallization from the melt. Of these we will make some remarks on particularly important papers. Strobl and coworkers [17, 28-30] have extensively studied the crystallization mechanisms both kinetically and morphologically, proposing a major rout of the melt crystallization where the melt transforms to lamellar crystals through a mesomorphic state of a liquid crystal-like structure and a granular crystal state (Figure 1.3).

Figure 1.4 represents in three related plots the route from the viewpoint of the corresponding changes in the chemical potential. The plots give the chemical potential per monomer, g, referred to that in the isotropic liquid, g_a. One has first to recognize that the chemical potential in layers is affected by their thickness. The dependence can be described by the Gibbs-Thomson equation, for both the lamellar crystallite and the mesomorphic layer. They were written for the crystal layer

$$g - g^a = (g^c - g^a) + \frac{a_{ac}}{d_c} \tag{1.2.5}$$

and for the mesomrohic layer

$$g - g^a = (g^m - g^a) + \frac{a_{am}}{d_m} \tag{1.2.6}$$

g_m and g_c describe the chemical potentials per monomer in the bulk of the mesomorphic and crystalline phases, respectively, the coefficients a_{ac} and a_{am} are proportional to the surface free energies associated with the two layers. We assume for the temperature range of crystallization

$$g^a < g^m < g^c \tag{1.2.7}$$

and

$$a_{am} < a_{ac} \tag{1.2.8}$$

Eq. (1.2.8) implies that not only the crystal phase is stable against the isotropic melt, but the mesomorhpic phase as well, although the latter is only metastable. Figure 1.4 refers to a certain crystallization temperature T_c. The lines in the plot on the left give the chemical potential in the lamellar crystals, in dependence on their (reciprocal) thickness d_c^{-1}. The lines with the lower slope in the right plot describe the same property for the monomers in mesomorphic layers with thickness d_m. The thickness at point A is the minimum thickness of the mesomorphic layer necessary to remain stable in the isotropic melt. Here the process starts and then continues along the path associated with the thickening. Thickening continues until

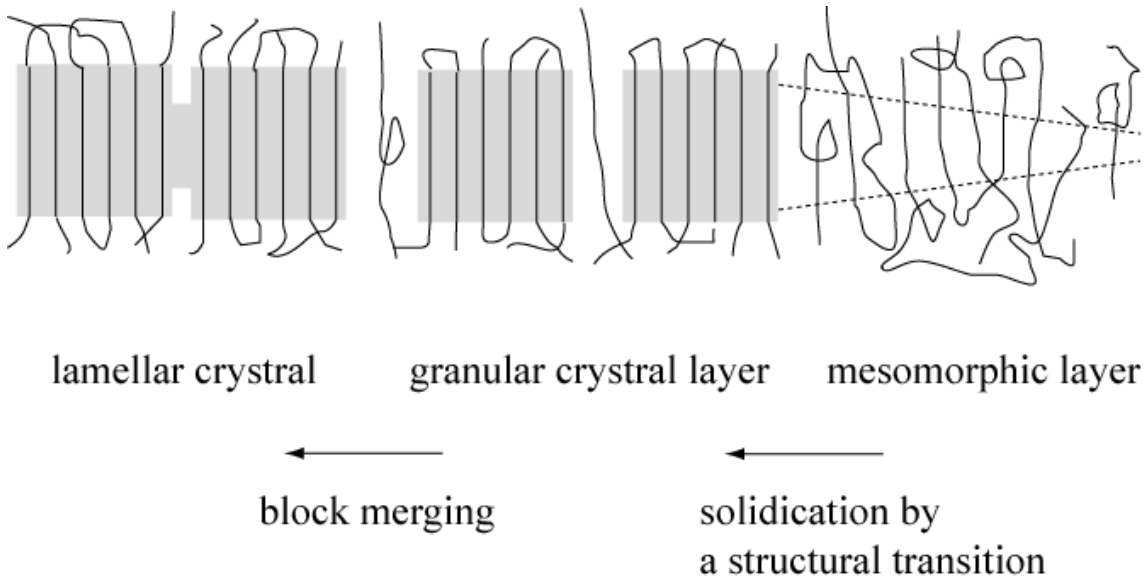

Figure 1.3. Sketch of the route proposed for the formation of polymer crystallites. Stages passed through as reflected in the structural states found along a layer [17].

point B is reached, where the layer solidifies. The transition occurs at a well-defined critical layer composed of blocks with an edge length $d_c \neq d_m$. The last step is the perfectioning and merging of the crystal blocks and this is formally described by the plot in the center. d_c remains unchanged, as the blocks just fuse together. The property varying along this section of the pathway is the degree of order within the layer. In order to formally describe this change we introduce a global "order parameter" ξ which plays the role of a reaction coordinate. It has an initial value ξ_i at the beginning of the perfectioning process at B, and ends up at unity when the perfect order of a homogeneous, laterally extended lamellar crystallite is reached. The chemical potential drops steadily along the path, down to its value at point C, which is the maximum gain in stability which can be acquired. The gain in stability along this section, *i.e.* from B to C, is much larger than that due to the mesomorhpic layer thickening, *i.e.* from A to B; the drawing does not show the real relation. The initial order parameter ξ_i varies with T_c, going up with increasing crystallization temperatures. As a consequence, the gain in the Gibbs free enthalpy gets smaller with increasing T_c. Point C shows up again in the left part of the drawing, now plotted on the Gibbs-Thomson line of the crystallites, at the position d_c^{-1}, which was already fixed by the size of the blocks.

Moreover, Strobl proposed the state diagram of polymer crystallization obtained from their experimental results (Figure 1.4). The melting line describes the thickness dependence of a phase transtion, that which leads from the crystalline to the isotropic amorphous state. Obviously the crystallization line has to be interpreted in an analogous way: It also represents the dc dependence of a structural transition, but since $T_c \neq T_f$, certainly another one between the crystalline and the amorphous state. Those parts of the structure which melt immediately above Tc experience exactly ehis transition. The state diagram in Figure 1.5 is therefore indication for a crysal development in two steps: Crystalites first appear in an initial form which then transforms into the final lamellar crytalite. The latter process provides the stabilization expressed by the temperature difference T_f - T_c and it occures without a change in d_c.

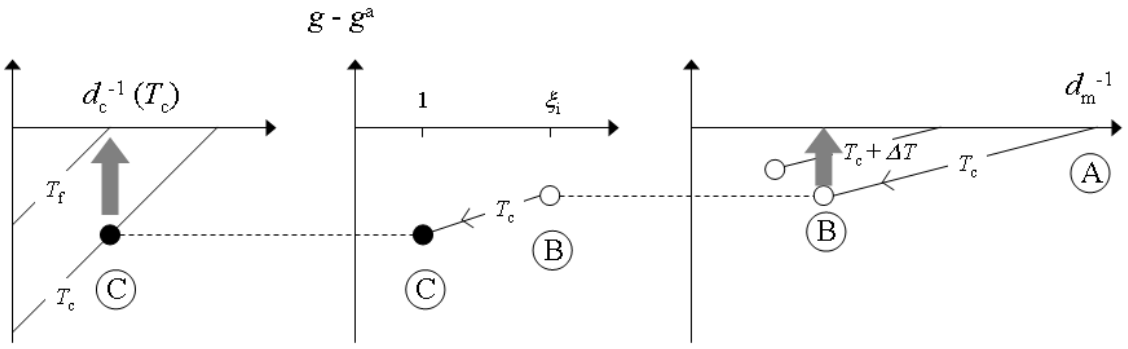

Figure 1.4. Variations of the chemical potential difference per monomer $g - g^a$ (g^a: chemical potential in the melt) along the route for a crystallization at T_c. Decrease due to the thickening of the mesomorphic layer, beginning with a minimum thickness at A, ending with the transition at B leading to a solidification (right). Decrease due to the perfectioning of the granular crystalline layer, described by a change of a global order parameter ξ from an initial ξ_i at B to unity at C (center). Chemical potential of homogeneous lamellar crystallites with the end point C being indicated (left). Grey arrows: Paths for the disaggregation of the blocks (right) and the melting of the lamellar crystallites (left) [17].

1.3. Crystallization of Isotactic Polypropylene via Mesophase and the Motivation of the Study

It is well known that isotactic polypropylene (iPP) forms the so-called mesophase by quenching the melt to a temperature below 0 °C, which is rater stable even at room temperarature. In addition, the mesophase of iPP crystallizes upon heating and the properties of the resultant crystal are very different from those obtained from the melt. The crystallization of iPP from the mesophase is also one of crystallization process via the intermediate state while the mesophase of iPP is rather stable compared with the intermediate states of other polymers. In this thesis we study the formation process of the mesophase as well as the crystallization process from the mesophase of iPP. Therefore, we describe the current situation of researches on the mesophase of iPP by reviewing the literatures to clarify the aim of this thesis.

The mesophase of isotactic polypropylene (iPP) has been researched by many researchers for a long time. The mesophase iPP is obtained by quenching molten amorphous iPP; empirically, this is achieved by dropping a thin piece of a sample rapidly into ice water [31]. The chain conformation in the mesophase iPP is the regular 3/1 helices of the isotactic chain configuration as well as the cases in the crystalline phases, such as the α-, β- and γ-forms [32]. On a crystallographic scale, the lateral chain arrangement in the mesophase iPP is less ordered than that in the crystalline phases but much better than that in the amorphous, as was characterized by two broad peaks in wide-angle X-ray diffraction (WAXD) pattern [33]. In conformity with the local structure, the level of stabilization energy of the mesophase iPP is also intermediate between that of amorphous and crystalline [34, 35]. On a mesoscopic scale, the mesophase iPP is cellulated into the granular particles, so-called “nodules” with a diameter of approximately 10 nm, as was revealed by small-angle X-ray scattering (SAXS), transmission electron microscopy (TEM) and atomic force microscopy (AFM) [36-40].

During quenching the sample, the sample experiences a cooling rate of the order of 100 °C/s. Specifically, the formation speed of the mesophase iPP is particularly high, and the formation process is completed over a short period of time. Extensive ex-situ analysis of the

transformation process to the mesophase of iPP has been performed [38, 41-46]. However, the ongoing process of mesophase formation has been a black box for many years, and in-situ observation of the formation process, which occurs in a very short period of time, has been challenging.

Initial in-situ observations were performed by a fast differential scanning calorimetric (fast DSC) technique [47], and an exothermal shoulder peak due to the mesophase formation was observed. In subsequent studies, an ultra-fast DSC technique successfully resolved two exothermal peaks due to crystallization and the mesophase formation [48]. The exothermal peak due to the mesophase formation is located between ca. -20 °C and ca. 35 °C, and the amount of the exotherm is comparable to that of crystallization. Thus, the formation of the mesophase of iPP is one of the solidification processes, which accompanies an exotherm (latent heat) sufficient to stabilize the mesophase at room temperature (above the T_g) [34, 35]. The understanding of the formation process of the mesophase iPP has progressed significantly as a result of thermal analysis.

From a structural point of view, the first in-situ observations of mesophase iPP formation were accomplished by heating from the glassy amorphous state, which is the reverse process of quenching from the molten amorphous state. Although it requires different techniques to obtain the glassy amorphous iPP rather than the mesophase iPP, the ex-situ preparation of the former was still possible with an ultra-quenching technique using cold ethanol or isopentane as a cooling medium [36, 37]. Once the glassy iPP is obtained below T_g, the progress of the mesophase formation can be controlled by slow heating. Thus, the development of the two broad peaks in WAXD and the broad peak in SAXS, which are characteristics of the mesophase iPP, were successfully observed [49]. Most recently, by using a propene/ethylene copolymer [50] to effectively delay the formation rate of the mesophase, in-situ observation of the formation process of the mesophase from the molten state has been achieved [51]. Thus, in-situ observation of the formation process of mesophase iPP has been challenging.

We would like to state the crystallization from mesophase in the next topic. The crystallization from the mesophase has been extensively studied in the literature [37, 40, 52-55]. Nishida *et al*. have ever found that the large crystal grains of several tens micrometer having “bamboo leaf-like (BL)” morphology were produced by a rapid heating from the mesophase of isotactic polypropylene (iPP) [53, 54].

Crystallization of polymer in bulk usually results in the formation of spherulite, the diameter of which often reaches into several tens micrometer. However, the spherulite is not a single crystal. The reason is the generation of the overgrowth of, for example, lamellar stack and cross-hatches significantly [56-60]. Geil observed single crystals in the β-form of hexagonal unit cell and also reported α-form dendritic ribbon consisted with broad thick ribbon and lateral branches [61]. It is known that α-iPP forms cross-hatches occurred at the early stage of crystallization from the melt. Therefore, quadrites were formed easily with the cross-hatted lamellae [61]. Thus, it has been quite difficult to obtain the isolated α-form single crystals of iPP grown from the melt. On the other hand, generation of large BL crystals is specific phenomena in bulk crystallization.

The mesophase as the initial state must be essential for this particular crystallization. Furthermore, the “rapid heating” in the crystallization process from mesophase should be also deeply associated with the generation of the BL crystal, because a cold crystallization from the mesophase of iPP with a slow heating just resulted in the formation of the nodular crystallites [39]. However, the condition to generate the BL crystal is unclear due to technical difficulty of controlling the rapid heating rate.

As shown above, there still remain many unsolved problems on the mesophase of iPP. In the thesis, therefore, we have aimed at clarifying the formation mechanism of the mesophase and crystallization mechanism from the mesophase of iPP during the heating process to find a new route to control the higher order structure of iPP.

1.4. Basic Principles of Measurements in This Thesis

In this section we describe briefly the basic principles and some experimental techniques used in the thesis; basic principles of scattering and de-polarized light transmission. These give us a basis for understanding the results obtained in this thesis.

1.4.1. Basic Principles of Scattering Experiments

Scattering theory is the most important tools for learning about the structure and the interactions of atomic, nuclear, and sub-nuclear system. In order to give the basis to understand the experimental results presented at some chapters in this thesis, the fundamental of scattering methods are summarized in this section [62].

Depending on the system under study and the desired resolution, photons in the X-ray and light scattering range, or neutrons are used. The general set up of a scattering experiment is indicated schematically in Figure 1.5. There is an incident beam of monochromatic radiation with wavelength λ and an intensity I_0. It becomes scattered by a specimen and the intensity I of the scattered waves is registered by a detector (D) at a distances A, under variation of the direction of observation. Employing the 'scattering vector' $\boldsymbol{q}$, defined

$$\boldsymbol{q} := \boldsymbol{k_f} - \boldsymbol{k_i} \tag{1.4.1}$$

where $\boldsymbol{k_f}$ and $\boldsymbol{k_i}$ denote the wave vectors of the incident and the scattered plane waves, the result of a scattering experiment is usually expressed by giving the 'intensity distribution in $\boldsymbol{q}$ – space', $I(\boldsymbol{q})$. In the majority of scattering experiments on polymers the radiation frequency remains practically unchanged. Then, we have

$$|\boldsymbol{k_f}| \approx |\boldsymbol{k_i}| = 2\pi/\lambda \tag{1.4.2}$$

and $|\boldsymbol{q}|$ is related to the 'Bragg scattering angle' θ_B by

$$|\boldsymbol{q}| = 4\pi/\lambda \sin \theta_B \tag{1.4.3}$$

Hence, the scattering amplitude produced by a set of particles at locations $\boldsymbol{r_i}$ is formulated as

$$C(\boldsymbol{q}) = \sum_{i=1}^{N_m} \exp i\boldsymbol{q}\boldsymbol{r_i} \tag{1.4.10}$$

The scattering intensity, $I(\boldsymbol{q})$ is proportional to the squared modulus of C.

$$I(\boldsymbol{q}) \sim \langle |C(\boldsymbol{q})|^2 \rangle \tag{1.4.11}$$

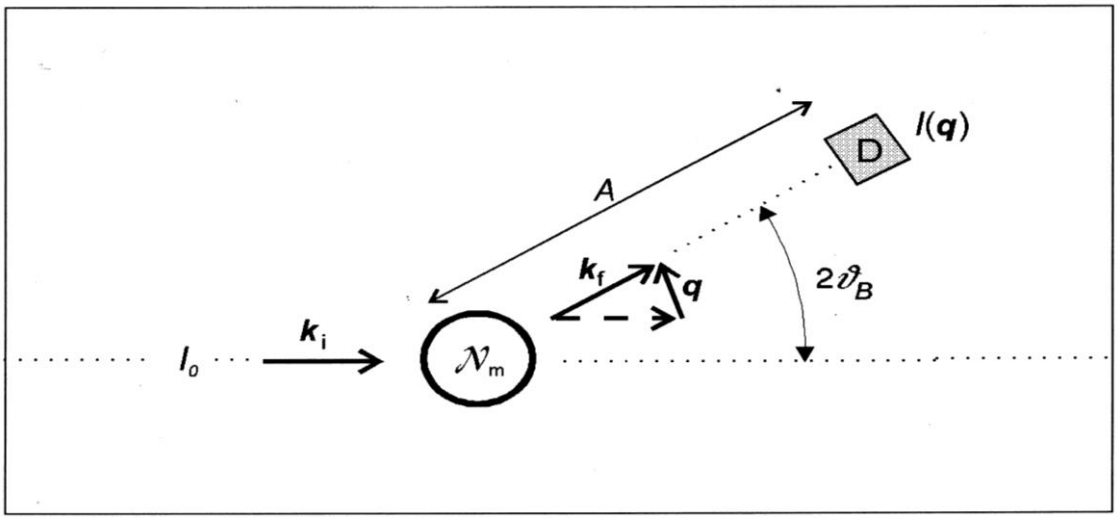

Figure 1.5. General set-up of a scattering experiment.

There two different functions can be used for representing scattering data in reduced form. The first one is the difficult scattering cross–section per unit volume of the sample, $\Sigma(\boldsymbol{q})$ described as:

$$\Sigma(\boldsymbol{q}) := 1/V\,(\mathrm{d}\sigma/\mathrm{d}\Omega) = 1/V\,I(\boldsymbol{q})\,A^2/I_0 \tag{1.4.4}$$

This function is called the 'Rayleigh–ratio'. While the effect of the volume is removed, $\Sigma(\boldsymbol{q})$ remains dependent on the scattering power of the particles in the sample, which varies with the applied radiation. For X-rays, the scattering power is related to the electron densites. The second one is interference function, $S(\boldsymbol{q})$, also called 'scattering function' or 'scattering law', which is defined as

$$S(\boldsymbol{q}) := I(\boldsymbol{q})/I_\mathrm{m}/N_\mathrm{m} \tag{1.4.5}$$

Here N_m represents the total number of particles/monomers in the samples, and I_m is the scattering intensity produced by one particle, if placed in the same incident beam. The interference function expresses the ratio between the actual intensity and the intensity which would be measured, if all particles in the sample were to scatter incoherently.

It thus indeed describes the interference effect. The relationship between $\Sigma(\boldsymbol{q})$ and $S(\boldsymbol{q})$ is described by the equation as

$$\Sigma(\boldsymbol{q}) = \Omega\,\langle c_\mathrm{m}\rangle\,(\mathrm{d}\sigma/\mathrm{d}\Omega)_\mathrm{m}\,S(\boldsymbol{q}) \tag{1.4.6}$$

Here $(\mathrm{d}\sigma/\mathrm{d}\Omega)_\mathrm{m}$ denotes the scattering section per particle of monomer and $\langle c_\mathrm{m}\rangle$ stands for their mean density

$$\langle c_m\rangle = N_m/V \tag{1.4.7}$$

Scattering diagrams generally emerge from the susperposition and interface of the scattered waves at the point of registration by the detector in normalized form are described by complex numbers of modulus unity and phases φ_i , the total scattering amplitude is obtained as

$$C = \sum_{i=1}^{N_m} \exp \mathrm{i}\varphi_\mathrm{i} \tag{1.4.8}$$

The phases φ_i are simply determined by the particle positions $\boldsymbol{r}_\mathbf{i}$ and the scattering vector $\boldsymbol{q}$ only, being given by

$$\varphi_i = \boldsymbol{q}\boldsymbol{r}_\mathbf{i} \tag{1.4.9}$$

As the normalization of the amplitudes of the single scattered waves is already implied in the definition of the interference function Eq.(1.4.5), Eq.(1.4.11) is completed to

$$S(\boldsymbol{q}) = 1/N_m \langle \mid C(\boldsymbol{q}) \mid^2 \rangle \tag{1.4.12}$$

This is a basic equation of general validity and it may serve as starting point for the derivation of other forms of scattering equations. The calculation of the squared scattering amplitude is following. A first formula given directly by insertion of Eq. (1.4.10), leading

$$S(\boldsymbol{q}) = 1/N_m \sum_{j=1}^{N_m} \langle \exp \mathrm{i}\boldsymbol{q}(\boldsymbol{r}_\mathbf{i} - \boldsymbol{r}_\mathbf{j}) \rangle \tag{1.4.13}$$

Instead of specifying the discrete $\boldsymbol{r_i}$ positions of all particles, one can also use a continuum description and introduce the particle density distribution $c_\mathrm{m}(\boldsymbol{r})$. The scattering amplitude for a single microstate, as represented by the association density distribution described as

$$C(\boldsymbol{q}) = \int_V \exp \mathrm{i}\boldsymbol{q}\boldsymbol{r}\, (\boldsymbol{c}_\mathbf{m}(\boldsymbol{r}) - \langle c_\mathrm{m} \rangle)\, \mathrm{d}^3\boldsymbol{r} \tag{1.4.14}$$

As scattering occurs only, if c_m varies within the sample, the mean value, $\langle c_\mathrm{m} \rangle$ is subtracted, thus relating the scattering directly to the fluctuation. $C(\boldsymbol{q})$ equals the Fourier-transform of the fluctuations in the particle density.

Insertion of Eq. (1.4.14) into (1.4.12) and carrying out the ensemble average yields

$$S = \int_V \int_V \exp \mathrm{i}\boldsymbol{q}(\boldsymbol{r}' - \boldsymbol{r}'') \langle (\boldsymbol{c}_\mathbf{m}(\boldsymbol{r}') - \langle c_\mathrm{m} \rangle)\, (\boldsymbol{c}_\mathbf{m}(\boldsymbol{r}'') - \langle c_\mathrm{m} \rangle) \rangle\, \mathrm{d}^3\boldsymbol{r}'\, \mathrm{d}^3\boldsymbol{r}'' \tag{1.4.15}$$

For macroscopically homogeneous system, where

$$\langle \boldsymbol{c_m}(\boldsymbol{r}')\, \boldsymbol{c_m}(\boldsymbol{r}'') \rangle = \langle \boldsymbol{c_m}(\boldsymbol{r}' - \boldsymbol{r}'')\, \boldsymbol{c_m}(0) \rangle \tag{1.4.16}$$

This equation can be reduced to a single integral. Substitution of $\boldsymbol{r}' - \boldsymbol{r}''$ by $\boldsymbol{r}$ yields

$$S(\boldsymbol{q}) = \int_V \exp \mathrm{i}\boldsymbol{q}\boldsymbol{r} \langle \langle \boldsymbol{c_m}(\boldsymbol{r})\, \boldsymbol{c_m}(0) \rangle - \langle c_\mathrm{m} \rangle \rangle\, \mathrm{d}^3\boldsymbol{r} \tag{1.4.17}$$

This equation expresses $S(\boldsymbol{q})$ as the Fourier-transform of the space dependent correlation function of the particle density.

A third form the basic scattering equation is obtained if structures are characterized with the aid of the pair distribution function, $g(\boldsymbol{r})$. Per definition, the product $g(\boldsymbol{r})\ \mathrm{d}^3\boldsymbol{r}$ gives the probability that starting from a given particle, the particle itself or some other particle is found in the volume element $\mathrm{d}^3\boldsymbol{r}$ at a distance $\boldsymbol{r}$. The pair distribution function $g(\boldsymbol{r})$ is composed of two parts; the self–contribution, $\delta(\boldsymbol{r})$ and the contributions of the other particles, $g'(\boldsymbol{r})$. For fluid systems with short – range order, the limiting value of the pair distribution function, $g(\boldsymbol{r})$

at large distance ($r \to \infty$) equals the mean density $\langle c_m \rangle$. As follows directly from the definition, density distribution and pair distribution function are related by

$$\langle \boldsymbol{c}_m(\boldsymbol{r})\, \boldsymbol{c}_m(0) \rangle = \langle c_m \rangle\, g(\boldsymbol{r}) \tag{1.4.18}$$

Insertion the equation in Eq.(1.4.17) gives

$$S(\boldsymbol{q}) = \int_V \exp i\boldsymbol{q}\boldsymbol{r}\, (g(\boldsymbol{r}) - \langle c_m \rangle)\, d^3\boldsymbol{r} \tag{1.4.19}$$

Once again, the scattering function equals a Fourier-transform, now of the pair distribution function. From Eq.(1.4.19) there follows the asymptotic value of S for large values of $\boldsymbol{q}$. In the limit $\boldsymbol{q} \to \infty$ only the contribution of the self-correlation part, $\delta(\boldsymbol{r})$, is left, and found that $S(\boldsymbol{q} \to \infty) \to 1$. It can be concluded that, for large $\boldsymbol{q}$, there are neither constructive nor destructive interferences between the particles so that they behave like incoherent scatters.

For isotropic systems with $g(\boldsymbol{r}) = g(r := |\boldsymbol{r}|)$, the scattering function is also isotropic $S(\boldsymbol{r}) = S(q := |\boldsymbol{q}|)$. The Fourier-relation between $g(r)$ and $S(r)$ then has the form

$$S(q) = \int_{r=0}^{\infty} \frac{\sin qr}{qr}\, 4\pi r^2\, (g(\boldsymbol{r}) - \langle c_m \rangle)\, d\boldsymbol{r} \tag{1.4.20}$$

In this section, it was formulated three equivalent relations, Eq.(1.4.13), (1.4.17) and (1.4.19), which may be employed in the evaluation of scattering data. All three equations express a Fourier–relation between $S(q)$ and functions which describe properties of the microscopic structure in statistical terms.

1.4.2. Basic Principles of De-polarized Light Transmission

Basic principles of de-polarized light transmission (DPLT) are similar to those of polarized optical microscope. The principle is that phase difference caused by light passing through optical anisotropic body is changed into contrast in measurements [63]. However, optical system for polarized optical microscope has imaging plane while the optical system for DPLT does not.

A polarizing plate for incident light is called polarizer, and that for transmitted light is called analyzer. The polarizer allows the incident light with vibration plane in a specific direction to pass, resulting in polarized light. Figure 1.6 shows the schematic description of vibration direction of light under cross Nicol before and after a sample. In the figure, the vibration plane of the light passed through the polarizer is horizontal to this paper. When the analyzer is inserted vertically to the polarizer in this light path, and then de-polarized intensity become zero if no oriented body is between the polarizer and the analyzer.

When an optically anisotropic specimen is under cross Nicol, incident light is divided into two refracted lights whose vibration directions are mutually perpendicular. The phenomenon is called birefringence. In the case of uniaxial crystal such as tetragonal and hexagonal crystals, one refracted light is independent of the propagation directions, and its velocity and refractive index is constant. On the other hand, the velocity and refractive index of the other depends on the propagation directions. The former is called ordinary light, and the latter is called extraordinary light. In the case of biaxial crystal such as orthorhombic and monoclinic crystals, both of the divided refracted lights are all extraordinary lights.

Here we assume the directions of vibration with the large and small refractive indices are $\boldsymbol{Z'}$ and $\boldsymbol{X'}$, respectively, and the angle between $\boldsymbol{Z'}$ and the polarizer $\boldsymbol{P}$ is θ (Figure 1.7). When the amplitude of light passed through the polarizer is Op, the amplitudes of the lights passing through the sample in the directions of $\boldsymbol{Z'}$ and $\boldsymbol{X'}$ are given by

$\boldsymbol{Z'}$ direction: $\mathrm{Om} = \mathrm{Op} \cos\theta$ (1.4.21)

$\boldsymbol{X'}$ direction: $\mathrm{Om} = \mathrm{Op} \sin\theta$ (1.4.22)

In the light with vibration in $\boldsymbol{Z'}$ direction, the amplitude is given by

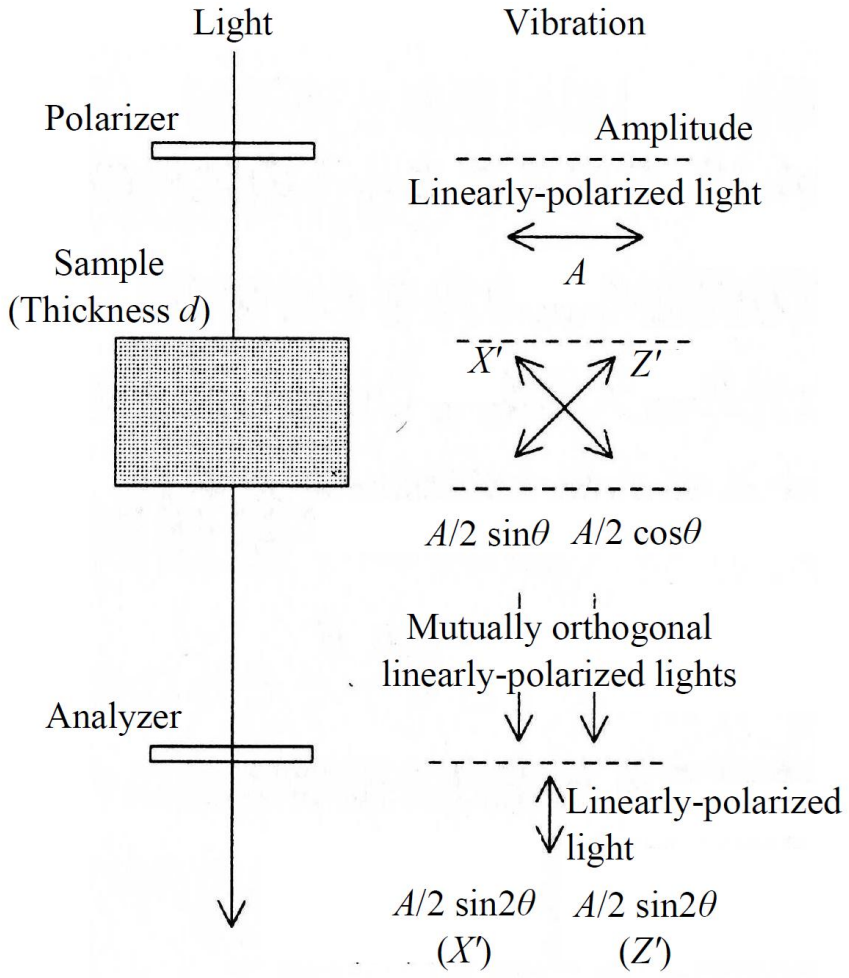

Figure 1.6. Vibration direction of light under cross Nicol.

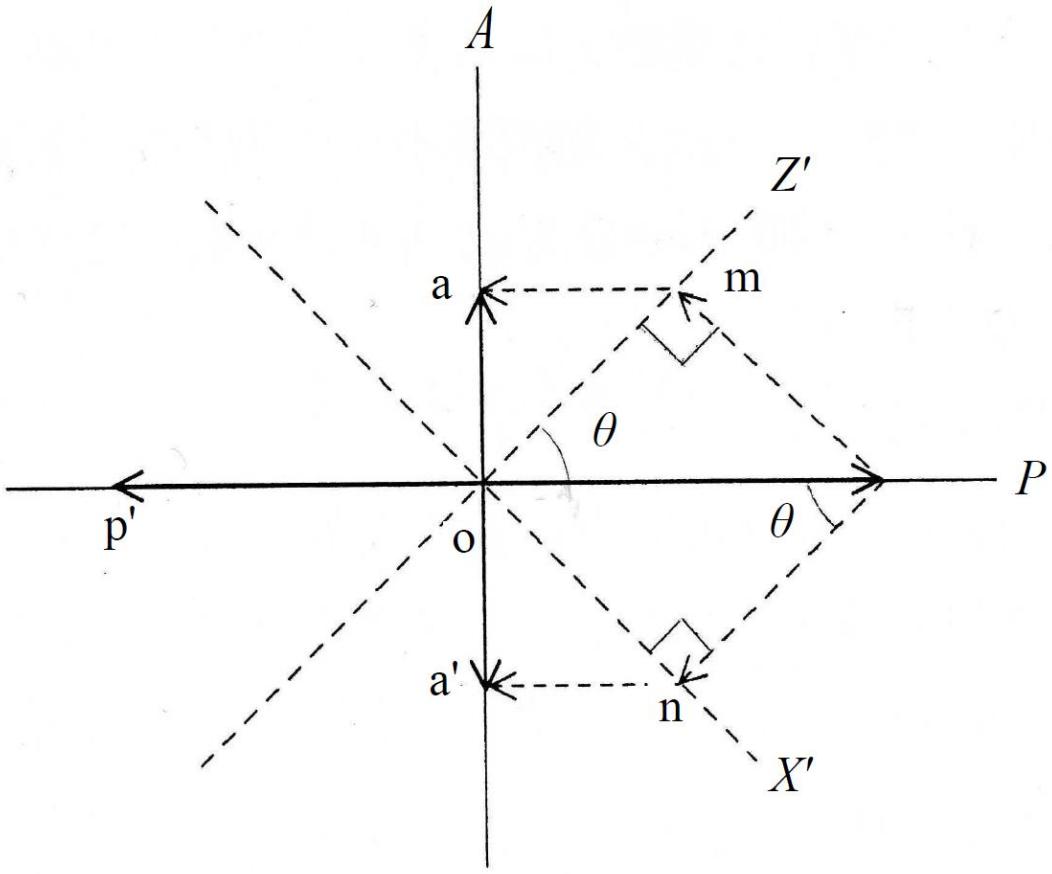

Figure 1.7. Relation between directions of samples and polarizer.

$$(Oa)_{Z'} = Om \sin\theta = OP \cos\theta \sin\theta = (Op/2) \sin 2\theta \quad (1.4.23)$$

In the light with vibration in ***X'*** direction, the amplitude is also given by

$$(Oa')_{X'} = Om \cos\theta = OP \sin\theta \cos\theta = (Op/2) \sin 2\theta \quad (1.4.24)$$

In the case of biaxial crystal, two extraordinary lights (1.4.23) and (1.4.24) are synthesized in passing through the analyzer. The amplitudes of both of the lights in ***Z'*** and ***X'*** directions are (Op/2) sin 2θ. However, the amplitude of the synthesized light is not (Op/2) sin 2θ because of the phase difference between them.

Figure 1.8 shows schematic drawing to explain the phase difference under cross Nicol. It is assumed that the fast light in ***X'*** direction has wavelength λ_1 and refractive index n_1 in the sample and the slow light in ***Z'*** direction has wavelength λ_2 and refractive index n_2. The light in ***Z'*** direction is gradually delayed during propagation. When the light in ***Z'*** direction gets out of the sample, the light in ***X'*** direction propagates ahead in the air by $R = \lambda_0 \{d/\lambda_2 - d/\lambda_1\}$. The relation between refractive index n and wavelength λ is expressed as $\lambda = \lambda_0/n$, and hence R is given by

$$R = d\,(n_2 - n_1) \quad (1.4.25)$$

where d is the thickness of the sample. R is called retardation and represents the delay of the light after passing through the oriented sample. Therefore, the phase difference between the fast light and the slow light is given by $\delta = 2\pi d\,(n_2 - n_1)/\lambda_0$. Generally speaking, orthogonal two refracted lights results in elliptically–polarized light. However, for simplicity, here we treat it as two separated linearly-polarized lights. When the two linearly-polarized lights enter the analyzer, the waves y_1 and y_2 are expressed by equation (1.4.26).

$$y_1 \equiv A_1 \sin\{((2\pi t)/T)\},\ y_2 \equiv A_2 \sin\{((2\pi t)/T) - \delta\} \quad (1.4.26)$$

where T is the period. Using the phase difference $\eta\ (= \delta - \pi)$ the synthesized light is given by

$$y_3 = y_1 + y_2 \equiv A_3 \sin\{((2\pi t)/T) - \eta\} \quad (1.4.27)$$

Hence, square of the amplitude of the synthesized light of the two refracted lights is given by

$$A_3^2 = (Op/2)^2 \sin^2 2\theta\,(1 + \cos(\delta'/2)) \quad (1.4.28)$$

The equation (1.4.28) corresponds to intensity obtained by DPLT measurements.

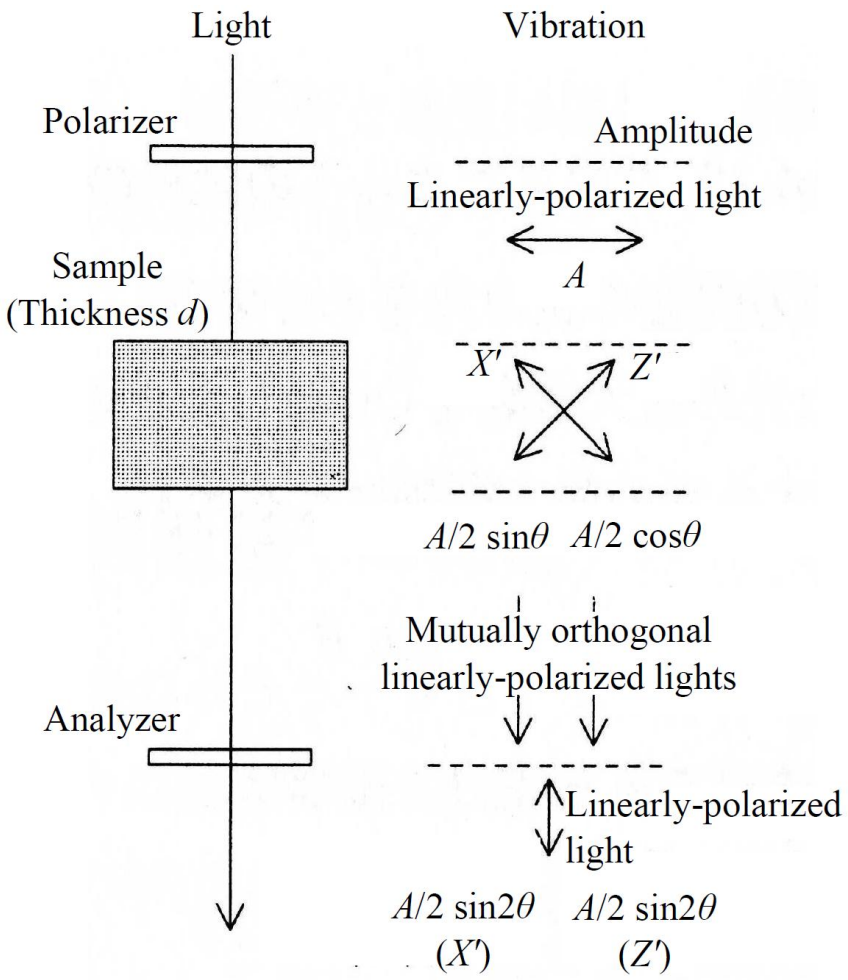

Figure 1.8. Scheme of vibration direction of light under cross nikol in putting the samples.

1.5. Outline of This Thesis

In Chapter 2, in-situ observation of the formation process of mesophase of iPP is reported from a structural point of view. A very rapid transformation from the molten state to the mesophase has, made in-situ observation difficult. In the present study, a rapid temperature jump and high-flux synchrotron radiation X-ray scattering techniques were combined effectively to observe this transformation. Fast time-resolved wide-angle X-ray diffraction (WAXD) during the rapid cooling clearly shows the time-evolution of the transformation process of the mesophase from the molten state. It was found that the transformation proceeded very quickly in a narrow temperature range below ca. 35 °C. Furthermore, the transformation was accompanied by instantaneous density fluctuations throughout the system, as visualized by microscopic observations. These observations suggest that the mesophase formation proceeds similarly to spinodal decomposition.

In Chapter 3, energy level of the mesophase (metastable state) of iPP is examined by comparing the fractions of α-crystal, mesophase and amorphous phase obtained in WAXD and DSC measurements during the heating process. It was found that the ratio of the melting enthalpy of mesophase to that of α-crystal was 0.75.

In Chapter 4, apart from iPP, mesophase of poly(butylene-2,6-naphthalate) (PBN) is studied, especially focusing on the energy level of the mesophase of PBN. The same method as that used in Chapter 3 was applied to estimate the energy level; the fractions of α-crystal, mesophase and amorphous phase were obtained in WAXD measurements during the heating process, and compared the WAXD results with those in the DSC ones. It was found that the ratio of the melting enthalpy of mesophase to that of α-crystal was 0.70 for PBN.

In Chapter 5, heating rate effects on the crystallization behavior from the mesophase of iPP is examined by utilizing a de-polarized light transmission (DPLT) method to find optimal condition to generate the BL crystals. The DPLT sensitively detected the crystal grain growth in a narrow temperature region just below the melting temperature. With increasing the heating rate, both the temperature regions of the cold crystallization and the crystal grain growth shifted toward the higher temperatures. When the heating rate was slow below

20 °C/min, the crystal grain growth was not conspicuous. With increasing the heating rate, the rate of the crystal grain growth increased and showed a maximum when the heating rate was approximately 60-80 °C/min. However, excessively fast heating above 100 °C/min also suppressed the crystal grain growth.

In Chapter 6, the condition to generate large single crystals is studied using optical microscope and DSC. The giant single crystals of iPP were obtained by a specific kinetic path through the mesophase of iPP; pre-quenched mesophase of iPP was heated to 164 °C at a rate of 75 °C/min and kept at 164 °C for 24 h. The obtained crystallites showed a very high melting temperature T_m at 186 °C, which is ca. 20 °C higher than the iPP's nominal T_m (= ca. 165 °C); namely the observed T_m is immediately near the iPP's equilibrium melting temperature T_m^0 (= 186.2 °C). The crystallites have bamboo leaf-like (BL) or needle-like morphology having ca. 40 μm in length and ca. 3 μm in width. The thickness of the crystallites was estimated to be approximately 90 nm according to the melting temperature. The number density of the crystallites in a unit volume was controlled by adjusting the heating rate. As the result, well-isolated single crystals of iPP having the above-mentioned morphology were obtained. Finally, the whole results and discussions in the thesis are summarized.

References

1. Basset, D.C. *Principles of Polymer Morphology*, 1-259, (Cambridge University Press, Cambridge, 1981).
2. Lauritzen, J. I. & Hoffman, J. D. Extension of theory of growth of chainfolded polymer crystals to large undercoolings. *J. Appl. Phys.* **44**, 4340-4352 (1973).
3. Imai, M., Mori, K., Mizukami, T., Kaji, K. & Kanaya, T. Structural formation of poly(ethylene terephthalate) during the induction period of crystallization: 1. Ordered structure appearing before crystal nucleation. *Polymer* **33**, 4451-4456 (1992).
4. Imai, M., Mori, K., Mizukami, T., Kaji, K. & Kanaya, T. Structural formation of poly(ethylene terephthalate) during the induction period of crystallization: 2. Kinetic analysis based on the theories of phase separation. *Polymer* **33**, 4457-4462 (1992).
5. Matsuba, G., Kaji, K., Nishida, K., Kanaya, T. & Imai, M. Conformational change and orientation fluctuations prior to the crystallization of syndiotactic polystyrene. *Macromolecules* **32**, 8932-8937 (1999).
6. Ezquerra, T.A., Lopez-Cabarcos, E., Hsiao, B. S. & Balta-Calleja, F. Precursors of crystallization via density fluctuations in stiff-chain polymers. *Phys. Rev. E* **54**, 989-992 (1996).
7. Akpalu, Y., Kiehorn, L., Hsiao, B. S., Stein, R. S., Russell, T. P., van Egmond, J. & Muthukumar, M. Structure development during crystallization of homogeneous copolymers of ethane and 1-octene: Time-resolved synchrotron X-ray and SALS measurements. *Macromolecules* **32**, 765-770 (1999).
8. Heeley, E. L., Maidens, A. V., Olmsted, P. D., Bras, W., Dolbnya, I. P., Fairclough, J. P. A., Terrill, N. J. & Ryan, A. J. Early stages of crystallization in isotactic polypropylene. *Macromolecules* **36**, 3656-3665 (2003).
9. Tashiro, K., Sasaki, S., Gose, N. & Kobayashi, M. Microscopically-viewed structural change of polyethylene during isothermal crystallization from the melt I. Time-resolved FT-IR spectral measurements. *Polym. J.* **30**, 485-491 (1998).

10. Fukao, K. & Miamoto, Y. Dynamical transition and crystallization of polymers. *Phys. Rev. Lett.* **79**, 4613-4616 (1997).
11. Imai, M., Kaji, K. & Kanaya, T. Orientation fluctuations of poly(ethylene terephthalate) during the induction period of crystallization. *Phys. Rev. Lett.* **71**, 4162-4165 (1993).
12. Imai, M., Kaji, K. & Kanaya, T. Structural formation of poly(ethylene terephthalate) during the induction period of crystallization. 3. Evolution of density fluctuations to lamellar crystal. *Macromolecules* **27**, 7103-7108 (1994).
13. Imai, M., Kaji, K., Kanaya, T. & Sakai, Y. Ordering process in the induction period of crystallization of poly(ethyleneterephthalate). *Phys. Rev. B* **52**, 12696-12704 (1995).
14. Imai, M., Kaji, K., Kanaya, T. & Sakai, Y. Chain conformation in the induction period of crystallization of poly(ethylene terephthalate). *Physica B* **213-214**, 718-720 (1995).
15. Matsuba, G., Kaji, K., Kanaya, T. & Nishida, K. Detailed analysis of the induction period of polymer crystallization by depolarized light scattering. *Phys. Rev. E* **65**, [061801-1]-[06180-7] (2002).
16. Olmsted, P. D., Poon, W. C. K., McLeish, T. C. B., Terrill, N. J. & Ryan, A. J. Spinodal-assisted crystallization in polymer melts. *Phys. Rev. Lett.* **81**, 373-376 (1998).
17. Strobl, G. From the melt via mesomorphic and granular crystalline layers to lamellar crystallites: A major route followed in polymer crystallization? *Eur. Phys. J. E* **3**, 165-183 (2000).
18. Muthukmar, M. Molecular modeling of nucleation in polymer. *Phil. Trans. R. Soc. Lond. A* **361**, 539-556 (2003).
19. Okui, T. *Koubunshi no kesshou* (*Crystals in Polymers*), 1-93 (Kyoritsu Shuppan, Tokyo, 1993).
20. Hikosaka, M. Unified theory of nucleation of folded-chain crystals and extended-chain crystals of linear-chain polymers. *Polymer* **28**, 1257-1264 (1987).
21. Hikosaka, M. Unified theory of nucleation of folded-chain crystals (FCCs) and extended-chain crystals (ECCs) of linear-chain polymers: 2. Origin of FCC and ECC. *Polymer* **31**, 458-468 (1990).

22. Allegra, G. Chain folding and Polymer crystallization: A statistical-mechanical approach. *J. Chem. Phys*. **66**, 5453-5463 (1977).
23. Lee, S., Miyaji, H. & Geil, P. H. Morphology of amorphous polyethylene terephthalate. *J. Macromol. Sci., Part B*: *Phys*. **22**, 489-496 (1983).
24. Doi, M. & Edwards, S. F. The theory of polymer dynamics, 1-408 (Oxford, New York, 1986).
25. Shimada, T., Doi, M. & Okano, K. Concentration fluctuation of stiff polymers. I. Static structure factor. *J. Chem. Phys*. **88**, 2815-2821 (1988).
26. Doi, M., Shimada, T. & Okano, K. Concentration fluctuation of stiff polymers. II. Dynamical structure factor of rodlike polymers in the isotropic phase. *J. Chem. Phys*. **88**, 4070-4075 (1988).
27. Doi, M., Shimada, T. & Okano, K. Concentration fluctuation of stiff polymers. III. Spinodal decomposition. *J. Chem. Phys*. **88**, 7181-7186 (1988).
28. Hauser, G., Schmidtke, J. & Strobl, G. The role of co-units in polymer crystallization and melting: New insights from studies on syndiotactic poly(propene-co-octene). *Macromolecules* **31**, 6250-6258 (1998).
29. Hugel, T., Stroble, G. & Thomann, R. Building lamellae from blocks: The pathway followed in the formation of crystallites of syndiotactic polypropylene. *Acta. Polym*. **50**, 214-217 (1999).
30. Iijima, M. & Strobl, G. Isothermal crystallization and melting of isotactic polproplene analyzed by time- and temperature-dependence small-angle X-ray scattering experiments. *Macromolecules* **33**, 5204-5214 (2000).
31. Miller, R. L. On the existence of near-range order in isotactic polypropylenes. *Polymer* **1**, 135-143(1960).
32. Turner-Jones A., Aizlewood J. M. & Beckett D. R. Crystalline forms of isotactic polypropylene. *Makromol. Chem.* **75,** 134-158 (1964).
33. Natta, G. Progress in five years of research in stereospecific polymerization. *SPE. J.* **15**,373-382 (1959).

34. Grebowicz, J., Lau, S.-F. & Wunderlich, B. The thermal properties of polypropylene. *J. Polym. Sci., Polym. Symp.* **71**, 19-37 (1984).
35. Cao, J. & Sbrrarski, I. Determination of the enthalpy of solid phase transition for isotactic polypropylene using a modified DSC technique. *Polymer* **47**, 27-31 (2006).
36. Ogawa, T., Miyaji, H. & Asai, K. Nodular structure of polypropylene. *J. Phys. Soc., Jpn.* **54**, 3668-3670 (1985).
37. Hsu, C. C., Geil, P. H., Miyaji, H. & Asai, K. Structure and properties of polypropylene crystallized from the glassy state. *J. Polym. Sci., Part B: Polym. Phys.* **24**, 2379-2401 (1986).
38. Zia, Q., Androsch, R., Radusch, H.-J. & Piccarolo, S. Morphology, reorganization and stability of mesomorphic nanocrystals in isotactic polypropylene. *Polymer* **47**, 8163-8172 (2006).
39. Zia, Q., Radusch, H.-J. & Androsch, R. Direct analysis of annealing of nodular crystals in isotactic polypropylene by atomic force microscopy, and its correlation with calorimetric data *Polymer* **48**, 3504-3511 (2007).
40. Androsch, R. In situ atomic force microscopy of the mesomorphic-monoclinic phase transition in isotactic polypropylene. *Macromolecules* **41**, 533-535 (2008).
41. Piccarolo, S., Saiu, M., Brucato, V. & Titomanlio, G. Crystallization of polymer melts under fast cooling. II. High-purity iPP. *J. Appl. Polym. Sci.* **46**, 625-634 (1992).
42. Choi, C.-H. & White, J. L. Correlation and modeling of the occurrence of different crystalline forms of isotactic polypropylene as a function of cooling rate and uniaxial stress in thin and thick parts. *Polym. Eng. Sci.* **40**, 645-655 (2000).
43. Brucato, V., Piccarolo, S. & Carrubba, V. L. An experimental methodology to study polymer crystallization under processing conditions. The influence of high cooling rates. *Chem. Eng.Sci.* **57** 4129-4143 (2002).
44. Coccorullo, I., Pantani, R. & Titomanlio, G. Crystallization kinetics and solidified structure in iPP under high cooling rates. *Polymer* **44**, 307–318 (2003).

45. Konishi, T., Nishida, K., Kanaya, T. & Kaji, K. Effect of isotacticity on formation of mesomorphic phase of isotactic polypropylene. *Macromolecules* **38**, 8749-8754 (2005).
46. Li, L. & de Jeu, W. H. Shear-induced smectic ordering and crystallisation of isotactic polypropylene. *Faraday Discuss*. **128**, 299–319 (2005).
47. Wu, Z. Q., Dann, V. L., Cheng, S. Z. D. & Wunderlich, B. Fast DSC applied to the crystallization of polypropylene. *J. Therm. Anal.* **34**, 105-114 (1988).
48. Gradys, A., Sajkewicz, P., Minakov, A. A., Adamovsky, S., Schick, C., Hashimoto, T. & Saijo, K. Crystallization of polypropylene at various cooling rates. *Mater. Sci. Eng. A* **413-414**, 442-446 (2005).
49. Miyamoto, Y., Fukao, K., Yoshida, T., Tsurutani, N. & Miyaji, H. Structure formation of isotactic polypropylene from the glass. *J. Phys. Soc. Jpn.* **69**, 1735-1740 (2000**)**.
50. Cavallo, D., Azzurri, F., Floris, R., Alfonso, G. C., Balzano, L. & Peters, G. W. Continuous cooling curves diagrams of propene/ethylene random copolymers. The role of ethylene counits in mesophase development. *Macromolecules* **43**, 2890–2896 (2010).
51. Cavallo, D., Portale, G., Balzano, L., Azzurri, F., Bras, W., Peters, G. W. & Alfonso, G. C. Real-time WAXD detection of mesophase development during quenching of propene/ethylene copolymers. *Macromolecules* **43**, 10208-10212 (2010).
52. Wang, Z. G., Hsiao, B. S., Srinivas, S., Brown, G. M., Tsou, A. H., Cheng, S. Z. D. & Stein, R. S. Phase transformation in quenched mesomorphic isotactic polypropylene. *Polymer* **42**, 7561-7566 (2001).
53. Nishida, K., Konishi, T., Kanaya, T. & Kaji, K. Novel morphology of isotactic polypropylene crystal generated by a rapid temperature jump method. *Polymer* **45**, 1433–1437 (2004).
54. Konishi, T., Nishida, K. & Kanaya, T. Crystallization of isotactic polypropylene from prequenched mesomorphic phase. *Macromolecules* **39**, 8035-8040 (2006).
55. Zhao, J., Qiu, J., Niu, Y. & Wang, Z. Evolutions of morphology and crystalline ordering upon annealing of quenched isotactic polypropylene. *J. Polym. Sci., Part B: Polym. Phys.* **47**, 1703-1712 (2009).

56. Natta, G. & Corradini, P. Structure and properties of isotactic polypropylene. *Nuovo Cimento Suppl.* **15**, 40-51 (1960).
57. Norton, D. R. & Keller, A. The spherulitic and lamellar morphology of melt-crystallized isotactic polypropylene. *Polymer* **26**, 704-716 (1985).
58. Olley, R. H. & Bassett, D. C. On the development of polypropylene spherulites. *Polymer* **30**, 399-409 (1989).
59. Janimak, J. J., Cheng, S. Z. D., Giusti, P. A. & Hsieh, E. T. Isotacticity effect on crystallization and melting in poly(propylene) fractions: 2. Linear crystal growth rate and morphology study. *Macromolecules* **24**, 2253-2260 (1991).
60. Yamada, K., Matsumoto, S., Tagashira, K. & Hikosaka, M. Isotacticity dependence of spherulitic morphology of isotactic polypropylene. *Polymer* **39**, 5327-5333 (1998).
61. Geil, P. H. *Polymer single crystals*, 1-560 (Willey-Interscience, New York, 1963).
62. Strobl, G. *The Physics of Polymer: Concepts for Understanding Their Structures and Behavior 2nd edition* 1-439 (Springer-Verlag, Berlin, 1997).
63. Awaya, Y. Koubunshisozai no henkoukenbikyou nyuumon (Introduction to polarized optical microscope for polymer materials), 1-264 (Agne gijyutsu center, Tokyo, 2001).

Chapter 2
In-situ Observations of Mesophase Formation of Isotactic Polypropylene
–Fast Time-resolved X-ray Diffraction Study–

2.1. Introduction

As mentioned in Chapter 1, the mesophase iPP is obtained by quenching molten amorphous iPP; empirically, this is achieved by dropping a thin piece of a sample rapidly into ice water. During quenching the sample, the sample experiences a cooling rate of the order of 100 °C/s. Specifically, the formation speed of the mesophase iPP is particularly high, and the formation process is completed over a short period of time. Then, extensive ex-situ analysis of the transformation process to the mesophase of iPP has been performed [1-7]. However, in-situ measurements of the formation process have been hardly done because it was impossible so far to follow such fast phenomenon. Recently, initial in-situ observations were performed by a fast differential scanning calorimetric (fast DSC) technique [8], and an exothermal shoulder peak due to the mesophase formation was observed. In subsequent studies, an ultra-fast DSC technique successfully resolved two exothermal peaks due to crystallization and the mesophase formation [9]. The understanding of the formation process of the mesophase iPP has progressed significantly as a result of thermal analysis.

From a structural point of view, the first in-situ observations of mesophase iPP formation were accomplished by heating from the glassy amorphous state [7, 10]. Most recently, by using a propene/ethylene copolymer [11] to effectively delay the formation rate of the mesophase, in-situ observation of the formation process of the mesophase from the molten state has been achieved [12]. Thus, in-situ observation of the formation process of mesophase iPP has been challenging.

In this chapter, we have performed in-situ observations of the formation process of mesophase of isotactic polypropylene (iPP) homopolymer by quenching the molten amorphous iPP to various temperatures using wide-angle X-ray diffraction (WAXD)

technique. As mentioned in Chapter 1, the formation process of the mesophase of iPP is so rapid that very fast observation technique is essential for the measurements. For this purpose, fast time-resolved WAXD measurements have been accomplished by combining a high-flux synchrotron radiation X-ray scattering facility and a rapid temperature-jump technique.

2.2. Experimental Procedure

2.2.1. Materials and Sample Preparations

The iPP material was supplied from Idemitsu Unitech Co., Ltd; the weight-average molecular weight is M_w = 380000 with a polydispersity of M_w/M_n = 4.5, and a degree of isotacticity (a meso pentad value) *mmmm* = 0.93. This isotacticity is higher enough than the critical value (0.68) of isotacticity to form the mesophase [5]. The sample film was prepared by quenching the molten iPP to 0 °C dipping into ice water. For WAXD measurements, the sample film having thickness of 200 μm was sandwiched between aluminum foils with 10 μm thickness.

2.2.2. Temperature Jump Stage

We have developed a temperature jump type hot stage consisting of two thermally separated heat blocks [13]. The temperature of each heat block was regulated independently. The sample cells consisted of a spacer rim and a pair of window materials such as aluminum foils for X-ray measurements or glass for optical measurements. Sample cells containing thin films were transferred immediately from one block to the other by passing through flat gaps and arranged colinearly inside the blocks. The thickness of the gap was adjusted to maintain a good thermal contact between the heat block and the sample cell. The heat capacity of the block was designed to be much larger than that of the sample cell so that the sample would approximately experience a relaxationtype temperature variation $T(t)$ with time t as

$$T(t) = (T_1 - T_2) \exp(-t/\tau_{cooling}) + T_2 \qquad (2.2.1)$$

where T_1, T_2 and $\tau_{cooling}$ are the temperatures of the first and second heat blocks and the characteristic time of cooling, respectively. $T(t)$ was monitored by a thin thermocouple attached to the sample cell. Figure 2.1 shows a typical cooling curve monitored for a case

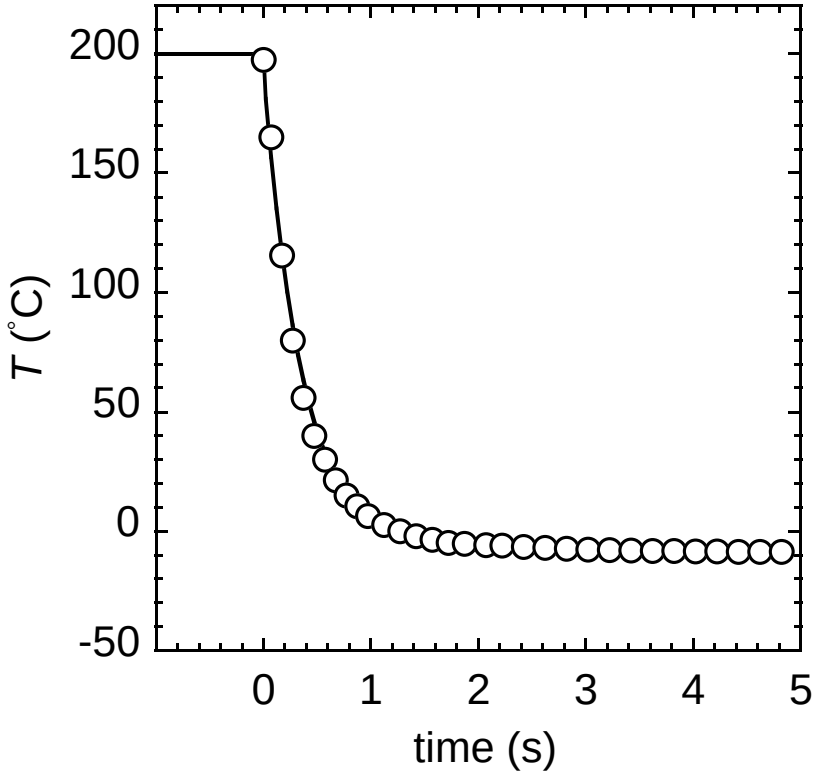

Figure 2.1. typical cooling curve monitored for a case T_1 = 200 °C and T_2 = –10 °C using aluminum foils 10 μm thick as the sample cell (see text).

where T_1 = 200 °C and T_2 = –10 °C using 10 μm thick aluminum foil with the sample cell. This case corresponds to the condition for time-resolved WAXD measurements as is described below (Figure 2.2 (a)). The open circles represent the observed values, and the solid line is a curve that was fit according to equation (2.2.1), where tcooling.0.36 s gives the best fit. The accuracy of $\tau_{cooling}$ may be affected by the conditions in the sample cell, so the cooling curve was calibrated for each case using the actual measurements of $T(t)$. A commercially available version of this apparatus is available from Japan Hightech and Linkam as LK-300. Further description of the apparatus is available elsewhere [13].

2.2.3. Wide-angle X-ray Diffraction (WAXD) Measurements

Fast time-resolved WAXD measurements were conducted using a high intensity undulator X-ray beam line BL45XU [14] in a synchrotron radiation (SR) facility, SPring-8, Hyogo, Japan. In the present measurements, the wavelength of the incident X-ray λ was selected to 0.9 Å by using a double crystal monochromator made of a set of synthetic diamond, so as to facilitate a good transmission for the sample. The scattering vector q (= $4\pi \sin\theta/\lambda$) was covered from 8 to 18 nm^{-1} for the WAXD measurements, where θ is a half of the scattering angle (2θ). The scattered X-ray was detected by an image intensified CCD camera (IICCD) with a capturing frequency 25 Hz at 0.04 s intervals in the fastest case. After standard data processing, such as correction of detector sensitivity and subtraction of scattering from the empty sample cell, the WAXD data were circularly averaged, since the 2-dimensional data showed no anisotropy.

2.2.4. Optical Microscope Observations

Time evolution of the optical micrographs was recorded with a Nikon Optiphot2-Pol with a CCD camera and a video recorder. The bright field mode of optical microscopy was used although the polarized light mode is often used for the observation of polymer crystallization, since the mesophase iPP give only very weak optical retardation. The

capturing frequency was 30 Hz according to the (National Television System Committee) NTSC format.

2.3. Results and Discussion

2.3.1. Time-resolved Wide-angle X-ray Diffraction (WAXD)

Fast time-resolved WAXD measurements were carried out while the molten iPP was rapidly cooled to various destined temperatures T_2. Figures 2.2 (a) to (d) show typical examples of the time-evolution of WAXD profiles at T_2 = –10, 20, 40 and 80 °C, respectively. For all the T_2s, the WAXD profile initially shows a single broad peak at around q = 11 nm^{-1}, which is characteristic of the molten amorphous state. The subsequent development depends on T_2. At T_2 = –10 °C (Figure 2.2 (a)), monotonic development of the second broad peak at around q = 15 nm^{-1}, characteristic of the mesophase iPP, is observed in common with the case by heating from the glassy amorphous state [11]. The resulting sample showed a broad SAXS peak at around q = 0.6 nm^{-1} by a preliminary measurement, which is considered due to the nodular structure. The value corresponds to 10 nm in real space. This is also a characteristic of the mesophase iPP as was mentioned in the introduction [7, 10, 15, 16]. Such detailed SAXS studies will be reported elsewhere. Inferring from the monotonic development it can be considered that there does not exist any other intermediate state between the amorphous and the mesophase at least in crystallographic scale. Qualitatively, the mesophase iPP fades away with increasing T_2 while the α-crystal becomes obvious.

To make this behavior more quantitative, these WAXD profiles were separated into three components of α-crystal, mesophase, and amorphous, according to the previously reported method [5].Figures 2.3 (a) to (d) show examples of the component analyses for the final WAXD profiles at T_2 = –10, 20, 40 and 80 °C, which were shown in Figure 2.2 (a) to (d), respectively. Open circles, thin solid lines, thin dotted lines and thick dotted lines represent observed WAXD profiles, crystalline, mesophase and amorphous components, respectively. Here the crystalline and mesophase components are described by the assembly of Lorenz curves.

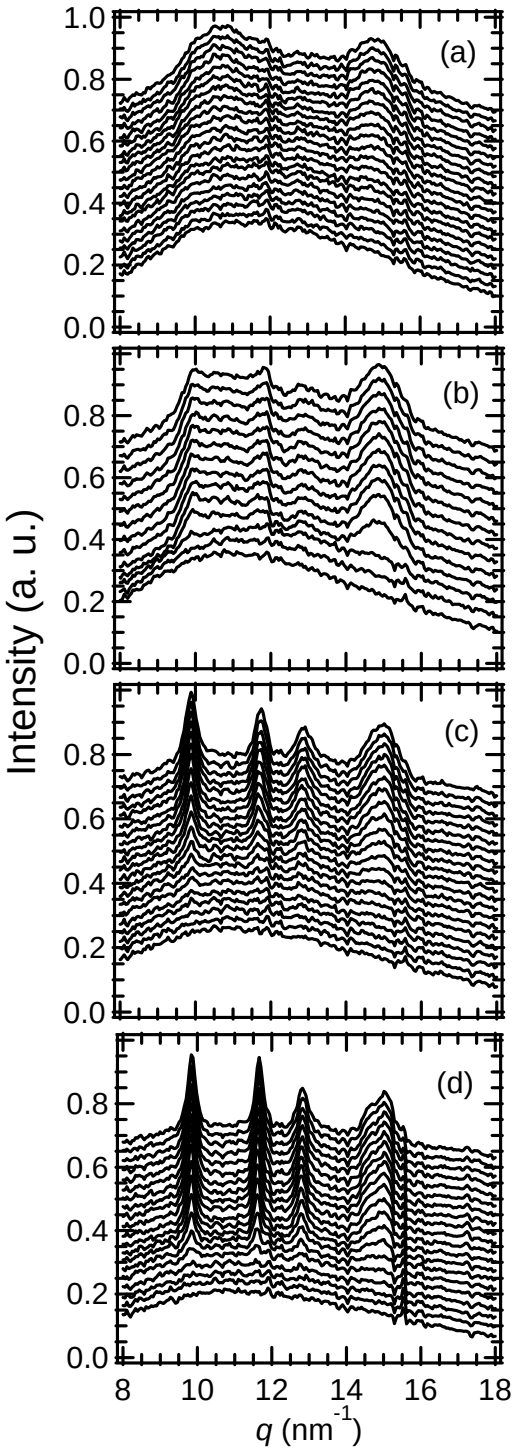

Figure 2.2. Time evolutions of WAXD profiles during molten iPP is rapidly cooled to the destined temperatures T_2. (a): T_2 = –10 °C, profiles are shown in every 0.04 s from t = 0.2 s to 1.0 s. (b): T_2 = 20 °C, profiles are shown in every 0.4 s from t = 0 s to 5.2 s. (c): T_2 = 40 °C, profiles are shown in every 0.08 s from t = 0.2 s to 1.8 s. (d): T_2 = 80 °C, profiles are shown in every 0.16 s from t = 0.2 s to 3.4 s.

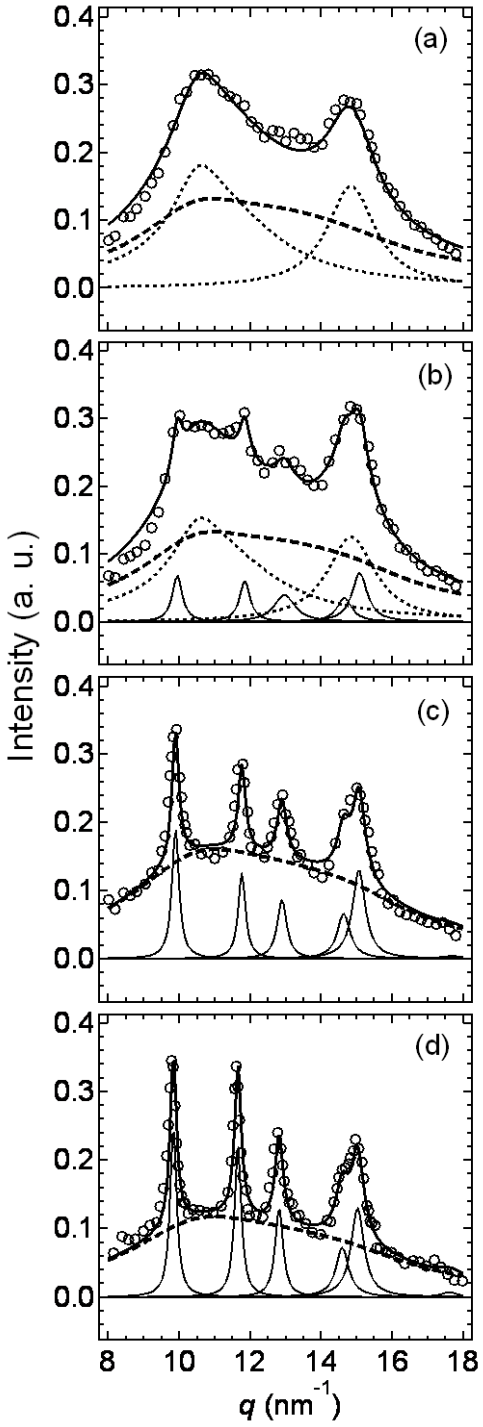

Figure 2.3. Examples of component analyses. Parts (a), (b), (c) and (d) correspond the final WAXD profiles at T_2 = –10, 20, 40 and 80 °C, which were shown in Figure 2.2 (a), (b), (c) and (d), respectively. Open circles, thin solid lines, thin dotted lines and thick dotted lines represent observed WAXD profiles, crystalline, mesophase and amorphous components, respectively. Thick solid lines represent the fitting curves.

A smoothed curve of the WAXD profile for the molten state is used as a reference curve for the amorphous component. Thick solid lines, which are the summations of the crystalline, mesophase and amorphous components, reproduce the observed WAXD profiles fairly well. The fractions Φ_{cryst}, Φ_{meso} and Φ_{amorph} of α-crystal, mesophase and amorphous components, respectively, were obtained as the ratios of the integrated intensity of each component to the total integrated intensity. Figure 2.4 shows such fractions as a function of time t during rapid cooling process. The conditions in Figures 2.4 (a) to (d) correspond to those in Figures 2.2 (a) to (d), respectively. For T_2 = –10 °C (Figure 2.4 (a)), Φ_{meso} starts to increase at around t = 0.5 s and levels off at around t = 2.0 s. In this way, the mesophase formation finishes in a very short time. The time t = 0.6 s corresponds to the temperature T = ca. 30 °C in Figure 2.1. This temperature is considered to be around the onset temperature where the mesophase formation is favorable. During the cooling process, only the development of Φ_{meso} is observed and Φ_{cryst} is not detected. At T_2 = 20 °C (Figure 2.4 (b)), development of Φ_{meso} is still predominant, but Φ_{cryst} develops somewhat. At $T_2 \geq 40$ °C (Figures 2.4 (c) and (d)), development of Φ_{meso} is no more detected and instead development of Φ_{cryst} becomes predominant.

2.3.2. Fractions of Crystal and Mesophase at the Final Stage of Cooling

Figure 2.4 shows the fractions of α-crystal Φ_{cryst} and mesophase Φ_{meso} at the end of cooling as a function of the destined temperature T_2. Φ_{cryst} starts to increase gradually with temperature and rather steeply increases between 30 and 50 °C. Meanwhile, Φ_{meso} decreases gradually below 30 °C and drastically between 30 and 40 °C, and above 40 °C it is not detected. Taking these results and also the previously described time-resolved WAXD data (Figure 2.4 (a)) into consideration, we can conclude that the temperature range being favorable for the mesophase formation is located below 35 ± 5 °C. This upper crossover temperature obtained by the present analysis is well consistent with the value obtained by the ultra-fast DSC [9].

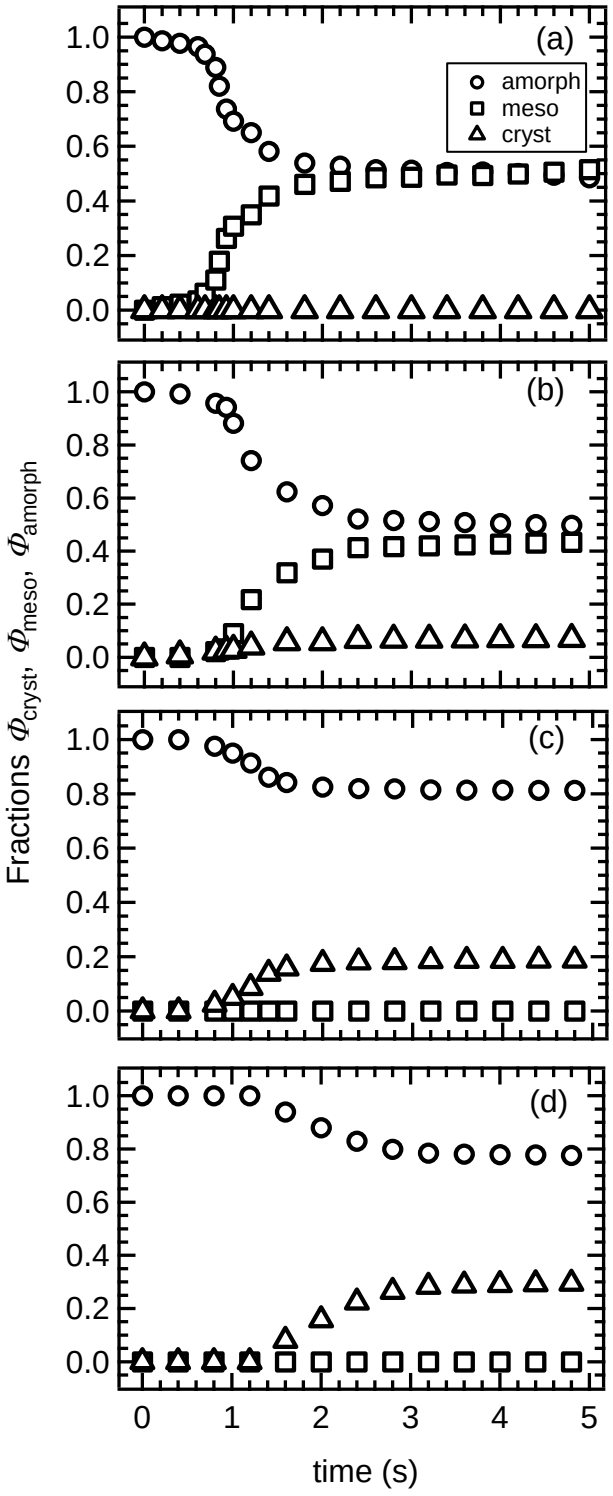

Figure 2.4. Fractions of α-crystal Φ_{cryst}, mesophase Φ_{meso} and amorphous Φ_{amorph} as a function of time t during rapid cooling process. The conditions in (a), (b), (c) and (d) correspond to those in Figure 2.2 (a), (b), (c) and (d), respectively.

2.3.3. Formation Rate of Mesophase Along a Specific Path

In the previous sections, the formation of the mesophase iPP has been surveyed in the structural viewpoint and the yield of the mesophase as a function of quenching temperature or the destined temperature T_2, has been obtained as in Figure 2.5. In the present section, we would like to discuss the kinetics of formation of the mesophase iPP. In general, the transition rate is estimated under the isothermal or the constant cooling rate conditions.

However, the cooling carried out in this experiment was considerably rapid as shown in Figure 2.1, so that neither the ideal isothermal nor the constant cooling rate condition is fulfilled. In such a nonideal condition, it is difficult to determine the proper formation rate of the mesophase. Alternatively we employed an amount defined by a differential fraction of the mesophase and temperature change, which is the increment of mesophase fraction by temperature decrement, $\mathrm{d}\Phi_{\mathrm{meso}}/(-\mathrm{d}T)$. This value qualitatively corresponds to a formation rate of the mesophase at each temperature. Such an apparent formation rate is obtained as follows. Referring $T(t)$ curve (Figure 2.2), $\Phi_{\mathrm{meso}}(t)$ (Figure 2.4 (a)) is converted into $\Phi_{\mathrm{meso}}(T)$, then $\mathrm{d}\Phi_{\mathrm{meso}}/(-\mathrm{d}T)$ is obtained by differentiating $\Phi_{\mathrm{meso}}(T)$ by T. The results are shown as a function of T. The resulting curve $-\mathrm{d}\Phi_{\mathrm{meso}}/\mathrm{d}T$ shows a monomodal distribution function. Above 40 °C it shows no significant value. With decreasing the temperature, it increases gradually and shows a maximum at around 10 °C. Then it starts to decrease below 10 °C and tends to converge into zero at around –10 °C. In preparation for the next section, we should remember that the present formation rate of mesophase of iPP was obtained along a “specific” thermal path.

2.3.4. Suitable Kinetic Path for Mesophase Formation

It is often considered that a rapid quenching is essential in order to obtain the mesophase iPP without developing a crystal fraction, while too rapid quenching to a deep supercooled state vitrifies the molten iPP without forming the mesophase, as was demonstrated by an ultraquenching technique [10, 11]. With this in mind, we wanted to determine the suitable cooling rates and suitable quenching temperatures. As was mentioned previously, a cooling rate of 100 °C/s has been a standard, but this is an estimate and is unspecific. The suitable

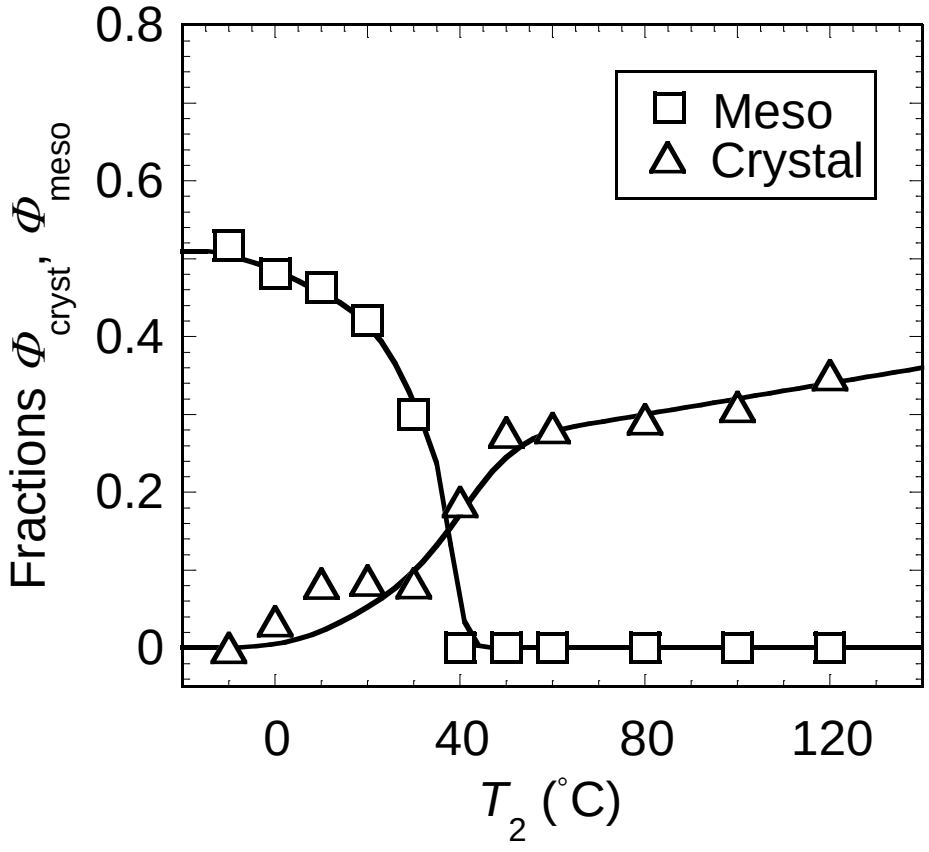

Figure 2.5. Final fractions of α-crystal Φ_{cryst} and mesophase Φ_{meso} phases at the end of cooling as a function of the destined temperature T_2.

kinetic paths for mesophase formation should be considered more specifically. The results of the ultra-fast DSC work were obtained with constant cooling rates (Figure 2 in Gradys *et al*. [9]). When the cooling rate was < 3000 °C/min (50 °C/s), almost all of the heat flow was due to crystallization. In increasing the cooling rate to > 3000 °C/min, the heat flow was due to the increase in mesophase formation, and the heat flow due to crystallization gradually decreased. The heat flow due to mesophase formation was at a maximum of 9000 °C/min (150 °C/s); however, at this cooling rate, crystallization still contributed significantly, and a bimodal distribution in the heat flow was observed at ~ 60 and 15 °C for the crystal and mesophase, respectively. A suitable cooling rate for the mesophase formation could not effectively suppress crystallization. Faster cooling rates, exceeding 9000 °C/min, suppressed both crystallization and mesophase formation considerably. The cooling rate that gives the fastest rate of mesophase formation does not correspond to the cooling rate that gives the slowest rate for crystallization. The mesophase iPP, not including the crystal fraction, can be obtained by the empirical quenching method, that is, by dropping the sample into ice water. With empirical quenching, the initial cooling rate is very large, and the rate decreases progressively with time. With such a cooling trajectory, the cooling rate is not only large enough to suppress crystallization in the temperature range 80-90 °C, where the rate of crystallization is at a maximum [17, 18], but is also able to cause mesophase formation in the temperature range 10-30 °C, where its formation rate is at a maximum [17]. Thus, the empirical quenching method inadvertently allowed for the realization of a suitable kinetic pathway for mesophase formation. It is believed that the ideal path to obtain mesophase iPP at the maximum rate should be with isothermal annealing at ~ 10-30 °C, with a subsequent quenching at an infinitely large cooling rate.

2.3.5. Mechanism of Mesophase Formation

The term ‘homogeneous’ is often interpreted by two ways in the relevant field. One is used to express the homogeneity of material, and the other is the homogeneity in space. To clarify, we define the former and the latter ‘materially homogeneous’ and ‘spatially

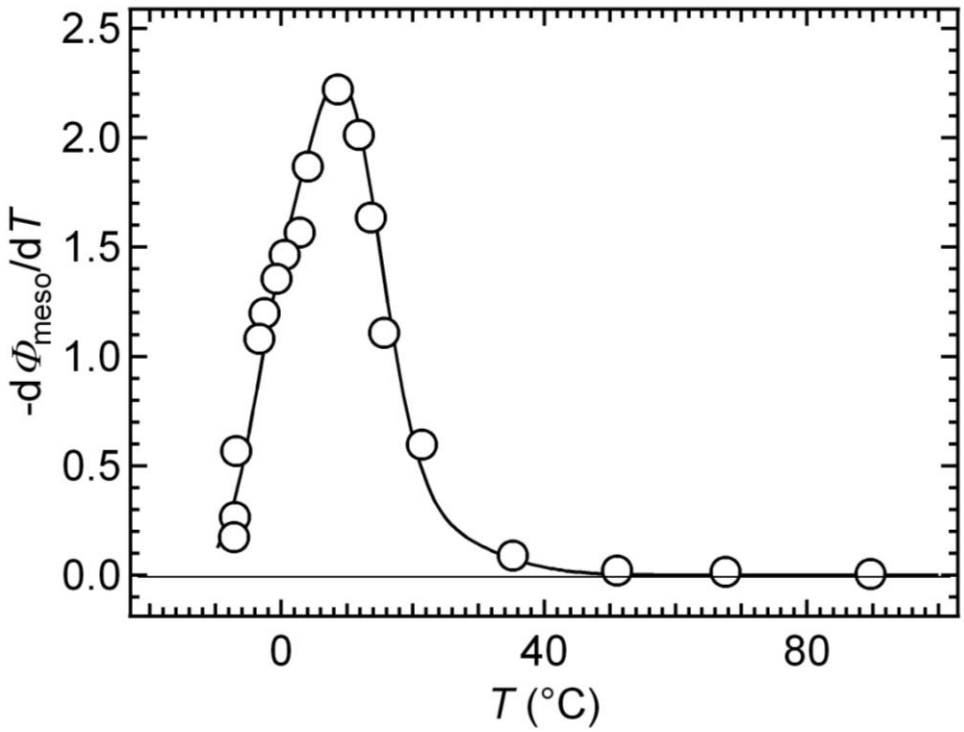

Figure 2.6. The differential fraction of the mesophase of iPP and temperature change, $-\mathrm{d}\Phi_{meso}/\mathrm{d}T$, as a function of temperature T along a specific thermal path as shown in Figure 2.2. This value represents the increment of mesophase fraction by temperature decrement, $\mathrm{d}\Phi_{meso}/(-\mathrm{d}T)$ and qualitatively corresponds to a formation rate of the mesophase at each temperature.

homogeneous', respectively. On the basis of a theory by Olmsted *et al*. [18], we propose a general model for the crystallization mechanism (for example, see Figure 31 in Kaji *et al*. [19]). The mechanism is categorized into three regions according to the supercooling depth, ΔT, from the melting temperature, T_m. In order from small to large ΔT, these regions are a direct crystal nucleation, binodal crystallization and spinodal crystallization. The first region is where the melt and crystals coexist in the phase diagram of the polymer melt by Olmsted, where crystal nucleation occurs directly from the melt, and classical crystal nucleation theory [20] seems to only be valid here. The other two regions involve phase separation between oriented (nematic) and unoriented (isotropic) phases before crystallization. In the binodal crystallization region, spherical nuclei or droplets of nematic phase are first formed in the isotropic melt and grow with time, and thereafter, crystallization is initiated inside the droplets through a smectic phase. Such a bimodal or nucleation and growth (N&G) type of phase separation occurs in the metastable region of the phase diagram. In the spinodal crystallization region, a spinodal decomposition (SD) type of phase separation first occurs between the nematic and isotropic phases with a quasi periodicity when the system falls into the unstable state of the phase diagram, and then crystallization occurs in the nematic phase part through the smectic phase. Such a smectic phase appearing midway before crystallization corresponds to the mesophase. Although the order parameter is different, this phase separation is similar to that of polymer blends. The usual spherulites are produced from the N&G region and not from the direct crystal nucleation region where single crystals seem to form directly from the melt at extremely slow rates. In the N&G regime, spherical nuclei or droplets are produced sporadically in time and randomly in space as well as grow in size with time. Accordingly, the resulting morphology shows a spatially inhomogeneous structure consisting of randomly arranged spherical domains or polygonal domains in the final stage. As described above, the internal structure of these spherical entities or droplets in the initial stage is regarded as a nematic liquid crystal where the molecules may be oriented perpendicular to the radius of each sphere. This scheme may provide evidence for explaining the formation process of the internal structure of the spherulite (see Imai *et al*. [21]). Furthermore, in real

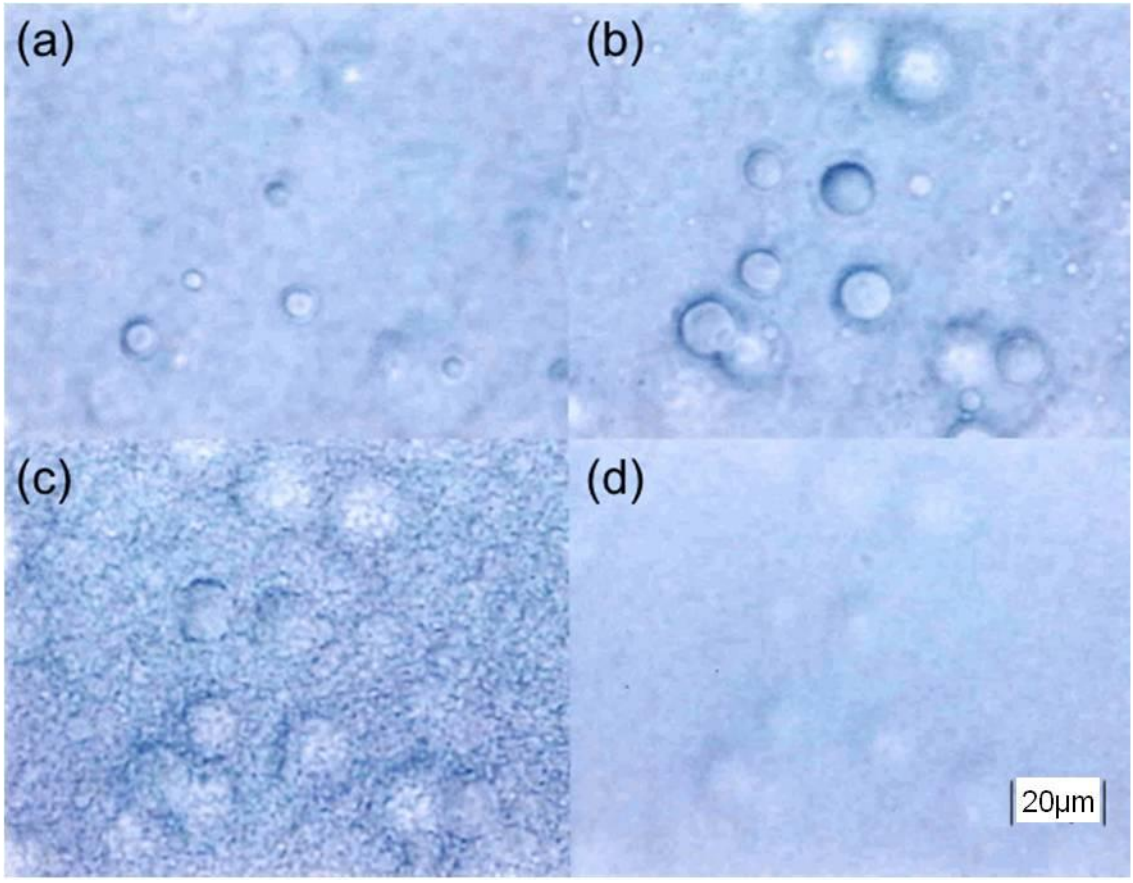

Figure 2.7. Time evolutions of optical micrographs immediately after molten iPP was rapidly cooled to the destined temperature T_2 = 10 °C. (a): t = 0.25 s (T = ca. 125 °C), (b): t = 0.5 s (T = ca. 70 °C), (c): t = 0.75 s (T = ca. 35 °C), (d): t = 1.0 s (T = ca. 25 °C).

systems, the nucleation of the nematic droplets, not the crystal nucleation, would be accelerated by impurities because nucleation assisted by impurities goes through a lower free-energy path, and the heterogeneous nucleation of droplets can occur at a smaller supercooling temperature [22]. When the isotropic melt falls into the SD region, it becomes unstable; therefore, the fluctuations due to molecular orientation appear instantaneously all over the system, accompanied by a characteristic wavelength. Accordingly, the resulting morphology is likely to form a quasi-periodic structure that is spatially homogeneous on a larger scale than the characteristic wavelength. Moreover, because the driving force of the SD is very large, owing to the unstable transition at a deep supercooling, both the SD process and the crystallization that follows will not be affected by impurities. Therefore, the crystallization in the unstable state seems to occur by the materially homogeneous nucleation, even in the presence of impurities. Figure 2.7 shows a series of optical micrographs of iPP during a rapid cooling process at T_2 = 10 °C. Figures 2.7 (a) to (d) are micrographs of 0.25, 0.5, 0.75 and 1.0 s after quenching, corresponding to 125, 70, 35 and 25 °C, respectively. In Figures 2.7 (a) and (b), growing spherical domains or droplets with different diameters are observed. Specifically, they should have been generated sporadically in time and randomly in space. On the other hand, as can be seen in Figure 2.7 (c), instantaneous fluctuations all over the system are observed. A Fourier transformation of the image in Figure 2.7 (c) gives a broad shoulder at ~ 3 μm^{-1} in reciprocal space, corresponding to ca. 2 mm in real space. This result indicates that there exists a weak periodicity in the system. We believe this periodicity is due to the SD structure. Thus, the randomly arranged spherical domain structure and the periodic structure show the characteristics of the binodal (N&G) and SD phase separation, respectively. Both of these phase-separated, ordered regions initially assume an internal structure of a nematic phase and then convert to a smectic phase or mesophase, from which crystallization is initiated. The transformation from nematic to smectic should involve a secondary phase separation to exclude molecular entanglements in the nematic phase, which produces very small order particles or so-called nodules and amorphous regions including entanglements. This process proceeds relatively quickly, but crystallization from the smectic phase takes

some time depending on the temperature and may be one reason why the mesophase is relatively stable. Another possible reason could be an increase in the glass transition temperature [11] with increasing mesophase fraction, which may freeze the crystallization process incompletely at the mesophase. Meanwhile, in the N&G region, which is more favorable for crystallization in iPP, the mesophase exists only transiently at the beginning of crystallization [23] and is therefore barely detectable by WAXD (Figures 2.2 (c) and (d)). We have made progress in understanding the mechanism by which the mesophase of iPP forms. Further studies will be required to fully elucidate this mechanism.

References

1. Piccarolo, S., Saiu, M., Brucato, V. & Titomanlio, G. Crystallization of polymer melts under fast cooling. II. High-purity iPP. *J. Appl. Polym. Sci.* **46**, 625-634 (1992).
2. Choi, C.-H. & White, J. L. Correlation and modeling of the occurrence of different crystalline forms of isotactic polypropylene as a function of cooling rate and uniaxial stress in thin and thick parts. *Polym. Eng. Sci.* **40**, 645-655 (2000).
3. Brucato, V., Piccarolo, S. & Carrubba, V. L. An experimental methodology to study polymer crystallization under processing conditions. The influence of high cooling rates. *Chem. Eng.Sci.* **57** 4129-4143 (2002).
4. Coccorullo, I. Pantani, R. & Titomanlio, G. Crystallization kinetics and solidified structure in iPP under high cooling rates. *Polymer* **44**, 307–318 (2003).
5. Konishi, T., Nishida, K., Kanaya, T. & Kaji, K. Effect of isotacticity on formation of mesomorphic phase of isotactic polypropylene. *Macromolecules* **38**, 8749-8754 (2005).
6. Li, L. & de Jeu, W. H. Shear-induced smectic ordering and crystallisation of isotactic polypropylene. *Faraday Discuss*. **128**, 299–319 (2005).
7. Zia, Q., Androsch, R., Radusch, H.-J. & Piccarolo, S. Morphology, reorganization and stability of mesomorphic nanocrystals in isotactic polypropylene. *Polymer* **47**, 8163-8172 (2006).
8. Wu, Z. Q., Dann, V. L., Cheng, S. Z. D. & Wunderlich, B. Fast DSC applied to the crystallization of polypropylene. *J. Therm. Anal.* **34**, 105-114 (1988).
9. Gradys, A., Sajkewicz, P., Minakov, A. A., Adamovsky, S., Schick, C., Hashimoto, T. & Saijo, K. Crystallization of polypropylene at various cooling rates. *Mater. Sci. Eng. A* **413-414**, 442-446 (2005).
10. Hsu, C. C., Geil, P. H., Miyaji, H. & Asai, K. Structure and properties of polypropylene crystallized from the glassy state. *J. Polym. Sci., Part B: Polym. Phys.* **24**, 2379-2401 (1986).
11. Miyamoto, Y., Fukao, K., Yoshida, T., Tsurutani, N. & Miyaji, H. Structure formation of isotactic polypropylene from the glass. *J. Phys. Soc. Jpn.* **69**, 1735-1740 (2000**)**.

12. Cavallo, D., Portale, G., Balzano, L., Azzurri, F., Bras, W., Peters, G. W. & Alfonso, G. C. Real-time WAXD detection of mesophase development during quenching of propene/ethylene copolymers. *Macromolecules* **43**, 10208-10212 (2010).
13. Nishida, K. Rapid temperature jump stage for optical microscope. *Proc. Polymer Processing Soc.* S17–631 (2008).
14. Fujisawa, T., Inoue, K., Oka, T., Iwamoto, H., Uruga, T., Kumasaka, T., Inoko, Y., Yagi, N. Yamamoto, M. & Ueki, T. Small-angle X-ray scattering station at the SPring-8 RIKEN beamline. *J. Appl. Cryst.* **33**, 797-800 (2000).
15. Ogawa, T., Miyaji, H. & Asai, K. Nodular structure of polypropylene. *J. Phys. Soc., Jpn.* **54**, 3668-3670 (1985).
16. Zia, Q., Radusch, H.-J. & Androsch, R. Direct analysis of annealing of nodular crystals in isotactic polypropylene by atomic force microscopy, and its correlation with calorimetric data *Polymer* **48**, 3504-3511 (2007).
17. Silvestre, C., Cimmino, S., Duraccio, D. & Schick, C. Isothermal crystallization of isotactic poly(propylene) studied by superfast calorimetry. *Macromol. Rapid Commun.* **28**, 875–881 (2007).
18. Olmsted, P. D., Poon, W. C. K., McLeish, T. C. B., Terrill, N. J. & Ryan, A. J. Spinodal-assisted crystallization in polymer melts. *Phys. Rev. Lett.* **81**, 373-376 (1998).
19. Kaji, K., Nishida, K., Kanaya, T., Matsuba, G., Konishi, T. & Imai, M. Spinodal crystallization of polymers: crystallization from the unstable melt. *Adv. Polym. Sci.* **191**, 187-240 (2005).
20. Turnbull, D. & Fisher, J. C. Rate of nucleation in condensed systems. *J. Chem. Phys.* **17**, 71-73 (1949).
21. Imai, M. & Kaji, K. Polymer crystallization from the metastale melt: the formation mechanism of spherulites. *Polymer* **47**, 5544-5554 (2006).
22. Janeschitz-Kriegl, H. Conditions of nucleation in crystallizable polymers: reconnaissance of positions - a critical evaluation. *Colloid. Polym. Sci.* **275**, 1121-1135 (1997).
23. Strobl, G. From the melt via mesomorphic and granular crystalline layers to lamellar

crystallites: A major route followed in polymer crystallization? *Eur. Phys. J. E* **3**, 165-183 (2000).

Chapter 3
Energy Levels of Mesophase of Isotactic Polypropylene

3.1. Introduction

The mesophase of iPP is considered a meta-stable state whose energy level is very low comparable to that of crystal. Differential scanning calorimetry (DSC) is usually a versatile method to examine various transitions among states in polymer and other materials. However, this method is rather insensitive to the transition of iPP from mesophase to crystal, since the majority of the exotherm was completed during the formation of the mesophase and the remaining exothermic enthalpy is considered to be small as was mentioned in the preceding paragraph. To make the matter more complex, other transitions such as mesophase to amorphous and/or amorphous to crystal may co-occur during heating, whose enthalpy are larger than that of the mesophase to crystal. Alternatively, the transition should be investigated in structural point of view. In this respect, wide-angle X-ray diffraction (WAXD) measurement is a sensitive method to detect the structural change whether or not the transition is accompanied by exo- or endotherm. Recent developments of high-intensity synchrotron radiation (SR) source and sensitive time-resolved detector system enable in-situ WAXD measurements in the similar thermal trace of DSC measurement. In this study, such a SR-WAXD technique has been applied to investigate crystallization of iPP from mesophase. Fractions of α-crystal, mesophase and amorphous phase as a function of temperature have been obtained by a component analysis of WAXD profile. The derivative of the crystalline fraction as a function of temperature clearly shows crystallization behavior of iPP from mesophase, which backs up the above-mentioned disadvantage of DSC method. Combining the structural information by SR-WAXD and DSC measurements, the energy level of mesophase has been estimated. Although rough estimation of the energy level of mesophase is possible by assuming the original fraction of mesophase transforms into the same fraction of α-crystal [1, 2], in reality the balance among the fractions of α-crystal, mesophase and amorphous phase as a function of temperature should be taken into consideration for the more

precise estimation.

3.2. Experimental

3.2.1. Materials and Sample Preparations

The iPP material has a weight-average molecular weight M_w = 353000, a polydispersity of M_w/M_n = 4.4, and a degree of isotacticity (a meso pentad value) *mmmm* = 0.98, which was supplied from Idemitsu Unitech Co., Ltd. This isotacticity is higher enough than the critical value (0.68) of isotacticity to form mesophase [3]. A mesophase thin film was obtained by quenching molten iPP to 0 °C by dipping into ice-water. The obtained film was macroscopically transparent and showed two broad peaks in WAXD, which are the characteristics of mesophase iPP.

3.2.2. Measurements

DSC measurements were carried out with a Perkin-Elmer Diamond DSC at a heating rate of 10 °C/min. WAXD measurements were carried out using the beam line BL40B2 in the SR facility, SPring-8, Hyogo, Japan. Wavelength of the incident X-ray was 1.0 Å. The detector used was CMOS flat panel detector from Hamamatsu Photonics K.K. The exposure time was selected to be 0.5 s. A Mettler FP82HT hot stage was used to heat the specimens for WAXD measurements at the same heating rate of the DSC measurement. In both DSC and WAXD measurements, thin films were tightly piled up to the same sample thickness, 0.7 mm, to apply similar thermal conduction within the samples.

3.3. Results and Discussion

3.3.1. Differential Scanning Calorimetry (DSC)

Figure 3.1 shows a DSC curve for a mesophase iPP during a heating process. The curve shows a shoulder at around 40-50 °C. We assume this shoulder is due to a glass transition like phenomenon of the mesophase of iPP, though there still is discussion for the origin [4]. An exothermal shallow peak is observed at around 100 °C. As will be turned out in the WAXD

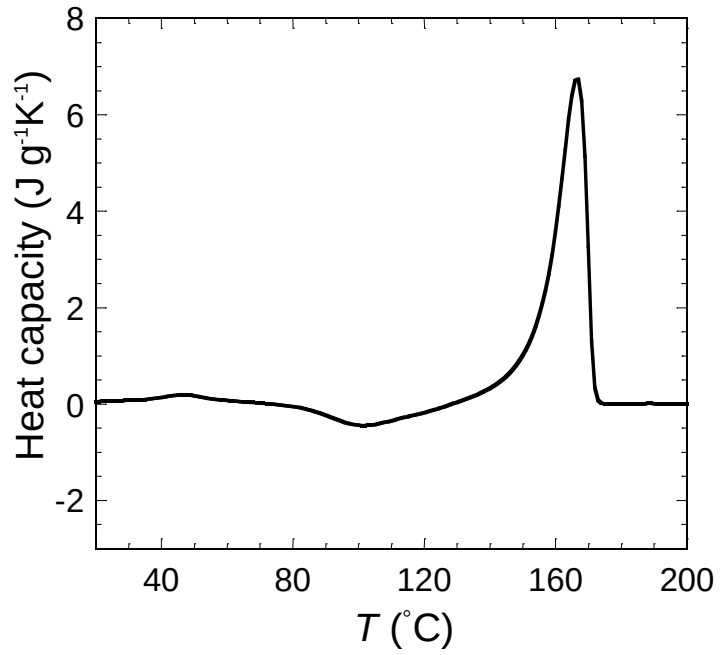

Figure 3.1. Observed DSC curve for mesophase iPP during heating process.

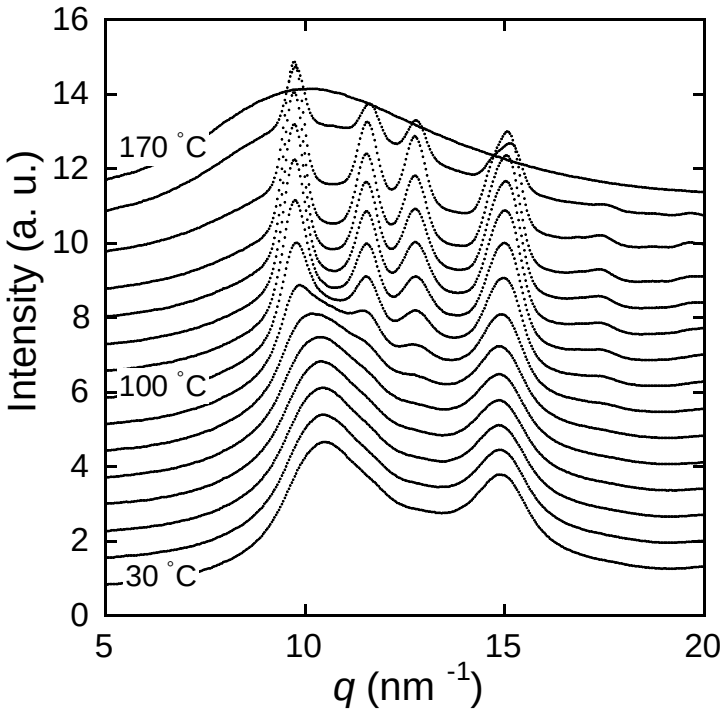

Figure 3.2. WAXD profiles during heating process from 30 to 170 °C displayed at every 10 °C from bottom to top. The profiles were shifted vertically for clarification.

analysis, this exothermal shallow peak is due to the crystallization from the mesophase. Endotherm starts at around 130 °C and a distinct endothermic peak is observed at around 165 °C. It is unquestionable to assign the distinct endothermic peak to the melting of the crystal. Integrated areas of these exo- and endothermic peaks do not balance out. This is mainly because that the exothermic enthalpy when the mesophase transforms into crystal is small, as was mentioned in the introduction. However, it lacks proof to claim these explanations only with the DSC data. This will be discussed in the following section.

3.2.2. Wide-angle X-ray Diffraction (WAXD)

Figure 3.2 shows in-situ WAXD profiles during a heating process from 30 to 170 °C. Broad peaks appearing at scattering vectors around q = 10.5 and 14.9 nm^{-1} for the profiles of low temperatures are characteristics of the mesophase iPP. Sharp peaks appearing at q = 9.7, 11.5, 12.8 and 15.1 nm^{-1} for the profiles of temperatures between 90 and 160 °C are reflections from α-crystal. Single broad peak appearing at q = 10 nm^{-1} for the profiles at 170 °C is the so-called amorphous halo. In order to discuss the crystallization behavior quantitatively, component analysis for WAXD profiles was carried out assuming each profile consists of three components such as α-crystal, mesophase, and amorphous, according to the previously reported method [5]. Dividing the integrated intensity of each component by the integrated intensity of observed (total) intensity for each profile, fractions of α-crystal Φ_{cryst}, mesophase Φ_{meso} and amorphous Φ_{amorph} as a function of temperature during heating process were obtained, as shown in Figure 3.3. The crystallization from mesophase proceeds in between 60 and 120 °C (meso-α transition); this behavior is the most conspicuous at around 80 °C. During this process, the crystallization from amorphous hardly takes place. The crystalline fraction shows almost constant in between 120 and 140 °C. The maximum crystalline fraction (crystallinity) at this temperature is in disagreement with the original mesophase fraction at RT (Figure 3.3), at least in the present experimental condition. A possible reason for this disagreement is that the heating rate of 10 °C/min is not slow enough to let the mesophase transforms into crystal to the full extent. The crystalline fraction starts to

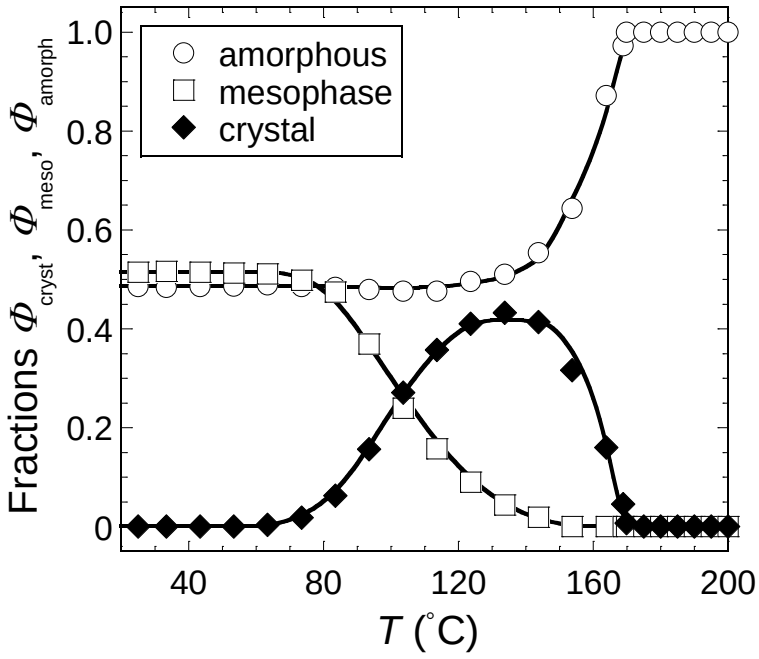

Figure 3.3. Fractions of α-crystal, mesophase and amorphous as a function of temperature during heating process.

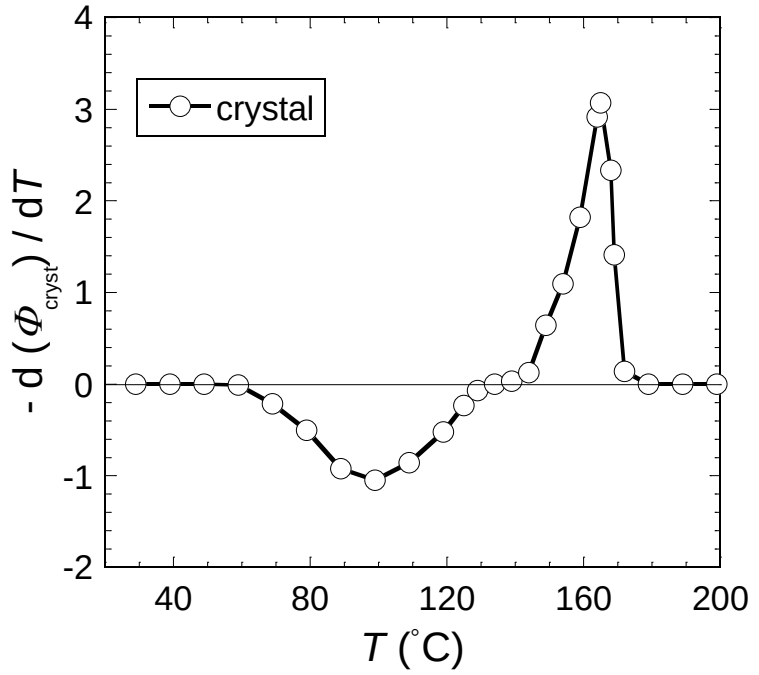

Figure 3.4. Temperature derivative of α-crystal fraction as a function of temperature.

decrease above 140 °C and the most extensively decreases at around 165 °C. Temperature derivative of α-crystal fraction $-d\Phi_{cryst}/dT$ more clearly shows crystallization behavior from mesophase (Figure 3.4). The integrated areas for the crystallization peak at around 100°C and that for the melting peak at around 165°C are equivalent in principle. With the support of these results, the shallow peak at around 100°C observed in DSC (Figure 3.1) has definitely turned out to be due to the crystallization.

3.3.3. Energy Level of Mesophase

Figure 3.5 shows schematic diagram of energy levels of α-crystal and mesophase relative to amorphous. Assuming the melting enthalpy of mesophase (ΔH_{meso}) being x times of that of α-crystal (ΔH_{cryst}), namely $\Delta H_{meso} = x\ \Delta H_{cryst}$, the total enthalpy relative to amorphous $\Delta H(T)$ is given by the following equation;

$$\Delta H(T) = \Delta H_{cryst}\Phi_{cryst}(T) + x\ \Delta H_{cryst}\Phi_{meso}(T). \quad (3.1)$$

Temperature derivative of $\Delta H(T)$ gives expected value of heat balance. As a reliable value of ΔH_{cryst} was already reported [6], unknown parameter is only x. Figure 3.6 shows $-d(\Delta H)/dT$ plotted for several values of x. The case when $x = 0.75$ reproduces the experimental DSC well. This value is significantly smaller than the previously reported values (=0.93 [1] and 0.97 [2]). It is essential to consider the balance among the fractions of α-crystal, mesophase and amorphous phase to obtain the reliable value, otherwise we end up overestimation of the value.

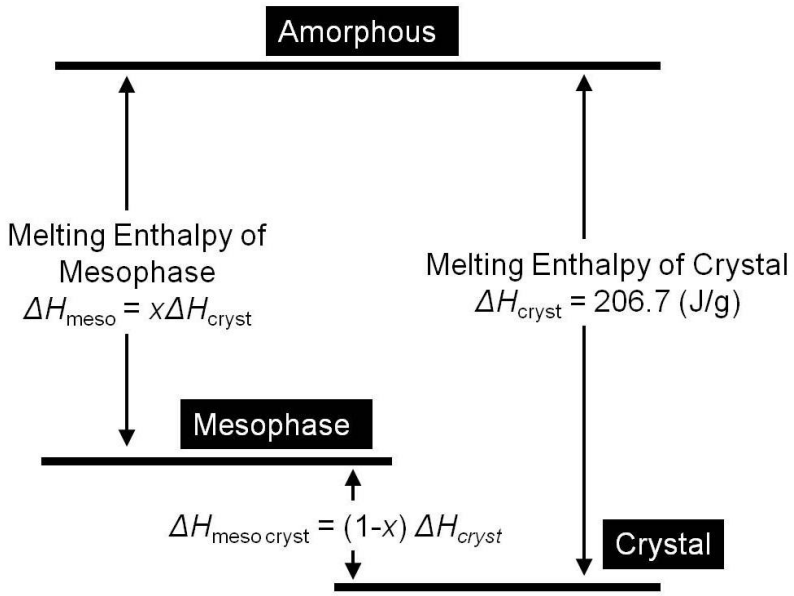

Figure 3.5. Schematic diagram of energy levels of α-crystal and mesophase relative to amorphous.

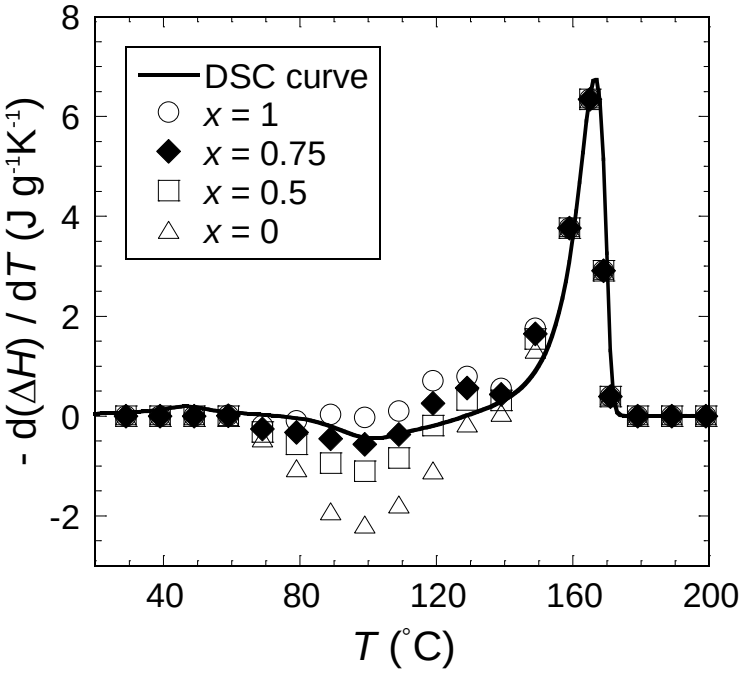

Figure 3.6. Temperature derivative of total enthalpy as a function of temperature for several numerical parameter *x* (see text).

References

1. Grebowicz, J., Lau, S.-F. & Wunderlich, B. The thermal properties of polypropylene. *J. Polym. Sci., Polym. Symp.* **71**, 19-37 (1984).
2. Cao, J. & Sbrrarski I. Determination of the enthalpy of solid phase transition for isotactic polypropylene using a modified DSC technique. *Polymer* **47**, 27-31 (2006).
3. Konishi, T., Nishida, K., Kanaya, T. & Kaji, K. Effect of isotacticity on formation of mesomorphic phase of isotactic polypropylene. *Macromolecules* **38**, 8749-8754 (2005).
4. Mileva, D., Androsch R. & Zhuravlev E. Temperature of melting of the mesophase of isotactic polypropylene. *Macromolecules* **42**, 7275-7278 (2009).
5. Konishi, T., Nishida, K. & Kanaya, T. Crystallization of isotactic polypropylene from prequenched mesomorphic phase. *Macromolecules* **39**, 8035-8040 (2006).
6. Bu, H., Cheng, S. Z. D. & Wunderlich, B. Addendum to the thermal properties of polypropylene. *Makromol. Chem. Rapid. Commun.* **9**, 75-77 (1988).

Chapter 4
Energy Levels of Mesophase of Poly(butylene-2,6-naphthalate)

4.1. Introduction

Poly(butylene-2,6-naphthalate) (PBN) is one of crystalline polyesters. Two kinds of crystal polymorphisms of PBN have been acknowledged as α-crystal and β-crystal up to the present [1, 2]. The monomeric unit of PBN consists of flexible part and rigid part, which are butylene and naphthalate, respectively. PBN is very easy to crystallize by just standing to cool from molten state; accordingly it is very difficult to obtain isotropic glass, *i.e.*, frozen state of melt, by cooling. This characteristic is contrast to the case of poly(ethylene terephthalate) (PET) although both are crystalline polyesters. The crystallization behavior of PBN at small quenching depths has been extensively studied in the past. However, the structure and thermal property of PBN at large quenching depths are not yet settled, because the fast crystallization rate of PBN at the large quenching depth makes it difficult to follow up the behavior at low temperatures.

At the large quenching depth, formation of mesophase has been reported for several polymers such as isotactic polypropylene (iPP), syndiotactic polypropylene (sPP) [3], polybutylene terephthalate (PBT) [4], poly(pentamethylene-2,6-naphthalate) (PPN) [5]. The mesophase is considered as intermediate state between that of amorphous and crystalline, and many researchers are interested in crystallization from mesophase.

In the case of iPP extensive studies have been performed for a long time to reveal that the mesophase iPP has flexible backbone and smectic-like structure [6]. The formation mechanism of the mesophase of iPP can be explained based on the concept of lyotropic liquid crystal assuming helical segments of iPP chains play a role of mesogens [7]. It was also confirmed by Konishi *et al*. [8] that PBN has the mesophase and its structure is smectic-like. Thus, the structure characteristics of the mesophase of PBN have been gradually revealed but the thermal characteristics are surprisingly obscure.

Differential scanning calorimetry (DSC) is usually a versatile method to examine

various transitions among states in polymer materials. However, this method is rather insensitive to investigate crystallization from mesophase, since the majority of the exotherm was completed during the formation of the mesophase and the remaining exothermic enthalpy is considered to be small as was reported by Konishi *et al*. [8]. In the case of iPP the measured enthalpy between mesophase and amorphous was often overestimated, because other transitions such as mesophase to amorphous coexisted during heating [9, 10].

In Chapter 3, in-situ wide-angle scattering measurements were performed for the crystallization process of iPP from mesophase during heating process using synchrotron radiation (SR) X-ray source, and the precise estimation of the energy level of the mesophase was successfully done by combining the structural information with thermal information obtained by DSC measurements. In this chapter, we applied the same method to mesophase PBN in order to evaluate the energy level of the mesophase of PBN.

4.2. Experimental Procedure

4.2.1. Materials and Sample Preparations

The specimen was PBN having an intrinsic viscosity of 1.40 dL/g [8]. The PBN sample was sandwiched between thin Kapton films was melted at 280 °C (>T_m) for 5 min on a hot stage, and then rapidly quenched to 0 °C by dipping into ice-water. The thickness of the sample film was ca. 150 μm. The obtained film was macroscopically transparent and showed two broad peaks in WAXD, which are the characteristics of mesophase PBN [8].

4.2.2. Measurements

DSC measurements were carried out with a Perkin-Elmer Diamond DSC at a heating rate of 10 °C/min. WAXD measurements were carried out using the beam line BL40B2 in the SR facility, SPring-8, Hyogo, Japan. Wavelength of the incident X-ray was 1.0 Å. The detector used was CMOS flat panel detector from Hamamatsu Photonics K.K. The exposure time was selected to be 1 s. A Mettler FP82HT hot stage was used to heat the specimens for WAXD measurements at the same heating rate as the DSC measurement. In both DSC and

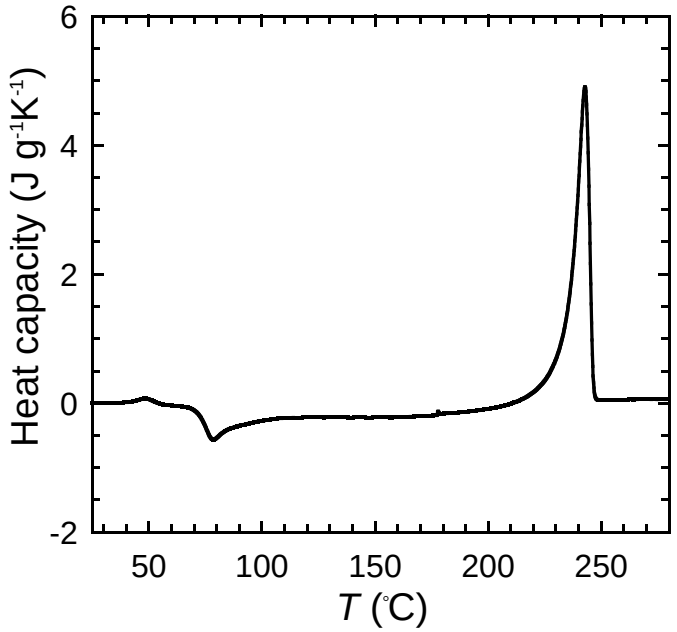

Figure 4.1. Observed DSC curve for mesophase PBN during heating process.

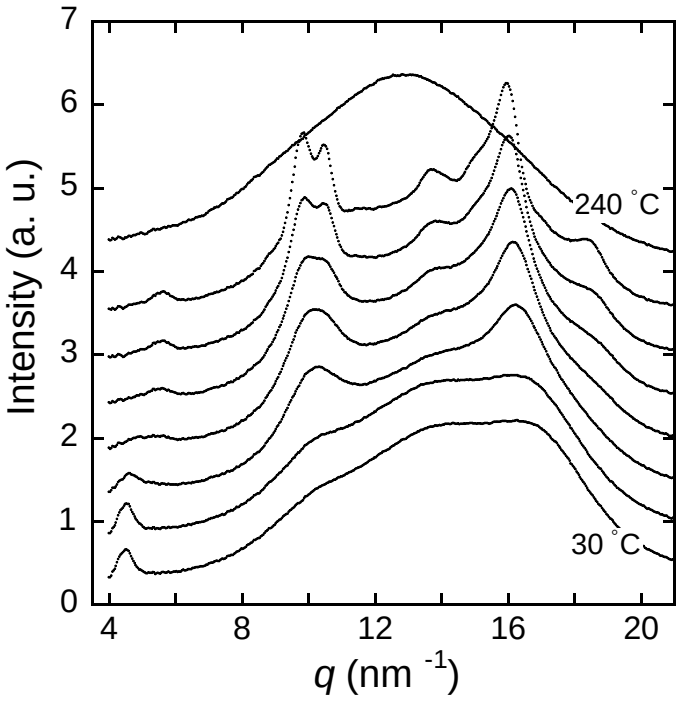

Figure 4.2. WAXD profiles during heating process from 30 to 240 °C displayed at every 30 °C from bottom to top. The profiles were shifted vertically for clarification.

WAXD measurements, thin films were tightly piled up to the same sample thickness, 0.7 mm, to apply similar thermal conduction within the samples.

4.3. Results and Discussion

4.3.1. Differential Scanning Calorimetry (DSC)

Figure 4.1 shows a DSC curve for mesophase PBN during a heating process. The curve shows a shoulder at around 40-50 °C. This shoulder is due to a glass transition [8]. An exothermal shallow peak is observed at around 80 °C. As will be turned out in the WAXD analysis, this exothermal shallow peak is due to the crossover between the formation of mesophase from melting state and the crystallization from the mesophase. Endotherm starts at around 200 °C and a distinct endothermic peak is observed at around 240 °C. It is unquestionable to assign the distinct endothermic peak to the melting of the crystal. Integrated areas of these exo - and endothermic peaks do not balance out. This is mainly because that the exothermic enthalpy when the mesophase transforms into crystal is small, as was mentioned in the introduction. However, it lacks proof to claim these explanations only with the DSC data. This will be discussed in the following section.

4.3.2. Wide-angle X-ray Diffraction (WAXD)

Figure 4.2 shows in-situ WAXD profiles during heating process from 30 to 260 °C. Sharp peak appearing at scattering vectors around q = 4.4 nm^{-1} and broad peak appearing at scattering vectors around 14 nm^{-1} for the profiles at low temperatures are characteristics of the mesophase PBN. The sharp peak at q = 4.4 nm^{-1} was assigned to (001) plane of mesophase, and the broad peak at q = 14 nm^{-1} was due to the lateral inter chains correlation [8]. Sharp peaks appearing at q = 5.8, 10.4, 10.9, 14, 15.7, 17, 18.3 nm^{-1} for the profiles of temperatures between 80 and 200 °C are reflections from α-crystal. Structure of α-crystal is triclinic, and the unit cell parameter of α-crystal are a = 4.87 Å, b = 6.22 Å, c = 14.36 Å, α = 110.1 ° , β = 126.9 ° , γ = 97.93 ° [1, 2].

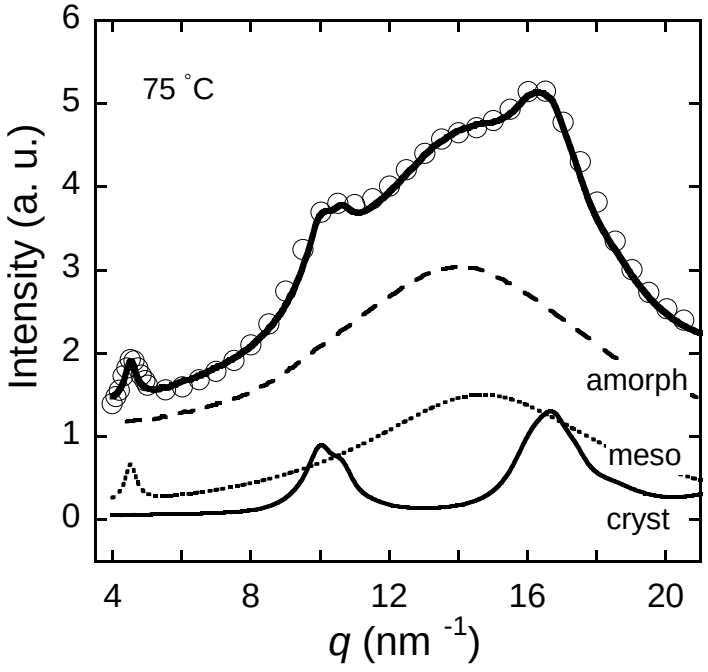

Figure 4.3. WAXD profile of mesophase PBN heated to 75 °C. Observed (open circle) and fitting (thick solid line) curve reproduced by summing up the constituents separated by the component analysis where α-crystalline form (thin solid line), mesophase (thin dotted lines), and amorphous phase (thin dashed line).

Single broad peak appearing at q = 13 nm^{-1} for the profiles at 240 °C is the amorphous halo. Component analysis for WAXD profiles was carried out to discuss the crystallization behavior quantitatively assuming each profile consists of three components such as α-crystal, mesophase, and amorphous. Here the crystalline and mesophase components are described by the assembly of Lorenz curves. A smoothed curve of the WAXD profile for the molten state is used as a reference curve for the amorphous component. Figure 4.3 shows typical example of fitting for component analysis. Thick solid line, which are the summations of the crystalline, mesophase and amorphous components, reproduce the observed WAXD profiles at 75 °C fairly well. Dividing the integrated intensity of each component by the integrated intensity of observed (total) intensity for each profile, fractions of α-crystal Φ_{cryst}, mesophase Φ_{meso} and amorphous Φ_{amorph} as a function of temperature during heating process were obtained, as shown in Figure 4.4. The fraction of mesophase and crystal were not changed at around 45 °C, so the shoulder in the DSC curve is confirmed to be due to a glass transition, as was mentioned above. The formation of mesophase slightly proceeded at around 80 °C, and crystallization from mesophase started at around 85 °C. Our previous study reported a glass transition of mesophase occurs at 65 °C [8], therefore the crystallization from mesophase and the formation of mesophase could be predicted to occur at the same time over 65 °C. In contrast, starting temperature of the formation of mesophase was lower than that of the crystallization from mesophase in fact. The reason can be considered that the mobility of mesophase is lower than that of amorphous. The crystallization from mesophase steeply proceeded in between 85 and 120 °C (meso-α transition); this behaviour is the most conspicuous at around 95 °C. During this process, the crystallization from amorphous hardly takes place. The crystalline fraction shows gradual increase in between 120 and 200 °C. The maximum crystalline fraction at this temperature is not coincident with the mesophase fraction at RT (Figure 4.4). A possible reason for this disagreement is that the heating rate of 10 °C/min is not slow enough to let the mesophase transforms into crystal to the full extent. The crystalline fraction starts to decrease above

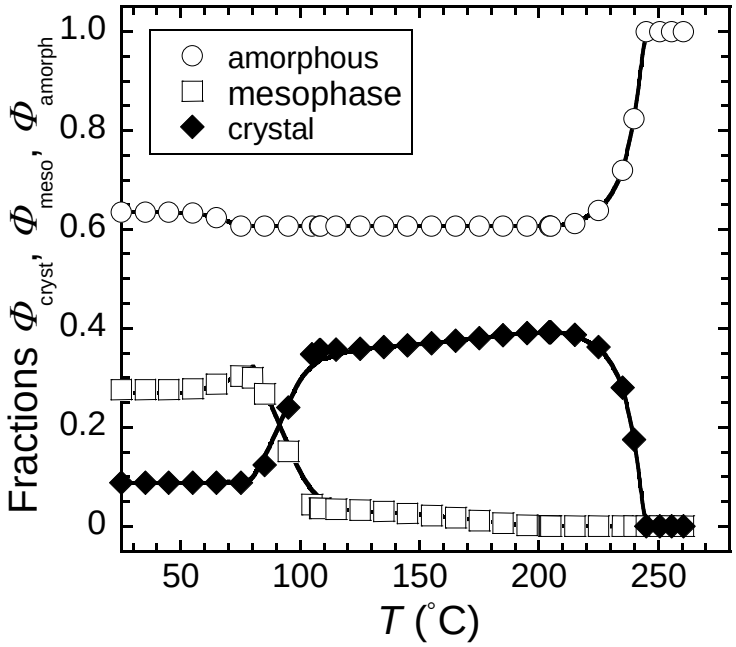

Figure 4.4. Fractions of α-crystal, mesophase and amorphous as a function of temperature during heating process.

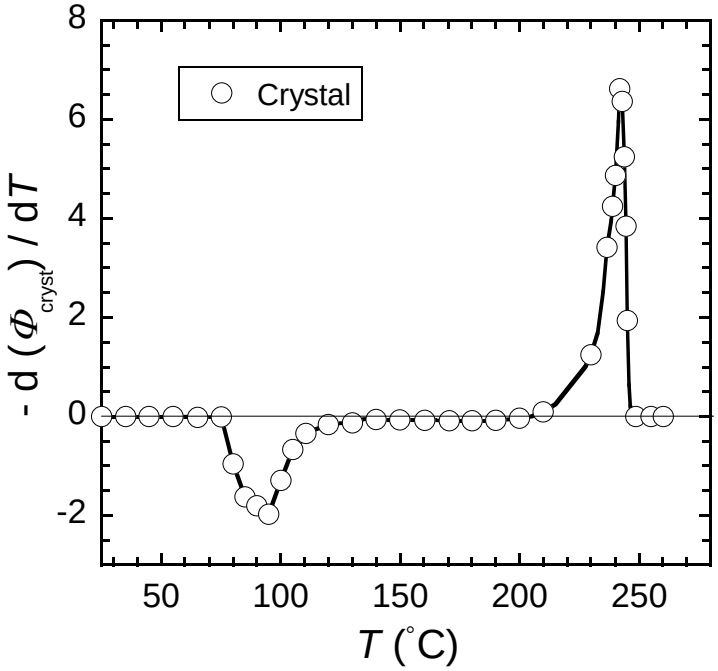

Figure 4.5. Temperature derivative of α-crystal fraction as a function of temperature.

220 °C and the most extensively decreases at around 240 °C. Temperature derivative of α-crystal fraction $-d\Phi_{cryst}/dT$ more clearly shows crystallization behavior from mesophase (Figure 4.5). The integrated areas for the crystallization peak at around 95 °C and that for the melting peak at around 240 °C are not equivalent due to the crystalline fraction at RT. This situation is different from crystallization of mesophase iPP during heating process in Chapter 3. Therefore, the shallow peak at around 95 °C observed in DSC (Figure 4.1) has definitely turned out to be due to the crystallization and the initial state of sample.

4.3.3. Energy Level of Mesophase

Figure 4.6 shows schematic diagram of energy levels of α-crystal and mesophase relative to amorphous. Assuming the melting enthalpy of mesophase (ΔH_{meso}) being x times of that of α-crystal (ΔH_{cryst}), namely $\Delta H_{meso} = x\ \Delta H_{cryst}$, the total enthalpy relative to amorphous $\Delta H(T)$ is given by the following equation;

$$\Delta H(T) = \Delta H_{cryst}\Phi_{cryst}(T) + x\ \Delta H_{cryst}\Phi_{meso}(T). \quad (4.1)$$

Temperature derivative of $\Delta H(T)$ gives expected value of heat balance. A reliable value of ΔH_{cryst} has not been reported yet, therefore the calculation of ΔH_{cryst} by comparing DSC results with WAXD analysis is necessary. The endothermic heat at the range from 220 °C to 250 °C was derived by just melting of α-crystal, and the value of integrated endotherm was 42.4 J/g. As was shown in Figure 4.1 and Figure 4.4, the amount of decrease of crystalline fraction is 0.393, so latent heat of fusion per crystallinity represented 107.9 J/g. by calculation of total endothem (42.4 J/g)/ max crystalline fraction (0.393). Unknown parameter is x. Figure 4.7 shows $-d(\Delta H)/dT$ plotted for several values of x. The case when $x = 0.7$ reproduces the experimental DSC well. It is essential to consider the balance among the fractions of α-crystal, mesophase and amorphous phase to obtain the reliable value. These results indicate this method is efficient to measure the mesophase of several polymers. Furthermore, it can be expected to be used for understanding the stability of mesophase in detail.

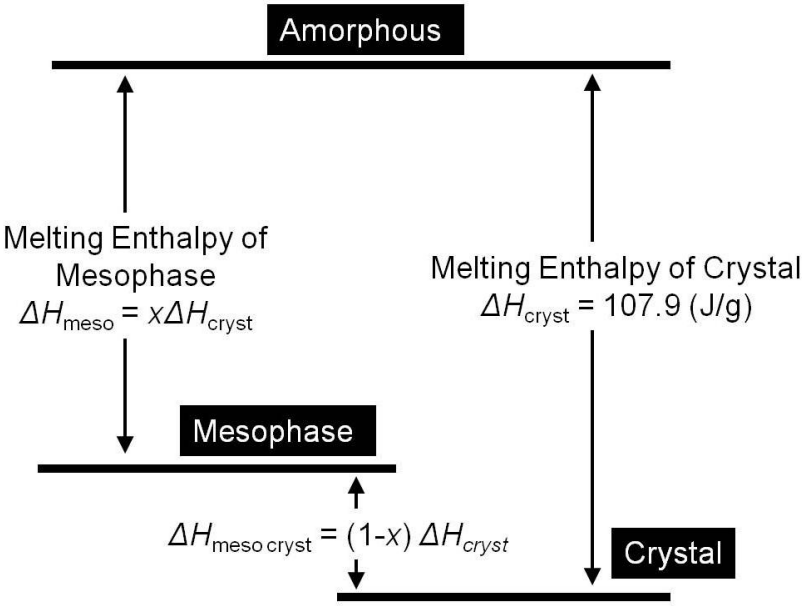

Figure 4.6. Schematic diagram of energy levels of α-crystal and mesophase relative to amorphous.

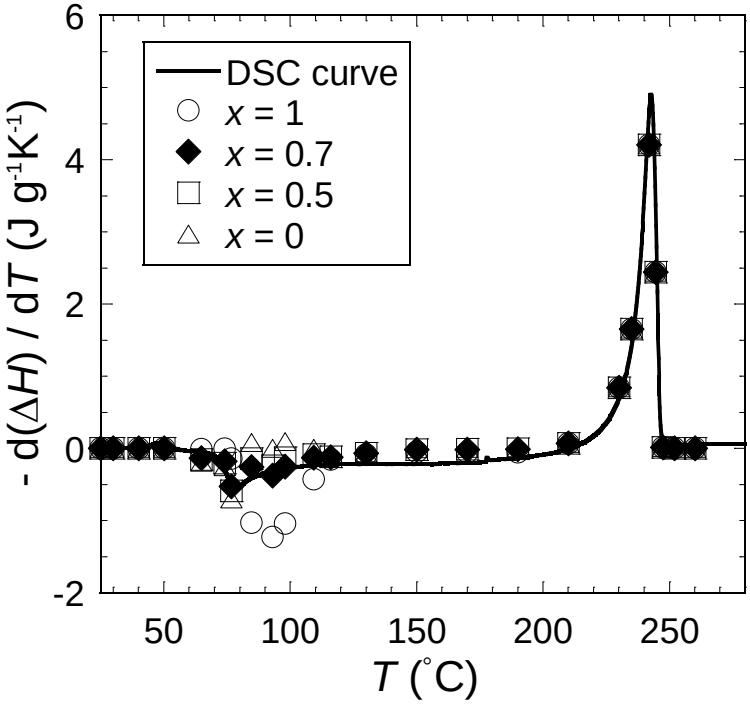

Figure 4.7. Temperature derivative of total enthalpy as a function of temperature for several numerical parameter *x* (see text).

References

1. Watanabe, H. Poly(butylene-2,6-naphthhalate) film no enshin to kouzou. *Kobunshi Ronbunshu* **33**, 229-237 (1976).
2. Koyano, H., Yamamoto, Y., Saito, Y., Yamanobe, T. & Komoto, T. Crystal structure of poly(butylene-2,6-naphthhalate). *Polymer* **39**, 4385-4391 (1998).
3. Vittoria, V. & Guadagno, L. Mesomorphic form of syndiotactic polypropylene. *Macromolecules* **33**, 6200-6204 (2000).
4. Konishi, T. & Miyamoto, Y. Crystallization of poly(butylene terephthalate) from the glass. *Macromolecules* **43**, 375-383 (2010).
5. Do, T. C., Jeon, H.-J., Song, H. H., Tashiro, K. & Ree, M. Mesomorphic phase in oriented poly(pentamethylene-2,6-naphthalate). *Polymer* **51**, 998-1001 (2010).
6. Natta, G. & Corradini, P. Structure and properties of isotactic polypropylene. *Nuovo Cimento Suppl.* **15**, 40-51 (1960).
7. Konishi, T., Nishida, K., Kanaya, T. & Kaji, K. Effect of isotacticity on formation of mesomorphic phase of isotactic polypropylene. *Macromolecules* **38**, 8749-8754 (2005).
8. Konishi, T., Nishida, K., Matsuba, G. & Kanaya, T. Mesomorphic phase of poly(butylene-2,6-naphthalate). *Macromolecules* **41**, 3157-3161 (2008).
9. Grebowicz, J., Lau, S.-F. & Wunderlich, B. The thermal properties of polypropylene. *J. Polym. Sci., Polym. Symp.* **71**, 19-37 (1984).
10. Cao, J. & Sbrrarski I. Determination of the enthalpy of solid phase transition for isotactic polypropylene using a modified DSC technique. *Polymer* **47**, 27-31 (2006).

Chapter 5
Heating Rate Effects on the Crystallization Behavior of Isotactic Polypropylene from Mesophase
–A De-polarized Light Transmission Study–

5.1. Introduction

Structural measurements, such as WAXD, SAXS, AFM, etc., generally require longer data acquisition time than the DSC measurements, therefore those techniques have not been applied to the fast heating process. In this chapter, we have applied a de-polarized light transmission (DPLT) method to investigate the crystallization of iPP from the mesophase. The DPLT method usually gives similar information to the DSC [1], because it is sensitive to the change in the degree of birefringence and the birefringence depends on the crystallinity. In fact, the DPLT has another advantage; the intensity of the DPLT is very sensitive to the size of the crystal grain even if the crystallinity is unchanged. Furthermore the DPLT requires only a short data acquisition time. This is the merit essential to apply the technique to the observation during fast scanning of temperature. As it will turn out later, these characteristics of the DPLT are especially useful to study the crystallization of iPP from the mesophase. In order to validate the characteristics of the DPLT measurements, the data obtained by the DPLT is compared with those obtained by the established methods, such as DSC, WAXD, and SAXS on the same heating condition. Combinatorial application of multiple methods synergistically helps us understand the polymer crystallization [2].

5.2. Experimental Procedure

5.2.1. Materials and Sample Preparations

The iPP material was supplied from Idemitsu Unitech Co., Ltd; the weight-average molecular weight was M_w = 353000, with a polydispersity of M_w/M_n = 4.4, and a degree of isotacticity (a meso pentad value) of *mmmm* = 0.98. This isotacticity is greater than the critical value (0.68) of isotacticity required to form the mesophase [3]. Sample films 200 μm

thick were prepared by quenching molten iPP to 0 °C by dipping them into ice water. Thus prepared films showed two broad peaks in WAXD pattern.

5.2.2. Hot Stage with Constant Heating Rates

Sample films of the mesophase iPP were heated from room temperature to 200 °C with various heating rates using a laboratory-made hot stage. The hot stage consisted of a heater block and a control unit. The heater block has a similar construction to the one that was previously used in a temperature jump experiment in Chapter 2. The control unit was assembled combining a programmable CPU unit KV-3000 and a PID temperature control unit KV-TF40 products of KEYENCE Japan. With increasing the heating rate, the temperature at the sample position tended to delay in comparison to the programmed one; therefore the heating rates were calibrated for each case using the actually measured temperature at the sample position. Accordingly, the values of the heating rate indicated in the results are not round numbers. The range of the heating rate after calibration covered from 10 to 124 °C/min.

5.2.3. De-polarized Light Transmission (DPLT) Measurements

The intensity of the light transmitted through the sample film was measured by utilizing the direct beam monitoring optics of a high-resolution small-angle light scattering instrument [4] with a diode laser of wavelength 405 nm as the light source. Utilization of this particular optics is efficient to measure the transmitted light at a good signal-to-noise ratio by suppressing the contamination of scattered light. A polarizer and an analyzer were inserted before and after the sample. By combination with a wide-dynamical range photometer, the measured intensity of transmitted light covered five orders of magnitude. The measuring time of the photometer was 0.2 s and the temperature error caused by this measuring time is approximately 0.4 °C in the case of the fastest heating rate (124 °C/min) of the present study. The intensity of the DPLT (I_{DPLT}) through a film, whose areal size is larger than the cross-section of light beam, is given by the following relation;

$$I_{\mathrm{DPLT}} \sim \sin^2(\pi \Gamma / \lambda) \qquad (4.2.1)$$

where Γ and λ are optical retardation and wavelength of light, respectively. The optical retardation Γ is a product of thickness of the film d and index of birefringence Δn. By analogy, I_{DPLT} for a case of dispersed cubic particles, whose dimension on a side is also d, is given by the following relation,

$$I_{\mathrm{DPLT}} \sim NS \sin^2(\pi d\Delta n/\lambda) \tag{4.2.2}$$

where N and S are number of particle and cross-sectional area of a particle (= d^2), respectively. In this case, a certain fraction of particles, whose relative orientation to the light beam fulfills the condition to produce the birefringence, can contribute to the intensity. When the value of $d\Delta n/\lambda$ is small enough, equation (4.2.2) can be approximated as follows;

$$I_{\mathrm{DPLT}} \sim Nd^4\Delta n^2 \tag{4.2.3}$$

The equation (4.2.3) tells that the DPLT is very sensitive to the size of a birefringent particle through the term d^4; *e.g.*, the value of I_{DPLT} becomes twice when the size of a particle becomes twice on the condition that the total volume of the particles and Δn are constant.

5.2.4. Complemental Measurements

The DPLT has an above-mentioned detection property for a hypothetical system that consists of cubic birefringent particles. However, its application to the particular crystallization of iPP has not been established yet. The validation of the DPLT method is performed by comparing with the data obtained by the established methods. Although equation (4.2.1) is an oscillatory function, it monotonically increases as long as the value Γ/λ does not exceed 1/2; otherwise the interpretation of the DPLT data will be complicated. We observed a polarization microscope (PM) for the sample, which showed the largest value of I_{DPLT} in the present study. The obtained image just showed dark grayish color, meaning that the value Γ is less than approximately 150 nm. Since the wavelength of light for the DPLT measurement is 405 nm, the value Γ/λ is estimated to be 0.37 at most; namely it does not exceed 1/2.

In order to get structural information on a mesoscopic scale, SAXS measurements were performed. The measurements were conducted using X-ray beam lines BL40B2 and BL03XU

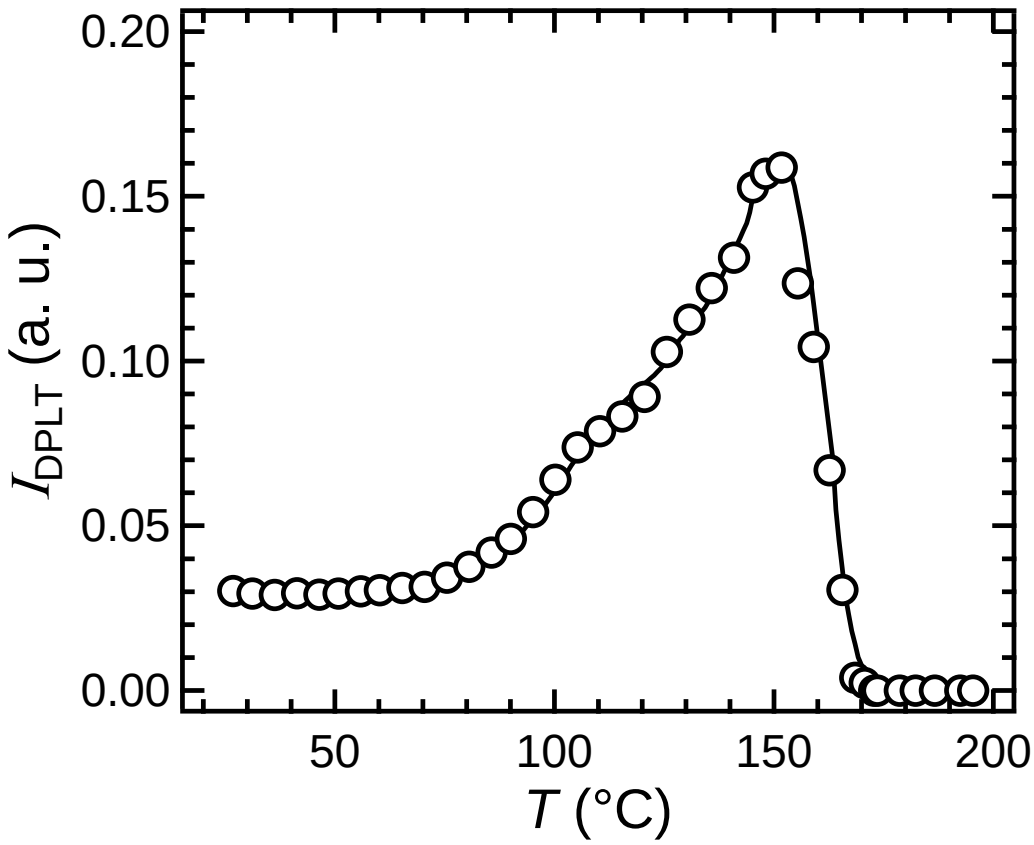

Figure 5.1. DPLT intensity I_{DPLT} as a function of temperature T, measured at a heating rate of 10 °C/min.

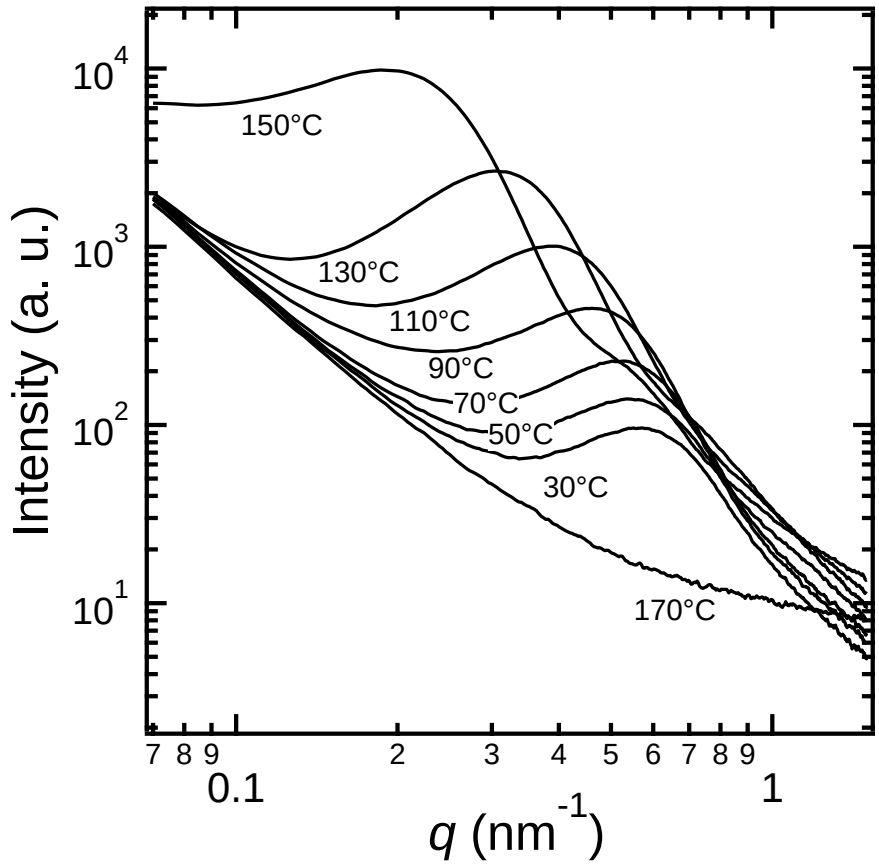

Figure 5.2. Temperature variation of SAXS intensity $I(q)$ of as a function of q, observed at a heating rate of 10 °C/min.

in a synchrotron radiation (SR) facility, SPring-8, Hyogo, Japan. In the present measurements, the wavelength of the incident X-ray λ was selected to 1.0 Å. The scattering vector q (= $4\pi\sin\theta/\lambda$) was covered from 0.07 to 2.0 nm^{-1}, where θ is a half of the scattering angle (2θ). After standard data processing, such as correcting detector sensitivity and subtracting scattering from the empty sample cell, the data were circularly averaged, because the 2D-data showed no anisotropy. The DPLT data were also compared with DSC and WAXD data that were taken on the same heating condition in Chapter 3.

5.3. Results and Discussion

5.3.1. Comparison of De-polarized Light Transmission (DPLT) with Other Methods

The present crystallization study was performed during non-isothermal heating processes. The DSC is one of the standard methods among the non-isothermal measurements. Therefore the data obtained by other methods, including the DPLT, are displayed in reference to the DSC's. In the non-isothermal DSC, the observed enthalpy ΔH as a function of temperature T is displayed in the form of a heat capacity $d(\Delta H)/dT$ or a heat flow $d(\Delta H)/dt$. Since the rates of structure formation will be discussed in this study, the DSC was handled in the form of the heat flow. The relation between the heat capacity and the heat flow is given by as follows,

$$d(\Delta H)/dt = d(\Delta H)/dT \times dT/dt. \quad (4.3.4)$$

It is a matter of preference; we took the positive side of the DSC chart as the endothermic and the negative side exothermic. Accordingly, also for other methods, the observed quantities were converted into the differential form and the rates of structure formations were displayed in the negative values when the data obtained by different methods are compared. The comparison was performed for the data obtained at a heating rate of 10 °C/min. Figure 5.1 shows a DPLT measurement, I_{DPLT} as a function of T, observed at a heating rate of 10 °C/min. At room temperature the I_{DPLT} showed a small but somewhat larger value than that of the isotropic molten state (see, T > 175 °C). This is because the mesophase iPP has locally a liquid crystal-like order although it is cellulated into the nodular domains. With increasing the

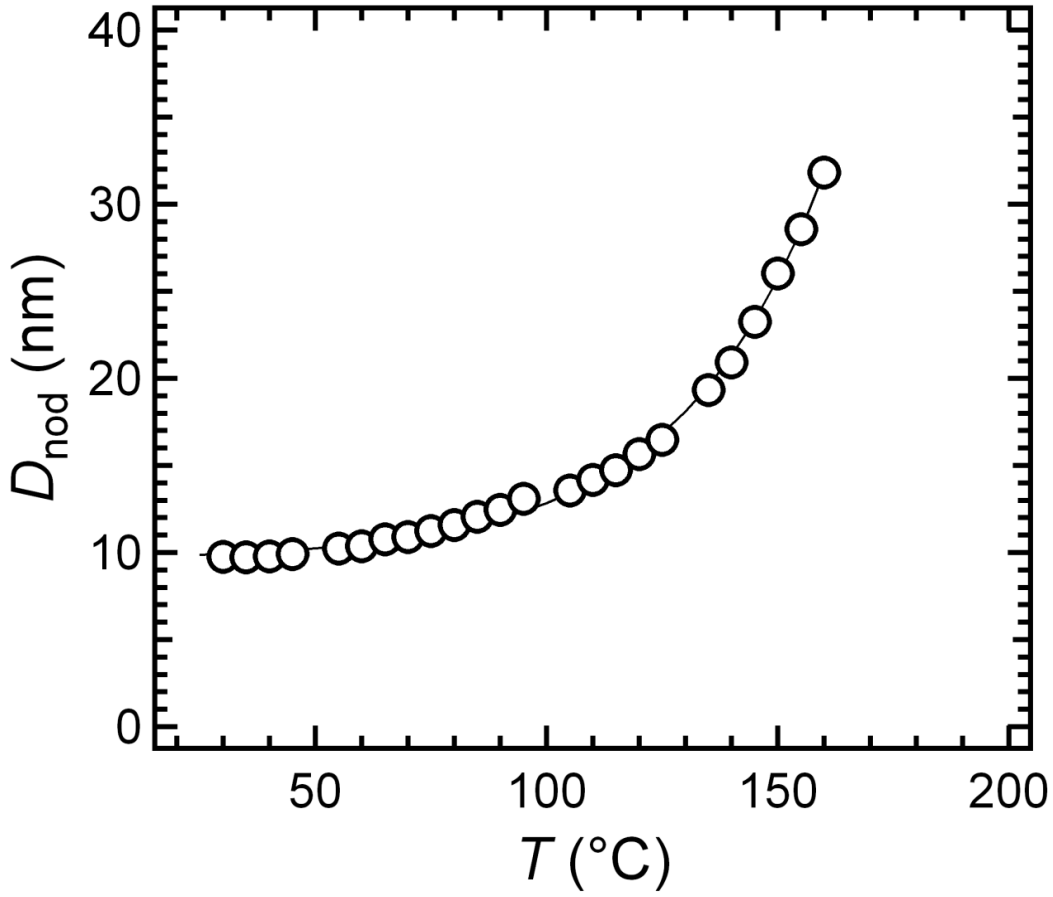

Figure 5.3. Diameter of nodule D_{nod} as a function of T at a heating rate of 10 °C/min.

temperature, the I_{DPLT} also increased showing two steeply increasing temperature regions around 100 and 145 °C, eventually it decreased very steeply around 165 °C. The steep decrease is unquestionably assigned to the melting of crystal. The interpretation for the two steep increases will be discussed later in the differential form referring the data obtained by other methods. The observed I_{DPLT} as a function of T was converted into the differential form similarly to equation (4.3.4) as follows,

$$dI_{DPLT}/dt = dI_{DPLT}/dT \times dT/dt. \quad (4.3.5)$$

The converted results $-dI_{DPLT}/dt$ as a function of T was displayed in Figure 5.4 (a). Figure 5.2 shows temperature variation of intensity $I(q)$ of SAXS as a function of q, observed at a heating rate of 10 °C/min. In agreement with the previously reported SAXS data observed during slow or stepwise heating, a broad maximum (q_{max}) was observed at approximately q = 0.6 nm^{-1} at room temperature and the maximum shifted toward the lower q side with the increasing the temperature, eventually the maximum disappeared above the melting temperature. The maximum in SAXS for the mesophase iPP is caused by the inter-nodular interference. Therefore the average diameter of the nodules D_{nod} is estimated by $2\pi/q_{max.}$ Figure 5.2 shows the D_{nod} as a function of T. With increasing the temperature, the D_{nod} also increased. In nodular systems, temperature dependence of D_{nod} has been explained by the Gibbs-Thomson effects [5]. The D_{nod} as a function of T was also converted into the differential form similarly to equation (4.3.4) as follows,

$$dD_{nod}/dt = dD_{nod}/dT \times dT/dt. \quad (4.3.6)$$

The converted results $-dD_{nod}/dt$ as a function of T was displayed in Figure 5.4 (b). In our previous paper, the crystallization behavior from the mesophase of iPP was studied using DSC and WAXD during the heating process at a rate of 10 °C/min in Chapter 3. There, we obtained the $d(\Delta H)/dT$ and the crystallinity Φ_{cryst} as a function of T. The $d(\Delta H)/dT$ was converted into $d(\Delta H)/dt$ according to equation (4.3.4) as mentioned above. The converted results $d(\Delta H)/dt$ as a function of T were displayed in Figure 5.4 (c). The Φ_{cryst} as a function of T was also converted into the differential form similarly to equation (4.3.4) as follows;

$$d\Phi_{cryst}/dt = d\Phi_{cryst}/dT \times dT/dt. \quad (4.3.7)$$

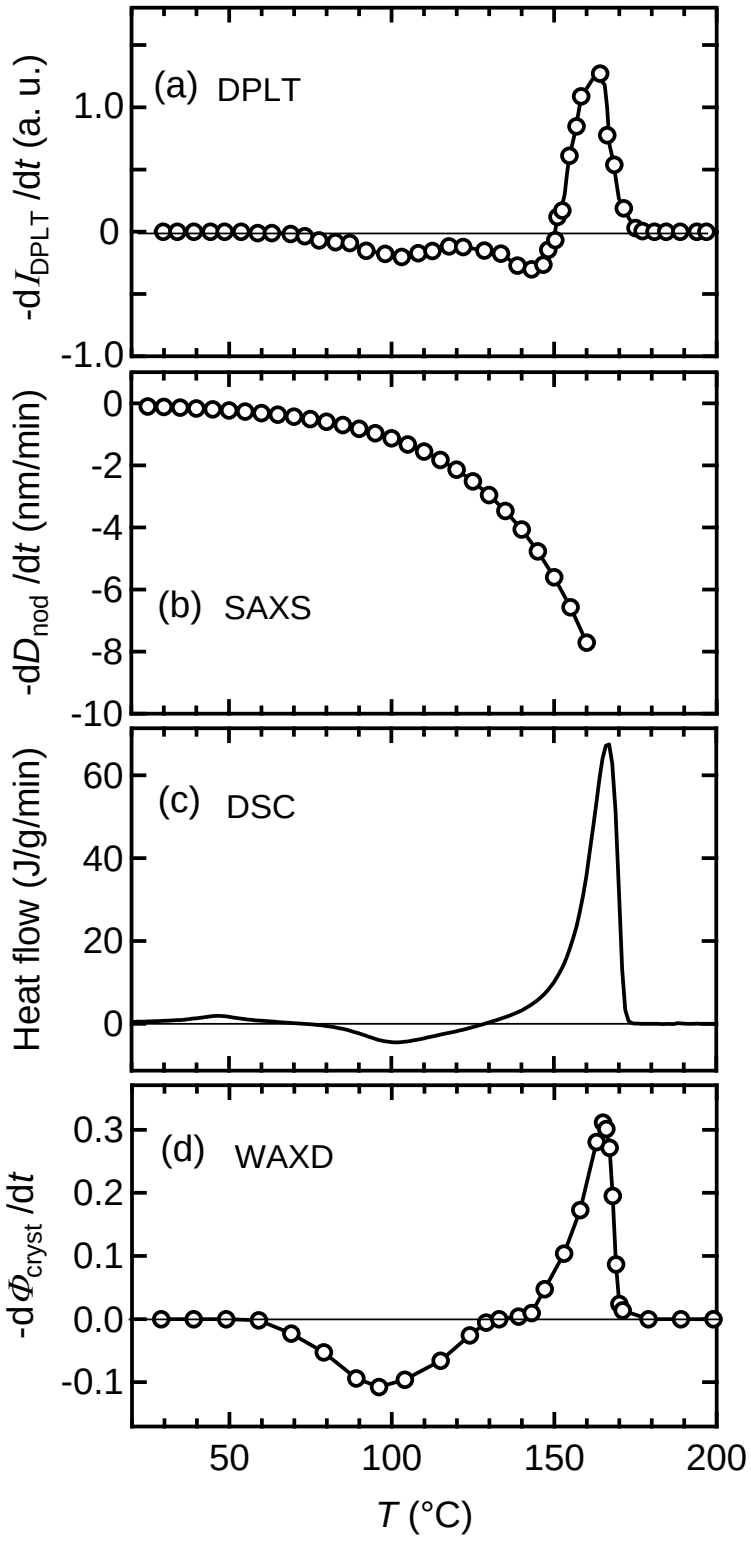

Figure 5.4. Methods-weighted rates of structure formations at a rate of 10 °C/min; parts (a), (b), (c), and (d) corresponds to the methods of DPLT, SAXS, DSC, and WAXD, respectively.

The converted results $-d\Phi_{cryst}/dt$ as a function of T were displayed in Figure 5.4 (d). Figure 5.4 shows a full set of the "methods-weighted rates" of structure formations from the mesophase of iPP during the heating process at a rate of 10 °C/min; parts (a), (b), (c), and (d) corresponds to the methods of DPLT, SAXS, DSC, and WAXD, respectively. Among these methods, the WAXD (Figure 5.4 (d)) gives the most neutral information in regard to the crystallization and melting, since only the fraction of crystalline phase Φ_{cryst} was extracted from the total WAXD profile by the component analysis [3]. A broad minimum around T = 100 °C and a rather sharp maximum T = 165 °C are assigned to the crystallization and the melting of crystal, respectively. This behavior is qualitatively similar to DSC's (Figure 5.4 (c)), however there are some quantitatively different points as follows. The integrated areas of the crystallization and the melting peaks balance out in the WAXD, whereas the integrated area of the crystallization peak is much smaller than that of the melting in the DSC. The imbalance in the DSC is due to the meta-stability of the mesophase of iPP in Chapter 3. Another difference is that only the DSC shows a glass transition-like behavior around 40-50 °C, since the structural measurements like WAXD is less sensitive to the relaxation phenomena. By comparing the DPLT (Figure 5.4 (a)) to the WAXD (Figure 5.4 (d)), the shallow minimum around T = 100 °C and a rather sharp maximum T = 165 °C are assigned to the crystallization and the melting of crystal, respectively. It should be noted that only the DPLT shows a specific minimum around 145 °C. To the contrary, the crystallinity is almost constant around 145 °C as is seen in the WAXD (Figure 5.4 (d)). Therefore, the specific minimum in the DPLT around 145 °C is not ascribed to the crystallization. The SAXS reflects the rate of grain size growth (Figure 5.4 (b)), independently of the crystallinity. The rate of grain size growth shows progressive increase towards the melting point. Considering this behavior and the detection property of DPLT as was discussed previously (see, equation (4.2.3)), the specific minimum around 145 °C in the DPLT should be assigned to the crystal grain growth. Thus the DPLT is sensitive to not only the crystallization but also the crystal grain growth. These two events did not take place simultaneously but they appeared at well-separated temperature regions (around 100 °C and 145 °C), when iPP was crystallized

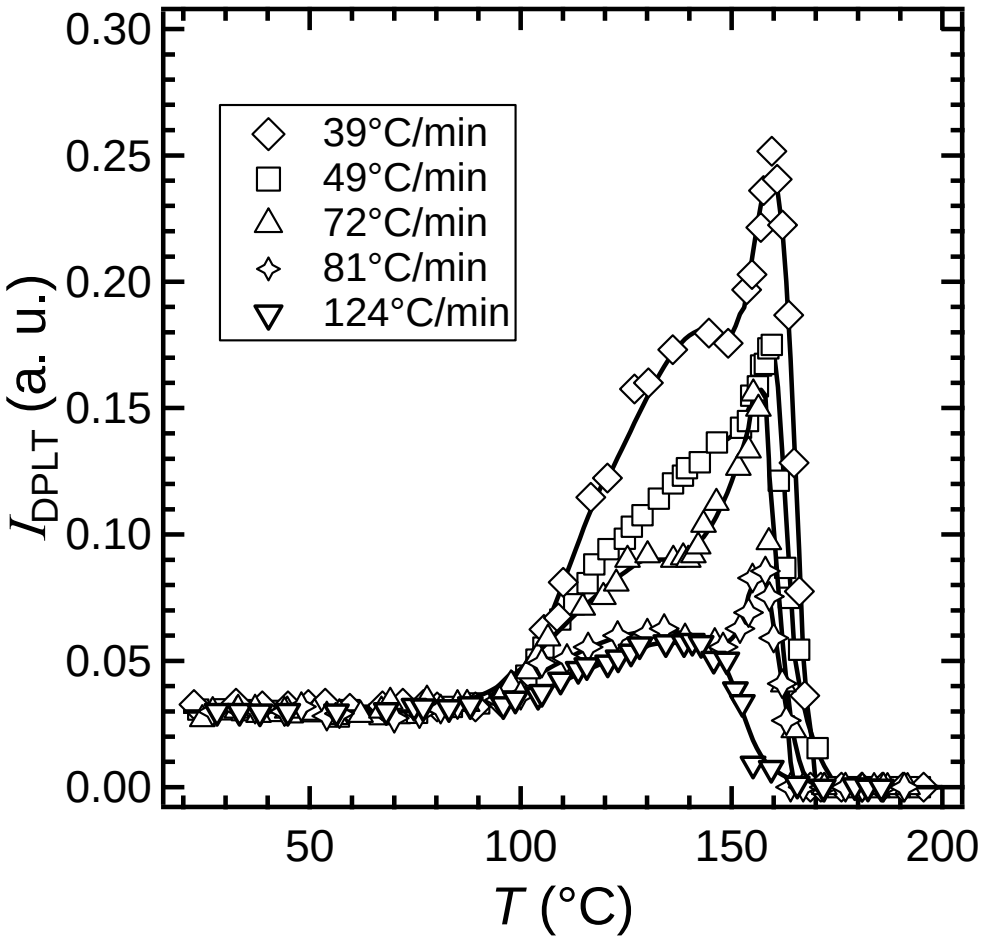

Figure 5.5. Heating rate variation of DPLT intensity I_{DPLT} as a function of temperature T.

from the mesophase by heating at a rate of 10 °C/min. In the former region (around 100 °C) it is obvious that the crystallization mainly proceeded by consuming the mesophase (meso-α transition); whereas in the latter region (around 145 °C) it is inferred that the crystal grain growth proceeded by partial melting and re-crystallization because the net crystallization rate was close to zero in this temperature region (Figure 5.4 (d)).

5.3.2. Heating Rate Effects on the Grain Growth Rate

Figure 5.5 shows the heating rate variation of the DPLT measurements, I_{DPLT} as a function of T, for the crystallization of iPP from the mesophase. In order to avoid overlapping, representative plots were displayed. These I_{DPLT} plots for different heating rates, except for 124 °C/min, showed qualitatively similar behavior to the one for 10 °C/min as was previously shown in Figure 5.1; I_{DPLT} increased showing two steeply increasing regions. The I_{DPLT} plot for 124 °C/min does not show the second steep increase. Further discussion on the heating rate effects for the DPLT is given in the differential form as follows.

Figure 5.6 shows the heating rate variation of $-dI_{DPLT}/dt$ as a function of T. In the differential form of the DPLT, the characteristic of the crystallization of iPP from the mesophase is readable; the first steep increase in the I_{DPLT} plots (Figure 5.5) appears as a broad minimum around 100-120 °C in $-dI_{DPLT}/dt$ (Figure 5.6) similarly to the crystallization peak in DSC and WAXD (Figure 5.4 (c) and (d)), and the second steep increase due to the crystal grain growth appears as a sharp minimum at a higher temperature region around 145-160 °C. With increasing the heating rate, the second minimum became more conspicuous (Figure 5.6 (b), (c)). In concert with the sharpening of the second minimum, a new maximum, which is small but a positive value, appeared between the first and second minimum. Considering the detection property of the DPLT and the definition of the $-dI_{DPLT}/dt$, the positive value means dissolution of a certain structure. Therefore, the appearance of this maximum together with the succeeding sharp minimum strongly suggests the partial melting and re-crystallization for the mechanism of crystal grain growth. Another important feature is that the second minimum disappeared when the heating rate was too high (Figure 5.6 (d)).

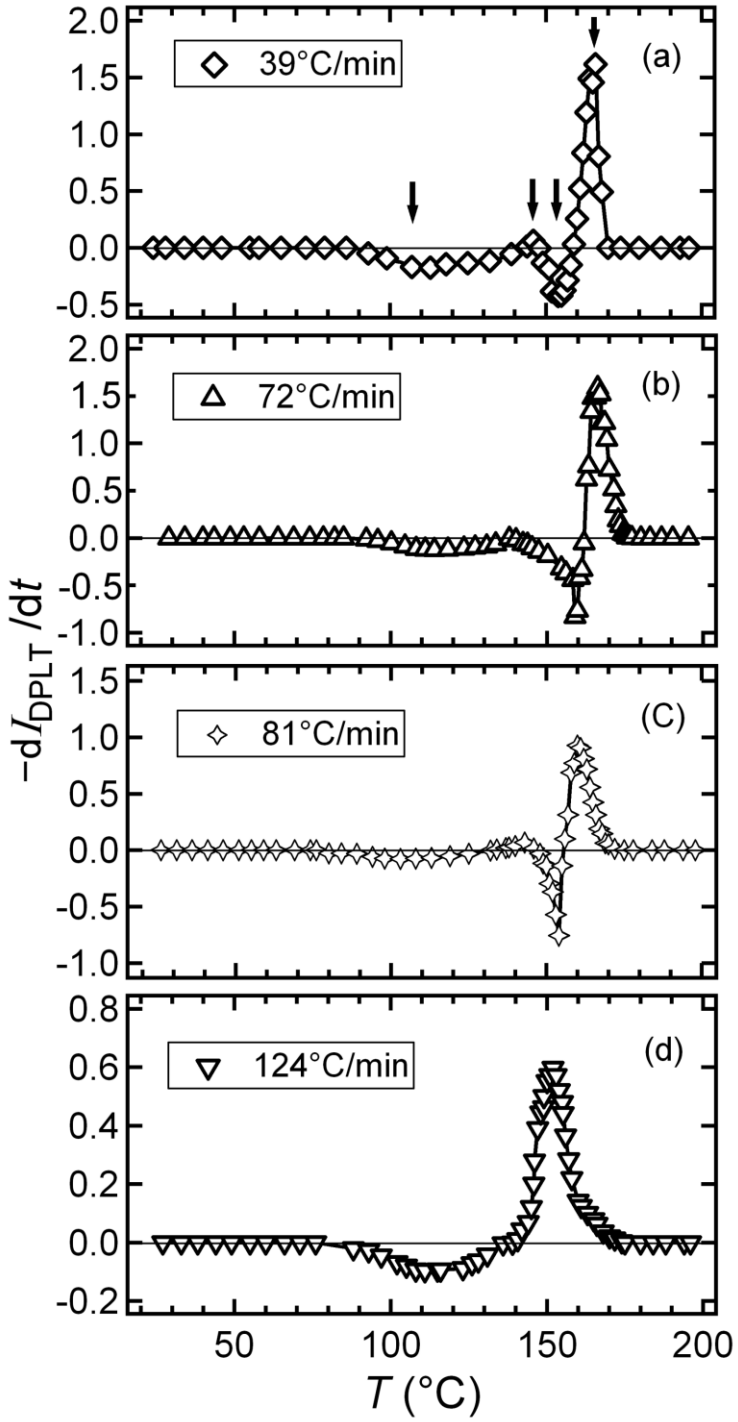

Figure 5.6. Heating rate variation of DPLT in differential form $-dI_{DPLT}/dt$ as a function of temperature T.

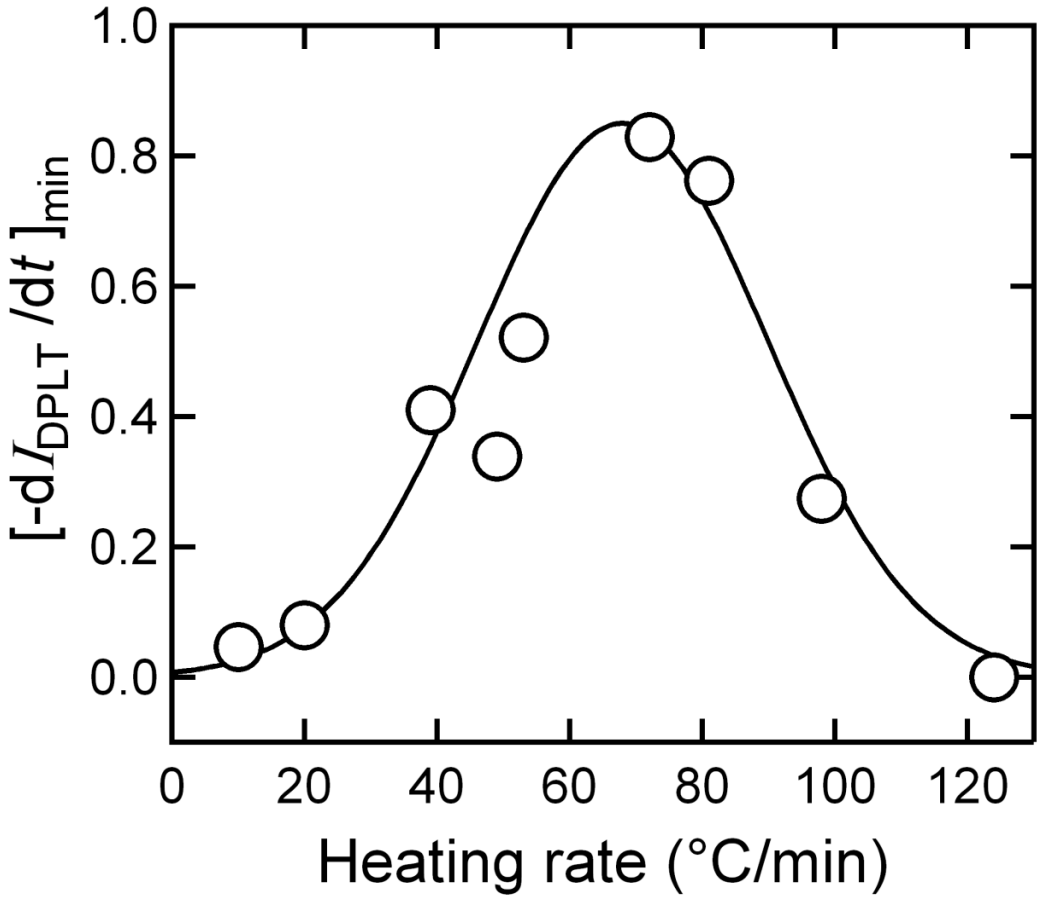

Figure 5.7. Depth of the second minimum in differential form of DPLT $[-dI_{DPLT}/dt]_{min}$ as a function of the heating rate.

This means that too fast heating prevents the crystal grain growth. Because again the low heating does not much promote the second minimum as was seen in Figure 5.4 (a), there should be an optimal heating rate favorable for the crystal grain growth.

Figure 5.7 shows the depth of the second minimum $[-dI_{DPLT}/dt]_{min}$ as a function of the heating rate. Although the plots of $[-dI_{DPLT}/dt]_{min}$ somewhat scatter, there is certainly a maximum around 60-80 °C/min. Present result is significant in order to optimize the heating rate. During the heating process of the mesophase iPP, the crystallization starts at considerably low temperature around 50-60 °C (Figure 5.4 (d)), which is just above the glass transition-like temperature located around 40-50 °C (Figure 5.4 (c)). When the heating rate is relatively small, effectively longer aging time is available in the low temperature region. Therefore, the crystallization is promoted in the low temperature region, although the crystallites are cellulated into nodules. In the meantime, the growth in nodule size is not yet conspicuous around 50-60 °C (Figure 5.4 (b)). If once nodules are thermally stabilized by the crystallization, they are relatively hard to merge into the larger size, in comparison to the less stabilized case. In other words, relatively large heating rate should promote the growth rate of the nodule size.

Figure 5.8 shows the heating rate variation of the growth rate of nodule $-dD_{nod}/dt$, as a function of T, for the crystallization of iPP from the mesophase. These data were extracted from the heating rate variation of SAXS measurements, which were performed similarly to Figure 5.2. At every heating rate, $-dD_{nod}/dt$ decreases, *i.e.*, the growth rate increases, with increasing the temperature until the melting. In the temperature region below 130 °C, the growth rate curves moved to the lower with increasing the heating rate. Namely, the grain growth is accelerated with increasing the heating rate at least in this temperature region. This trend is also valid in the temperature region above 130 °C except for the case of 64 °C/min. It should be noted that, the growth rate curve of 64 °C/min shows conspicuously small value, namely, the grain growth is very much accelerated in the temperature region above 130 °C. This behavior (SAXS) is consistent with the discussion for the heating rate effect on the DPLT measurements.

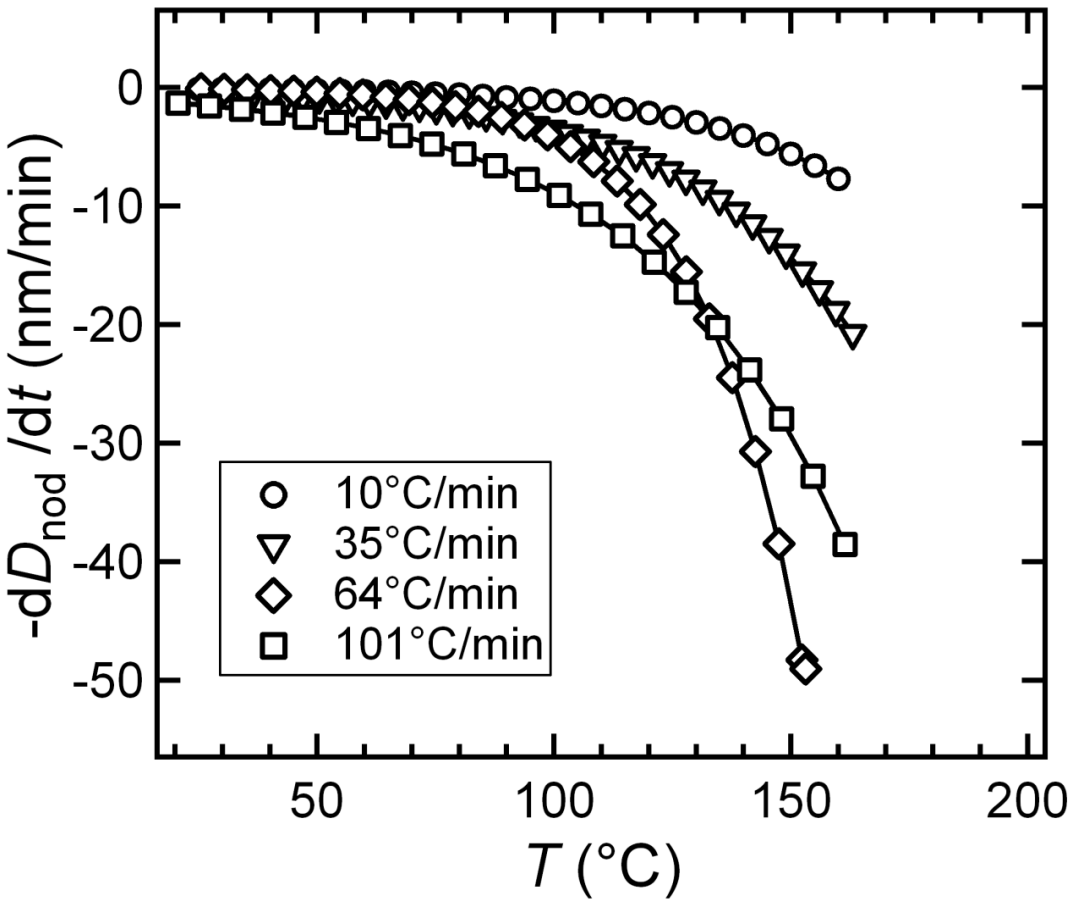

Figure 5.8. Heating rate variation of the growth rate of nodule $-\mathrm{d}D_{\mathrm{nod}}/\mathrm{d}t$, as a function of T.

5.4. Conclusion

The effectiveness of an application of the de-polarized light transmission (DPLT) method to the crystallization of iPP from the mesophase has been demonstrated. In the present study an optimal condition in regard to the heating rate was successfully obtained by utilizing the DPLT method in order to accelerate the crystal grain growth. However, some parameters, such as the isothermal temperature and the period to anneal subsequent to the heating at the specific rate, are left to be scanned in order to optimize the total conditions obtaining the "bamboo leaf-like (BL)" crystal of several tens micron in size, which is one of the ultimate cases of the large size of crystal grain.

References

1. Misztal-Faraj B., Sajkiewicz P., Savytskyy H., Bonchyk O., Gradys A. & Ziabicki A. Following phase transitions by depolarized light intensity. The experimental set up. *Polym*. *Test*. **28**, 36-41 (2009).
2. Su, C. H., Jeng, U., Chen, S. H., Lin, S. J., Wu, W. R., Chuang, W.-T., Tsai, J. C. & Su, A. C. Nanograin evolution in cold crystallization of syndiotactic polystyrene as illustrated via in-situ small/wide-angle X-ray scattering and differential scanning calorimetry. *Macromolecules* **42**, 6656-6664 (2009).
3. Konishi, T., Nishida, K., Kanaya, T. & Kaji, K. Effect of isotacticity on formation of mesomorphic phase of isotactic polypropylene. *Macromolecules* **38**, 8749-8754 (2005).
4. Nishida, K., Ogawa, H., Matsuba, G., Konishi, T. & Kanaya, T. A high-resolution small-angle light scattering instrument for soft matter studies. *J*. *Appl*. *Cryst*. **41**, 723-728 (2008).
5. Konishi, T., Nishida, K. & Kanaya, T. Crystallization of isotactic polypropylene from prequenched mesomorphic phase. *Macromolecules* **39**, 8035-8040 (2006).

Chapter 6
Giant Single Crystal of Isotactic Polypropylene Showing Near Equilibrium Melting Temperature

6.1. Introduction

Single crystal of isotactic polypropylene (iPP), of especially large size, has attracted interest of researchers for many years [1-12]. However, in the ordinary crystallization of iPP from the molten state, not the single crystal but the crystal aggregate, the so-called spherulite, is usually obtained. The spherulite consists of both crystalline lamella and non-crystalline amorphous regions, which are alternatively arranged with a certain periodicity, *i.e.*, the long period. In order to obtain thick lamella, very long time annealing at a high temperature is usually required; *e.g*. Hikosaka *et al*. obtained iPP spherulite with 66 nm thick lamellae by annealing at 166 °C for 6 months [13]. This record value of the lamella thickness attained a melting temperature of ca. 183 °C [14, 15], which is near the equilibrium melting temperature T_m^0. As for the T_m^0, several values were so far reported from 183.8 °C to 187.5 °C [14-17].

Besides the thickness of the lamella, the isolation between the lamellae or the crystallites is another important factor to qualify the single crystal [2, 4, 10]. Although such an isolated single crystal is rather readily obtained by the solution crystallization [3-7], it is difficult to obtain such one when iPP is crystallized from the bulk melt. The stacks and cross-hatches of lamellae easily occur during the crystallization from the bulk melt [18-22]. The branching of lamellae also blocks the formation of single crystal [18] and results in the formation of the spherulite. Due to those obstacles, usually the well-isolated single crystal of iPP exists only for the early stage of crystallization process [4, 12]. As a natural consequence, the size of the single crystal of iPP results in small when iPP is crystallized from the bulk melt.

In contrast to the above-mentioned ordinary crystallization of iPP from the molten state, we ever reported that a rapid heating of iPP from the mesophase yielded the large crystallite having needle-like or “bamboo leaf-like (BL)” morphology [9, 10, 11]. Since the BL crystal

was found by chance, neither the production mechanism nor the optimum of the production condition have not yet been clarified in detail. From a structural point of view, it was speculated at that time that the BL crystal is not the crystal aggregates like the spherulite but is the single crystal, because it showed very sharp X-ray diffraction peaks compared to the normal melt-crystallized spherulite and it showed a monochrome image within each domain of the BL crystal by a polarized microscope observation [9]. However, the thermal property, which correlates directly with the thickness of a single crystal, has not been clarified.

In Chapter 5 we have clarified that a certain temperature region just below the melting and a specific heating rate around 60-80 °C/min gave the maximum growth rate of the crystal grain when iPP was crystallized from the pre-quenched mesophase in Chapter 5. Although this result is very useful information to produce the BL crystal with good reproducibility, the optimal condition for the growth rate not necessarily corresponds to the optimal condition for the isolation of the crystal grain. Therefore, in the present study, managing the control of number density of crystallites in a unit volume, we will make it clear that the relationship between the melting point of the BL crystal and the production conditions, such as the heating rate from the mesophase and the annealing temperature.

6.2. Experimental Procedure

6.2.1. Materials and Sample Preparations

The iPP material was supplied from Idemitsu Unitech Co., Ltd; the weight-average molecular weight was M_w = 353000, with a polydispersity of M_w/M_n = 4.4, and a degree of isotacticity (a meso pentad value) of *mmmm* = 0.98. This isotacticity is greater than the critical value (0.68) of isotacticity required to form the mesophase [23]. Sample films 200 μm-thick were prepared by quenching molten iPP to 0 °C by dipping them into ice water. Thus prepared films were transparent macroscopically and showed two broad peaks in wide-angle X-ray diffraction (WAXD), which are the characteristics of the mesophase iPP [24, 25].

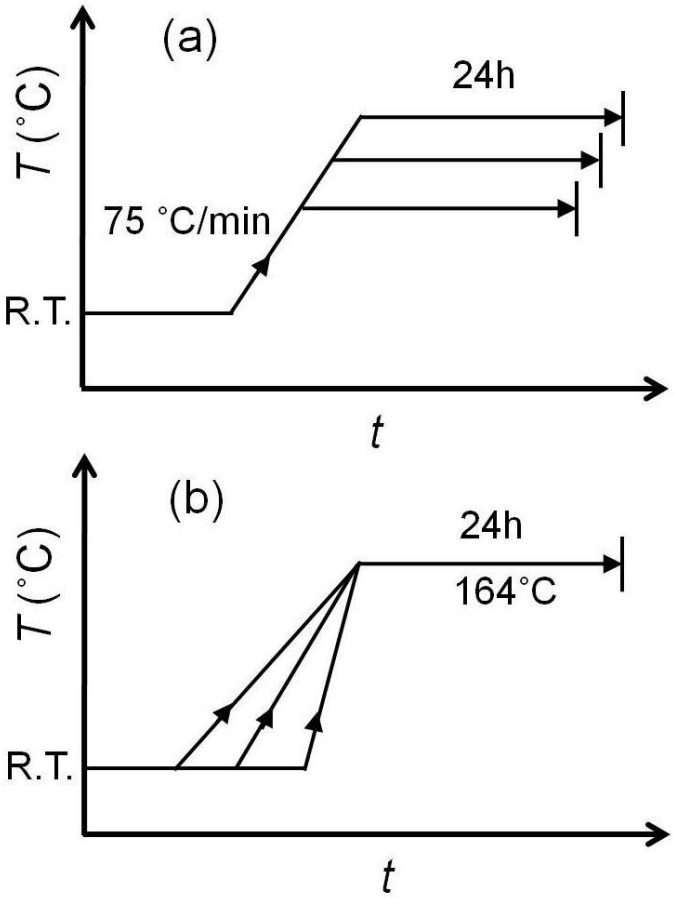

Figure 6.1. Time-temperature protocol. The heating rate is fixed at 75 °C/min and the final annealing temperature is scanned (a), and the final annealing temperature is fixed at 164 °C and the heating rate is scanned (b).

6.2.2. Time-temperature Protocol

As was mentioned in the introduction, the production condition of the BL crystal has already been narrowed down, namely a certain temperature region just below the melting and a specific heating rate around 60-80 °C/min gave the maximum growth rate of the crystal grain in Chapter 5. In this study we prepared two groups of time-temperature protocol around the above-mentioned condition; firstly the heating rate is fixed at 75 °C/min and the final annealing temperature is scanned (Figure 6.1 (a)), and secondly the final annealing temperature is fixed at 164 °C and the heating rate is scanned (Figure 6.1 (b)). In the both protocol, the period of the final annealing is fixed 24 h.

6.2.3. Optical Microscope Observation

Optical microscope observations were performed using an Optiphot2-Pol, a product of Nikon Japan. The bright field mode was used in order to avoid the counting loss of the number of the crystallites, since only the crystallites arranged in the specific orientation are detected in the polarized mode. The pre-quenched sample films were heated and annealed according to the prescribed protocol (Figure 6.1) using a laboratory-made hot stage [26]. The hot stage consisted of a heater block and a control unit. The heater block, to which the sample contacts, is controlled by a programmable CPU unit KV-3000 and a PID unit KV-TF40, products of KEYENCE Japan. The temperatures displayed in the results are calibrated ones using the actually measured temperatures at the sample position.

6.2.4. Differential Scanning Calorimetry

Differential scanning calorimetry (DSC) measurements were performed using a Diamond DSC, a product of Perkin-Elmer USA. The pre-quenched sample films were heated and annealed within the DSC instrument according to the prescribed protocol (Figure 6.1) in common with the optical microscope observations. Just succeeding the prescribed protocol, the DSC data were recorded during the heating process at a rate of 10 °C/min. In the latter heating process the melting behavior of the crystallites was observed. The temperature was

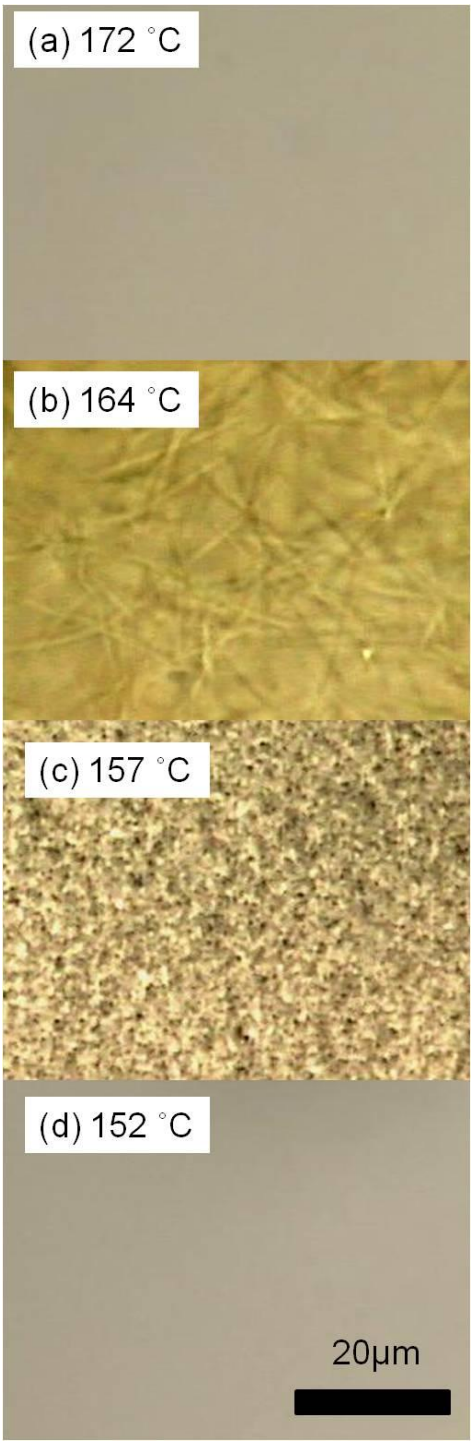

Figure 6.2. Selected images of optical microscope observations after the samples were annealed for 24 h at various temperatures succeeding the heating at a rate of 75 °C/min.

calibrated by the melting temperatures of pure In and Sn. All the measurements were performed under nitrogen environment.

6.3. Results and Discussion

6.3.1. Effect of Annealing Temperature on Crystallization

Figure 6.2 shows selected images of the optical microscope observations after the samples were annealed for 24 h at various temperatures (152-172 °C) succeeding the heating at a rate of 75 °C/min, according to the prescribed protocol (Figure 6.1 (a)).

As seen from Figure 6.2, the crystalline entities were detected only when the samples were annealed within a specific temperature window 157-164 °C. Within the specific window, the size and the number density of the crystallites were very much dependent on the annealing temperature; well-isolated large BL crystals were observed when the sample was annealed at 164 °C (Figure 6.2 (b)), whereas densely populated small crystallites, though not clear due to overlapping, were observed when the sample was annealed at 157 °C (Figure 6.2 (c)). On the outer side of the specific window, the images were merely transparent. The reasons for the transparency below and above the specific window are considered different as follows. Above the specific window (172 °C, Figure 6.2 (a)) the transparency is unquestionably due to the complete melting, *i.e.*, non existence of crystallites, whereas below the specific window (152 °C, Figure 6.2 (d)) the absence of the detectable entities does not mean the non existence of crystallites. At 152 °C most of the mesophase actually transforms into α-crystal [10, 27, 28], however, the α-crystal exists in the nodular form with the diameter of several tens nm at most [28]. The iPP film consisting of such nano-crystallites is macroscopically transparent [29]. Judging from Figure 6.2, the well-isolated large BL crystals are obtained when the pre-quenched mesophase iPP is annealed around 164 °C succeeding the heating at a rate of 75 °C/min.

6.3.2. Effect of Heating Rate on Crystallization

Figure 6.3 shows selected images of the optical microscope observations after the

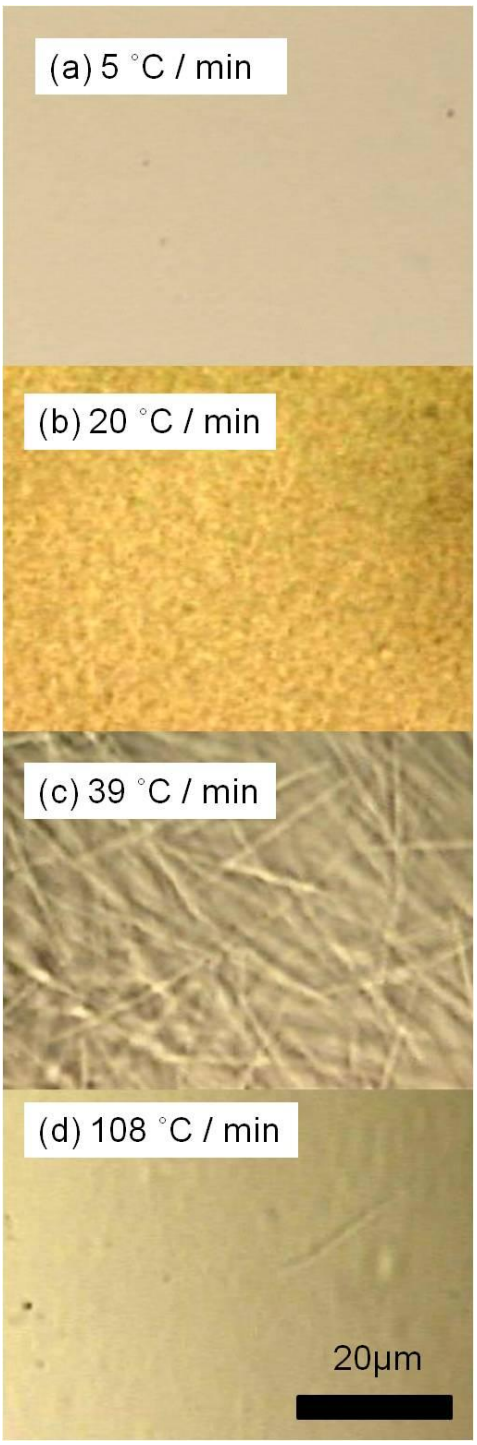

Figure 6.3. Selected images of optical microscope observations after the samples were annealed for 24 h at 164 °C succeeding the heating at various rates.

samples were annealed for 24 h at 164 °C succeeding the heating at various rates (5-108 °C/min), according to the prescribed protocol (Figure 6.1 (b)). As seen from Figure 6. 3, the crystalline entities were detected when the heating rate was more than 20 °C/min. At the rate of 5 °C/min, the images were merely transparent (Figure 6.3 (a)). The reason for the transparency is not the nonexistence of crystallites but the formation of the nano-crystallites similar to the case of Figure 6.2 (d). Densely populated small crystallites, though not clear due to overlapping, were observed when the sample was heated at the rate of 20 °C/min (Figure 6.3 (b)). At the rate of 39 °C/min, fairly well-isolated large BL crystals were observed (Figure 6.3 (c)). With increasing the heating rate, the isolation between neighboring crystallites was improved (75 °C/min, Figure 6.2 (b)). Finally, a unique isolated BL crystal within a scope was attained, when the heating rate reached 108 °C/min (Figure 6.3 (d)).

When the annealing temperature was fixed at 164 °C, the heating rate was proven to be an effective parameter to control the isolation and the morphology of the crystallites for the crystallization of iPP from the mesophase. Furthermore, it should be noted that the annealing temperature 164 °C is considered enormously high in an ordinary sense, because at such a high temperature it takes very long time for iPP to crystallize from the normal molten state [30]. It is one of the characteristics of the crystallization from the mesophase that the crystallization works properly at such a high temperature.

In what follows, the size and the number density of the obtained crystallites will be discussed quantitatively on the basis of the image analysis of the micrographs. First we determined the average longitudinal and lateral sizes, which were apparently read out from the micrographs. The thickness of the crystallites was far smaller than the detection limit of the optical microscope, so it will be discussed later based on the DSC analysis. Figure 6.4 shows a representative of the size-distribution histogram when iPP was crystallized at 164 °C succeeding the heating from mesophase at a rate of 75 °C/min. The condition corresponds to Figure 6.2 (b), but the sampling was performed covering the wider scope than the displayed one to get reasonable statistics. By fitting the Gaussian function to the histogram, the average and the standard deviation of the longitudinal and lateral sizes were obtained.

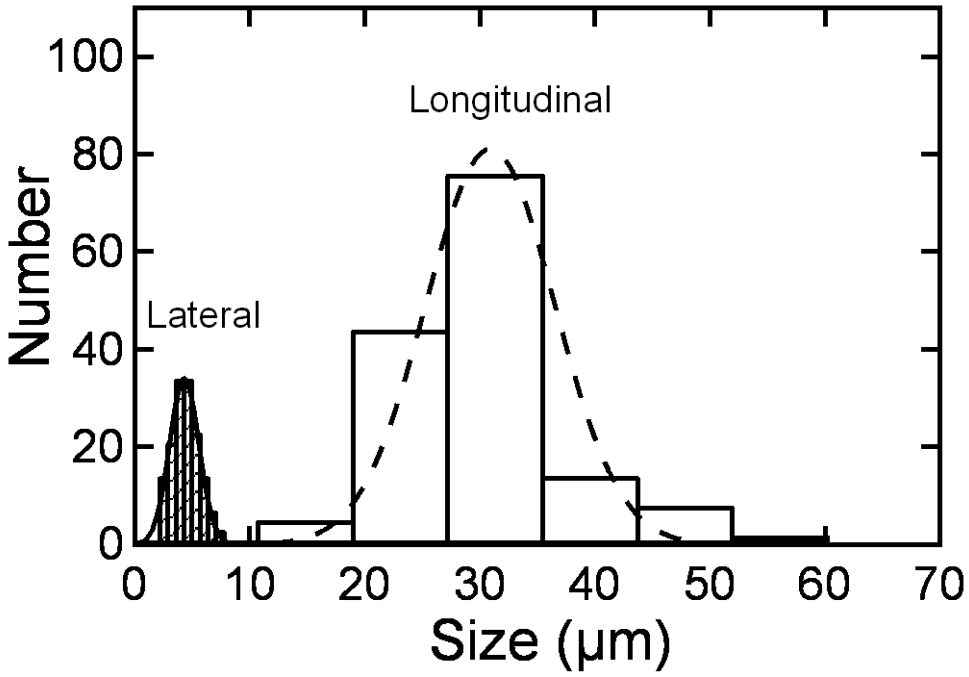

Figure 6.4. Size-distribution histogram of crystallites when iPP was crystallized at 164 °C succeeding the heating from mesophase at a rate of 75 °C/min.

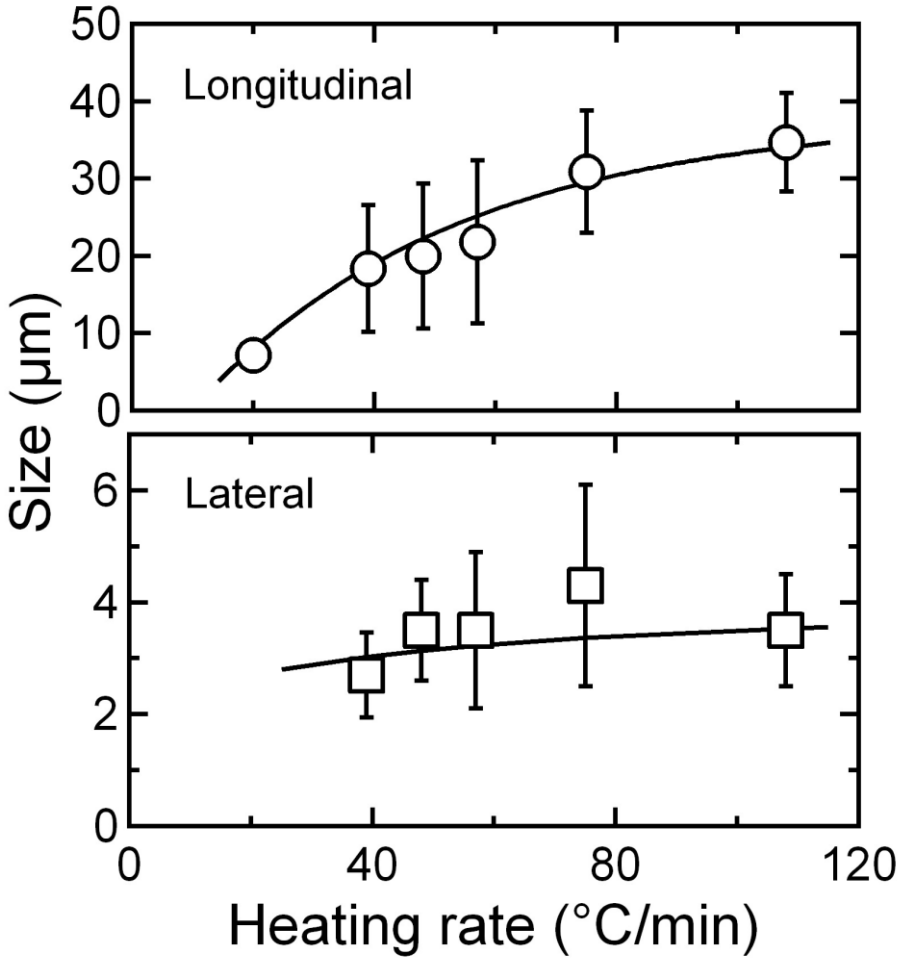

Figure 6.5. Longitudinal (a) and the lateral (b) sizes of the BL crystals as a function of the heating rate.

The longitudinal and the lateral sizes of the BL crystals as a function of the heating rate are shown in Figure 6.5 (a) and (b), respectively. With increasing the heating rate, the longitudinal size increased from ca. 7 μm and to ca. 35 μm. In the meantime, the lateral size also increased with increasing the heating rate, although the quantitative value at the thinnest case (heating rate of 20 °C/min) could not be determined due to the resolution of the microscope.

Dividing the longitudinal size by the lateral size, the aspect ratio of the BL crystals as a function of the heating rate was estimated and shown in Figure 6.6. Although the aspect ratio slightly increased with increasing the heating rate, it showed inherently high values around 5-10, as well as those of the single crystals that were produced at the early stage of the melt-crystallization [12].

The number density in a unit area was estimated by simply counting the number of crystallites within a unit area in the micrographs. Assuming that only the crystalline entities distributing within the focal depth were detected, the number density in a unit volume was calculated by dividing the number density in a unit area by the focal depth; the focal depth of the present optics was estimated to be 6.2 μm on the basis of the numerical aperture of the lens. Figure 6.7 shows thus estimated number density of the crystallites in a unit volume. The number density decreased approximately two orders of magnitude with increasing the heating rate until ca. 60 °C/min. Therefore the heating rate was proven to be an effective parameter to control the number density of the crystallites, namely the isolation between the single crystals can be controlled by the heating rate in the present specific crystallization from the mesophase of iPP. Further increase in the heating rate slightly decreased the number density.

6.3.3. Effect of Annealing Temperature on Melting Behavior

Figure 6.8 shows selected charts of the DSC measurements during heating scans at a rate of 10 °C/min for the samples annealed within the DSC instrument according to the prescribed protocol (Figure 6.1(a)) at various temperatures (130-167 °C) for 24 h. The heating scans were started from the prescribed annealing temperatures to 200 °C just succeeding

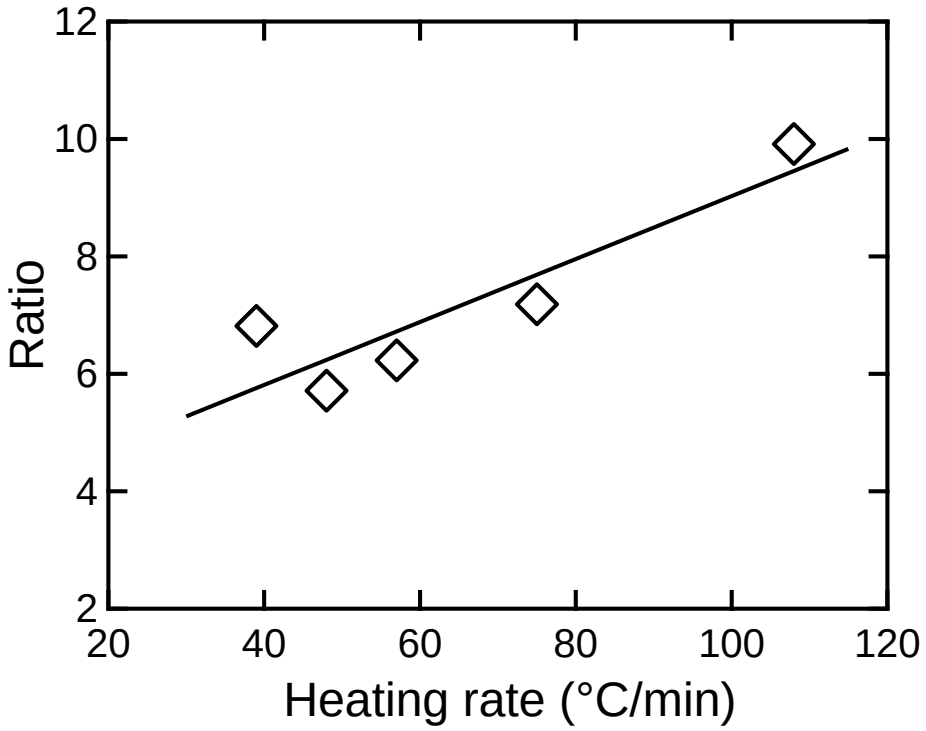

Figure 6.6. Aspect ratio of the BL crystals as a function of the heating rate.

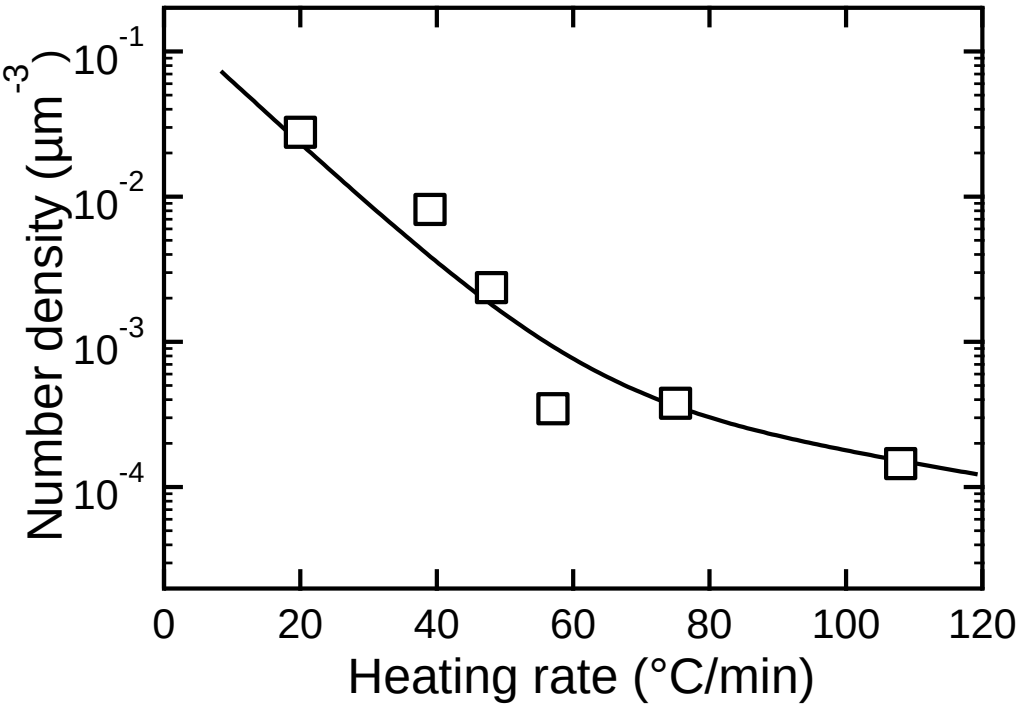

Figure 6.7. Number density of the crystallites in a unit volume as a function of the heating rate.

the annealing processes. As seen from Figure 6.8, the endothermic melting peak shifted towards higher temperatures with increasing the annealing temperature.

In Figure 6.9, the melting temperature T_m is plotted as a function of the annealing temperature or the crystallization temperature T_c, the so-called "Hoffman-Weeks plots". The thick solid line indicates the relation of $T_m = T_c$. The horizontal thin solid line indicates the iPP's equilibrium melting temperature T_m^0 (= 186.2 °C) reported by Toda *et al*. [14, 15]. In the normal Hoffman-Weeks plots, T_m is often proportional to T_c linearly or near linearly in the area above the $T_m = T_c$ line and the extrapolation to the $T_m = T_c$ line is considered to give the T_m^0 [31].

As is clear from Figure 6.9, the present behavior is quite different from the normal behavior of the above-mentioned Hoffman-Weeks plots. Below T_c = ca. 155 °C, T_m was almost independent of T_c. As was discussed the transparency of the micrograph obtained at 152 °C (Figure 6.2 (d)), the crystallites in this temperature region exist in the form of nodule. Therefore the T_m is restricted by the nodular size. Above T_c = ca. 155 °C, T_m increased rapidly and it seems to level off toward T_m^0. In this temperature region, the growth of crystallites is very much accelerated in Chapter 5. The gradient of the T_m *vs.* T_c plots is an index of the perfection and morphology of the crystal [31-34]; with approaching the infinitely thick defect-free crystal, the gradient decreases and becomes horizontal in the ultimate case. Therefore the observed asymptotic behavior is the indication that the present BL crystal is near the infinitely thick defect-free crystal.

The relations between the T_m and the thickness of the crystallites have been discussed quantitatively in literature [14-16]. Here, we estimated the thickness of the BL crystals according to the following relation proposed by Toda *et al*. [15].

$$T_m = 186.2 - 220/< l > \quad (6.1)$$

The values of T_m are dependent on the methods, such as optical microscope and DSC. In this study we have determined the T_m by DSC, so the thickness of the crystallites $< l >$ is an

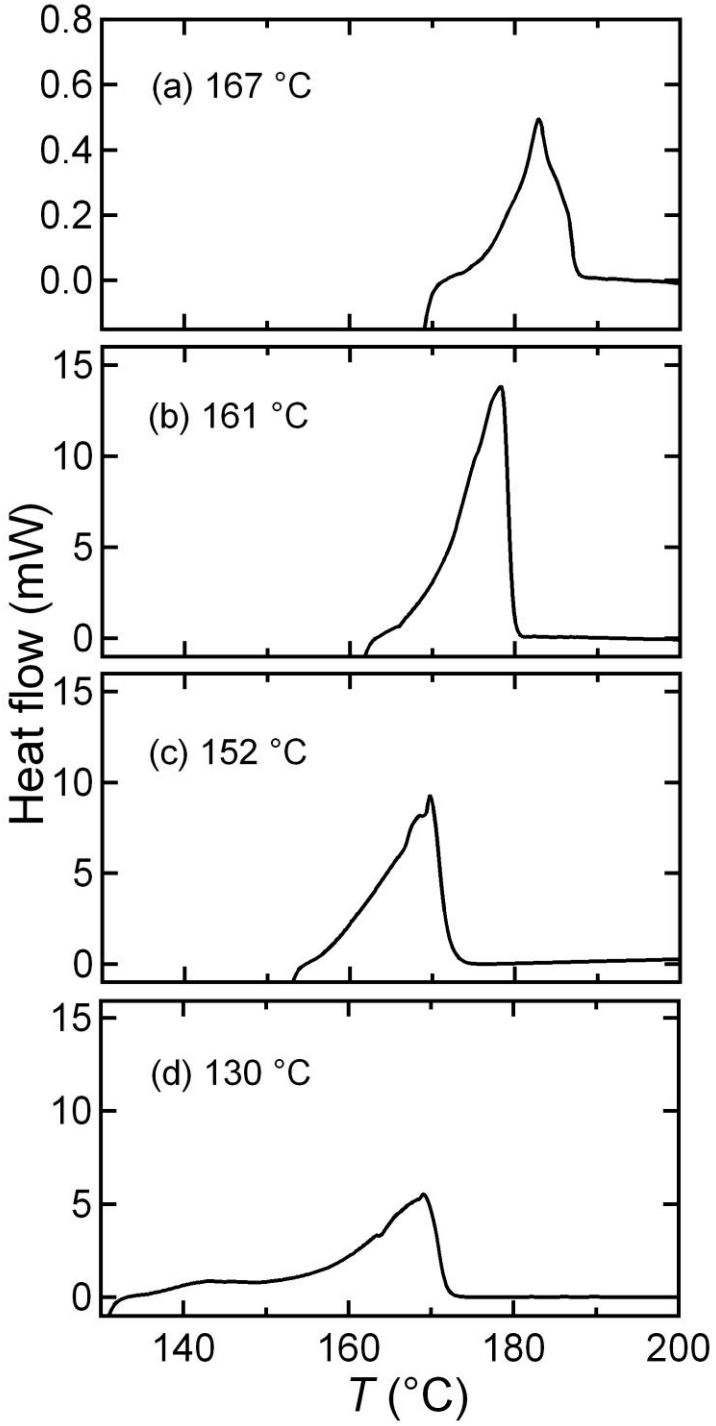

Figure 6.8. Selected DSC charts during heating scans at a rate of 10 °C/min for the samples annealed within the DSC instrument at various temperatures.

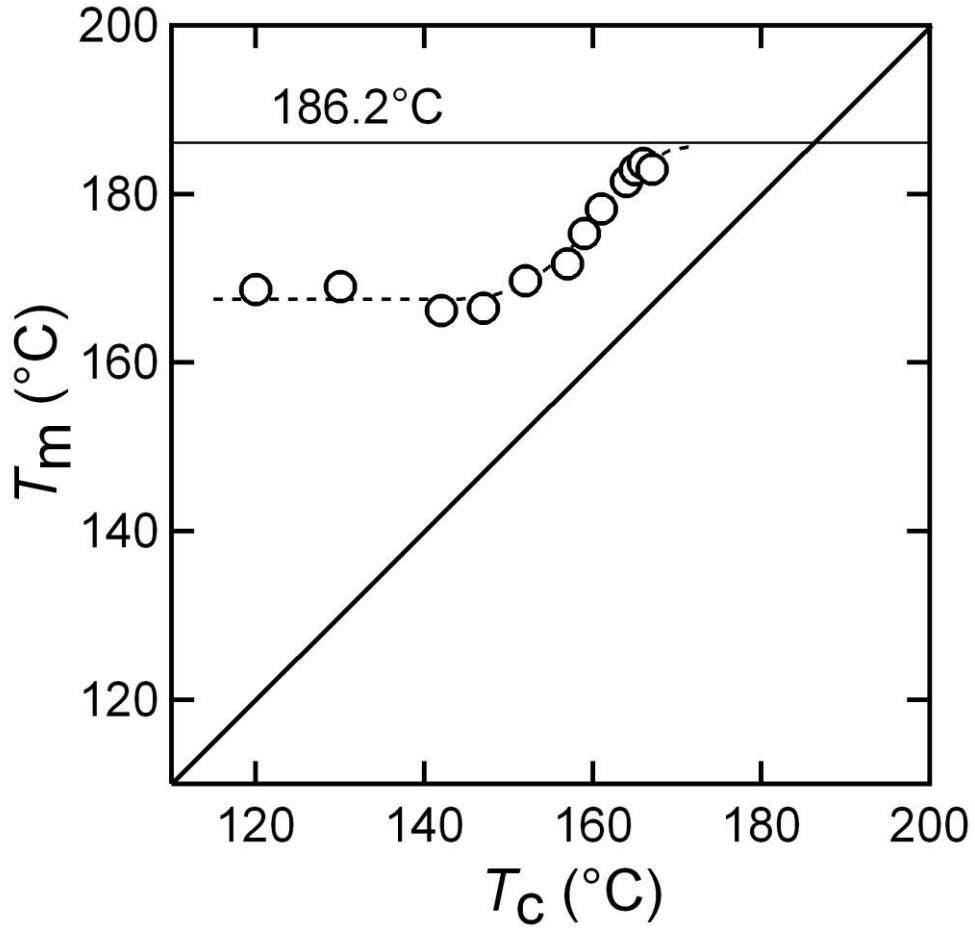

Figure 6.9. Melting temperature T_m as a function of the annealing temperature T_c.

averaged one weighted by the DSC. Figure 6.10 shows such an estimated value of $< l >$ as a function of the annealing temperature T_c. The $< l >$ was almost independent of T_c below T_c = ca. 155 °C as well as the behavior of T_m, whereas the $< l >$ showed a tendency to diverge above T_c = ca. 155 °C in contrast to the behavior of T_m. Apart from the diverging tendency, we have attained the crystal thickness of 88 nm. Although the obtained value is similar to or a little larger than the record value of the lamella thickness 66 nm when crystallized from the molten state [15], the present annealing process greatly saved the annealing time; it took 24 h when crystallized from the mesophase, whereas it took 6 months when crystallized from the molten state.

6.4. Conclusion

The giant single crystals of iPP have been obtained by a specific kinetic path through the mesophase. The obtained crystals possess the largeness without branching, the high aspect ratio, the isolation and the high melting temperature. These characteristics prove the quality of the single crystal. In addition to the quality, the present crystals are obtained in a relatively short annealing period.

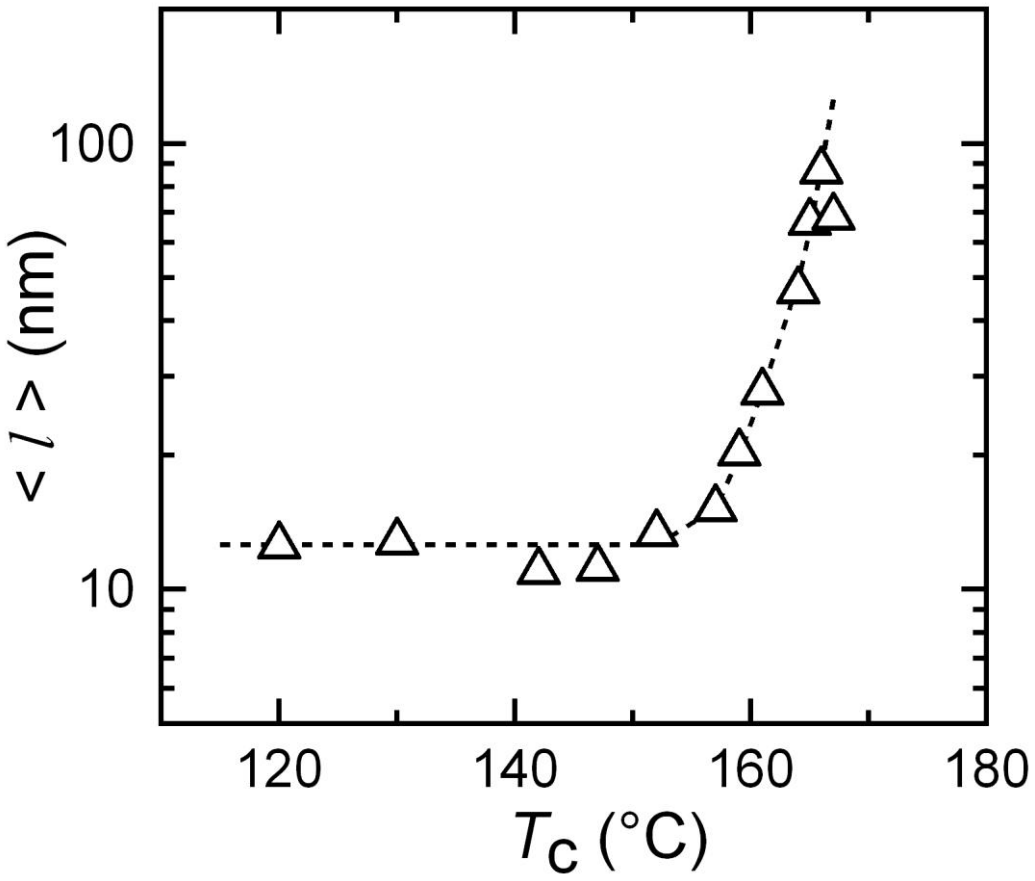

Figure 6.10. Thickness of the crystallites < *l* > as a function of the annealing temperature T_c.

References

1. Rånby, B. G., Morehead, F. F. & Malter, N. M. Morphology of *n*-alkanes, linear polyethylene, and isotactic polypropylene crystallized from solution. *J. Polym. Sci*. **44**, 349-367 (1960).
2. Geil, P. H. Folded molecules in lamellas crystallized from molten polymers. *J. Appl. Phys*. **33**, 642-643 (1962).
3. Sauer, J. A., Morrow, D. R. & Richardson, G. C. Morphology of solution-grown polypropylene crystal aggregates. *J. Appl. Phys*. **36**, 3017-3021 (1965).
4. Khoury, F. The spherulitic crystallization of isotactic polypropylene from solution: On the evolution of monoclinic spherulites from dendritic chain-folded crystal precursors. *J. Res. Natl. Bur. Stand. Sect*. **A70**, 29-61 (1966).
5. Kojima, M. Morphology of polypropylene crystals. I. Dilute solution-grown lamellar crystals. *J. Polym. Sci., Part A-2*: *Polym. Phys*. **5**, 597-613 (1967).
6. Kojima, M. Morphology of polypropylene crystals. II. Twinning of lamellar crystals. *J. Polym. Sci., Part A-2*: *Polym. Phys*. **5**, 615-622 (1967).
7. Padden, F. J. & Keith, H. D. Crystallization in thin films of isotactic polypropylene. *J. Appl. Phys*. **37**, 4013-4020 (1966).
8. Padden, F. J. & Keith, H. D. Mechanism for lamellar branching in isotactic polypropylene. *J. Appl. Phys*. **44**, 1217-1223 (1973).
9. Nishida, K., Konishi, T., Kanaya, T. & Kaji, K. Novel morphology of isotactic polypropylene crystal generated by a rapid temperature jump method. *Polymer* **45**, 1433-1437 (2004).
10. Konishi, T., Nishida, K. & Kanaya, T. Crystallization of isotactic polypropylene from prequenched mesomorphic phase. *Macromolecules* **39**, 8035-8040 (2006).
11. Zhao, J., Qiu, J., Niu, Y. & Wang, Z. Evolutions of morphology and crystalline ordering upon annealing of quenched isotactic polypropylene. *J. Polym. Sci., Part B: Polym. Phys.* **47**, 1703-1712 (2009).
12. Yamada, K., Kajioka, H., Nozaki, K. & Toda, A. Morphology and growth of single

crystals of isotactic polypropylene from the melt. *J. Macromol. Sci., Part B*: *Phys.* **50**, 236-247 (2010).

13. Maiti, P., Hikosaka, M., Yamada, K., Toda, A. & Gu, F. Lamellar thickening in isotactic polypropylene with high tacticity crystallized at high temperature. *Macromolecules* **33**, 9069-9075 (2000).
14. Yamada, K., Hikosaka, M., Toda, A., Yamazaki, S. & Tagashira, K. Equilibrium melting temperature of isotactic polypropylene with high tacticity: 1. Determination by differential scanning calorimetry. *Macromolecules* **36**, 4790-4801 (2003).
15. Yamada, K., Hikosaka, M., Toda, A., Yamazaki, S. & Tagashira, K. Equilibrium melting temperature of isotactic polypropylene with high tacticity. 2. Determination by optical microscopy. *Macromolecules* **36**, 4802-4812 (2003).
16. Cheng, S. Z. D., Janimak, J. J., Zhang, A. & Hsieh, E. T. Isotacticity effect on crystallization and melting in polypropylene fractions: 1. Crystalline structures and thermodynamic property changes. *Polymer* **32**, 648-655 (1991).
17. Wunderlich, B. *Macromolecular Physics Volume3*, 1-363 (Academic Press, New York, 1980).
18. Norton, D. R. & Keller, A. The spherulitic and lamellar morphology of melt-crystallized isotactic polypropylene. *Polymer* **26**, 704-716 (1985).
19. Vaughan, A. S. & Basset, D. C. Early stages of spherulite growth in melt-crystallized polystyrene. *Polymer* **29**, 1397-1401 (1988).
20. Olley, R. H. & Bassett, D. C. On the development of polypropylene spherulites. *Polymer* **30**, 399-409 (1989).
21. Janimak, J. J., Cheng, S. Z. D., Giusti, P. A. & Hsieh, E. T. Isotacticity effect on crystallization and melting in poly(propylene) fractions. 2. Linear crystal growth rate and morphology study. *Macromolecules* **24**, 2253-2260 (1991).
22. Yamada, K., Matsumoto, S., Tagashira, K. & Hikosaka, M. Isotacticity dependence of spherulitic morphology of isotactic polypropylene. *Polymer* **39**, 5327-5333 (1998).
23. Konishi, T., Nishida, K., Kanaya, T. & Kaji, K. Effect of isotacticity on formation of

mesomorphic phase of isotactic polypropylene. *Macromolecules* **38**, 8749-8754 (2005).

24. Natta, G. Progress in five years of research in stereospecific polymerization. *SPE. J.* **15**, 373-382 (1959).
25. Miller, R. L. On the existence of near-range order in isotactic polypropylenes. *Polymer* **1**, 135-143 (1960).
26. Nishida, K. Rapid temperature jump stage for optical microscope. *Proc. Polymer Processing Soc*. S17-631 (2008).
27. Zia, Q., Androsch, R., Radusch, H.-J. & Piccarolo, S. Morphology, reorganization and stability of mesomorphic nanocrystals in isotactic polypropylene. *Polymer* **47**, 8163-8172 (2006).
28. Zia, Q., Radusch, H.-J. & Androsch, R. Direct analysis of annealing of nodular crystals in isotactic polypropylene by atomic force microscopy, and its correlation with calorimetric data. *Polymer* **48**, 3504-3511 (2007).
29. Funaki, A., Kanai, T., Saito, Y. & Yamada, T. Analysis of Contributing factors toproduction of highly transparent isotactic polypropylene extrusion sheets. Part I. *Polym. Eng. Sci*. **50**, 2356-2365 (2010).
30. Radhakrishnan, J., Ichikawa, K., Yamada, K., Toda, A. & Hikosaka, M. Nearly pure α2 form crystals obtained by melt crystallization of high tacticity isotactic polypropylene. *Polymer* **39**, 2995-2997 (1998).
31. Hoffman, J. D. & Weeks J. J. Melting process and the equilibrium melting temperature of polychlorotrifluoroethylene. *J. Res. Natl. Bur. Stand. Sect.* **A66**, 13-28 (1962).
32. Baker, C. H. & Mandelkern, L. The crystallization and melting of copolymers I-The effect of the crystallization temperature upon the apparent melting temperature of polymethylene copolymers. *Polymer* **7**, 7-21 (1966).
33. Okui, N. & Kawai, T. Crystallization of ethylene/vinylacetate random copolymers. *Makromol. Chem*. **154**, 161-176 (1972).
34. Yoo, H. Y., Umemoto, S., Kikutani, T. & Okui, N. Co-crystallization behavior and melting-point depression in poly(ethylene terephtalate-co-1,4-cyclohexylene dimethylene

terephthalate) random copolyesters. *Polymer* **35**, 117-122 (1994).

Summary

The present thesis includes studies on structure, energy level of mesophase of isotactic polypropylene (iPP), the formation process of the mesophase from the melt and the crystallization process from the mesophase. The contents of the respective chapters are summarized as follows.

In Chapter 1, the author reviewed the previous studies on the polymer crystallization including classical nucleation and growth crystallization mechanism, crystallization mechanism via intermediate states, and recent progress of studies on the mesophase of iPP. In addition the author also described basic principles of scattering and de-polarized light transmission measurements to give a basis to understand the results obtained in the thesis. The motivation of the studies and the outline of the thesis were also described.

In Chapter 2, in-situ observation of the formation process of mesophase of iPP was performed from a structural point of view. A very rapid transformation from the molten state to the mesophase made in-situ observation difficult. In the present study, a rapid temperature jump and high-flux synchrotron radiation X-ray scattering techniques were combined to observe this transformation. Fast time-resolved wide-angle X-ray diffraction (WAXD) during the rapid cooling clearly revealed the time-evolution of the transformation process of the mesophase from the molten state. It was found that the transformation proceeded very quickly in a narrow temperature range below ca. 35 °C. Furthermore, the transformation was accompanied by instantaneous density fluctuations throughout the system, as visualized by microscopic observations. These observations suggested that the mesophase formation proceeded through a mechanism similar to spinodal decomposition.

In Chapter 3, energy level of the mesophase (metastable state) of iPP was examined by comparing the fractions of α-crystal, mesophase and amorphous phase obtained in WAXD and DSC measurements during the heating process. It was found that the ratio of the melting enthalpy of mesophase to that of α-crystal was 0.75.

In Chapter 4, mesophase of poly(butylene-2,6-naphthalate) (PBN) was studied, especially

focusing on the energy level of the mesophase of PBN. The same method as that used in Chapter 3 was applied to estimate the energy level. The fractions of α-crystal, mesophase and amorphous phase were obtained in the WAXD measurements during the heating process, and compared the WAXD results with those in the DSC ones. It was found that the ratio of the melting enthalpy of mesophase to that of α-crystal was 0.70 for PBN.

In Chapter 5, heating rate effects on the crystallization behavior from the mesophase of iPP was studied by utilizing a de-polarized light transmission (DPLT) method to find optimal condition to generate the bamboo leaf-like (BL) crystals. The DPLT sensitively detected the crystal grain growth in a narrow temperature region just below the melting temperature. With increasing the heating rate, both the temperature regions of the cold crystallization and the crystal grain growth shifted toward the higher temperatures. When the heating rate was slow below 20 °C/min, the crystal grain growth was not conspicuous. With increasing the heating rate, the rate of the crystal grain growth increased and showed a maximum when the heating rate was approximately 60-80 °C/min. However, excessively fast heating above 100 °C/min also suppressed the crystal grain growth.

In Chapter 6, the condition to generate large single crystals was studied using optical microscope and DSC. The giant single crystals of iPP were obtained by a specific kinetic path through the mesophase of iPP; pre-quenched mesophase of iPP was heated to 164 °C at a rate of 75 °C/min and kept at 164 °C for 24 h. The obtained crystallites showed a very high melting temperature T_m at 186 °C, which is ca. 20 °C higher than the iPP's nominal T_m (= ca. 165 °C); namely the observed T_m is immediately near the iPP's equilibrium melting temperature T_m^0 (= 186.2 °C). The crystallites have bamboo leaf-like (BL) or needle-like morphology having ca. 40 μm in length and ca. 3 μm in width. The thickness of the crystallites was estimated to be approximately 90 nm according to the melting temperature. The number density of the crystallites in a unit volume was controlled by adjusting the heating rate. As the result, well-isolated single crystals of iPP having the above-mentioned morphology were obtained.

List of Publications

In-situ observations of mesophase formation of isotactic polypropylene–Fast time-resolved X-ray diffraction study

Nishida, K., Okada, K., Asakawa, H., Matsuba, G., Ito, K., Kanaya, T. & Kaji, K.

Polym. J. **44**, 95-101 (2012).

(Chapter 2)

Crystallization of isotactic polypropylene from mesomorphic phase: a constant heating rate study

Asakawa, H., Nishida, K., Matsuba, G., Kanaya, T. & Ogawa, H.

J. Phys.: *Conf. Ser*. **272**, [012024-1]-[012024-4] (2011).

(Chapter3)

Energy levels of mesophase of poly(butylene-2,6-naphthalate)

Asakawa *et al*.

in preparation

(Chapter 4)

Heating rate effects on the crystallization behavior of isotactic polypropylene from mesophase – A de-polarized light transmission study–

Asakawa, H., Nishida K., Yamamoto, J., Inoue, R. & Kanaya, T.

Submitted to *Polymer*

(Chapter 5)

Giant single crystal of isotactic polypropylene showing near equilibrium melting temperature

Asakawa, H., Nishida, K. & Kanaya, T.

Submitted to *Polym. J*.

(Chapter 6)

Acknowledgements

This thesis is based on the study carried out under the supervision of Professor Toshiji Kanaya, Laboratory of Polymer Material Science, Division of Fundamental Material Polymer Properties, Institute for Chemical Research, Kyoto University, from 2008 to 2012.

The author would like to express his sincere gratitude to Professor Toshiji Kanaya for his continuous guidance and valuable advices.

Professor Hirokazu Hasegawa and Professor Yoshinobu Tujii are especially acknowledged for their review of this thesis.

The author is deeply indebted to Associate Professor Koji Nishida for his continuous guidance, discussions and encouragements.

The author also wishes to express his sincere thanks to Emeritus Professor Keisuke Kaji for his helpful discussions of this study.

The author is sincerely grateful to Dr. Rintaro Inoue for his helpful advices and encouragements. The author is also deeply grateful to Associate Professor Go Matsuba (Yamagata University) for his experimental guidance and helpful advices.

Further thanks are extended to Dr. Hiroki Ogawa (JASRI), Hiroyasu Masunaga (JASRI) and Dr. Kazuki Ito (Rigaku Co.) for his kind support in X-ray scattering experiments at SPring-8. The author is also deeply grateful to Dr. Takahiko Kawai (Gunma University) and Dr. Takashi Konishi (Kyoto University) for their helpful advices.

The author appreciates all the students and secretary (Ms. Hanako Ishida) of Professor Kanaya's laboratory. Especially, the author wishes to expresses his thanks to Mr. Junpei Yamamoto, Mr. Kazuma Okada, Mr. Norihiro Matumoto and Mr. Yasuhiro Hanamoto for their collaborations throughout this study at Kanaya laboratory.

Finally, the author expresses his sincere gratitude to his family and friends.

January 2012

Harutoshi Asakawa